NREL/TP-411-20276 • UC Category: 1262 • DE96000466

Wide-Band-Gap Solar Cells with High Stabilized Performance

Annual Subcontract Report 15 July 1994 – 14 July 1995

C. R. Wronski, R. W. Collins,
S. J. Fonash, J. S. Burnham, I-S. Chen,
L. Jiao, S. Kim, J. Koh, Y. Lee, H. Liu,
S. Semoushkina
Pennsylvania State University
University Park, Pennsylvania

NREL technical monitor: W. Luft

National Renewable Energy Laboratory
1617 Cole Boulevard
Golden, Colorado 80401-3393
A national laboratory of the U.S. Department of Energy
Managed by Midwest Research Institute
for the U.S. Department of Energy
under contract No. DE-AC36-83CH10093

Prepared under Subcontract No. XAN-4-13318-03

November 1995

This publication was reproduced from the best available camera-ready copy submitted by the subcontractor and received no editorial review at NREL.

NOTICE

This report was prepared as an account of work sponsored by an agency of the United States government. Neither the United States government nor any agency thereof, nor any of their employees, makes any warranty, express or implied, or assumes any legal liability or responsibility for the accuracy, completeness, or usefulness of any information, apparatus, product, or process disclosed, or represents that its use would not infringe privately owned rights. Reference herein to any specific commercial product, process, or service by trade name, trademark, manufacturer, or otherwise does not necessarily constitute or imply its endorsement, recommendation, or favoring by the United States government or any agency thereof. The views and opinions of authors expressed herein do not necessarily state or reflect those of the United States government or any agency thereof.

Available to DOE and DOE contractors from:
Office of Scientific and Technical Information (OSTI)
P.O. Box 62
Oak Ridge, TN 37831
Prices available by calling (615) 576-8401

Available to the public from:
National Technical Information Service (NTIS)
U.S. Department of Commerce
5285 Port Royal Road
Springfield, VA 22161
(703) 487-4650

Printed on paper containing at least 50% wastepaper, including 10% postconsumer waste

Table of Contents

Preface 1

Objectives 1

Scope of Work 1

Executive Summary 2

1. Improved Understanding of Stability in Materials and Solar Cells 8
   - 1.1 Stability in Materials 8
   - 1.2 Stability in Solar Cells 9
2. Intrinsic Materials Optimization 16
   - 2.1 Widegap Silicon Materials 16
   - 2.2 Widegap Silicon-Carbon Materials 18
   - 2.3 Widegap Silicon versus Widegap Silicon-Carbon 19
3. Solar Cells Optimized for Intrinsic Layer Performance 35
   - 3.1 Midgap Baseline Cell Deposition Monitored by RTSE 35
   - 3.2 Widegap Baseline Cell Deposition Monitored by RTSE 38
4. *P*-type Layer Optimization 48
   - 4.1 Hydrogen Treatments for Widegap *p*-type Layers 48
   - 4.2 TMB as *p*-type Layer Source Gas 49
5. Top Cell Interfaces 55
   - 5.1 Compositional Gradients 55
   - 5.2 TCO/*p-i* Interfaces 56
   - 5.3 *p/i* Interfaces 58
6. Solar Cell Grading 65
   - 6.1 Hydrogen Dilution Grading 65
   - 6.2 Widegap a-$Si_{1-x}C_x$:H Buffer Layers 65
7. Future Work 73
8. Bibliography 76

Preface

This report presents highlights of research performed from July 15, 1994 through July 15, 1995 under Phase I of a subcontract from National Renewable Energy Laboratory (a national laboratory of the U.S. Department of Energy operated by Midwest Research Institute) to The Pennsylvania State University (subcontract number XAN-4-13318-03 to prime contract DE-AC02-83CH10093). The research was carried out under the direction of C. R. Wronski, Leonhard Professor of Electronic Materials and Devices, serving as principal investigator; R. W. Collins, Professor of Physics and Materials Research, and S. J. Fonash, Distinguished Professor of Engineering Science, serving as co-principal investigators. Materials and solar cells preparation and real time spectroscopic ellipsometry studies were carried out in the Electronic Materials and Processing Research Laboratory and the Intercollege Materials Research Laboratory of The Pennsylvania State University. Contributions to this work were made by J. S. Burnham, I. -S. Chen, C. M. Fortmann, M. Gunes, T. Jamali-beh, L. Jiao, S. Kim, J. Koh, Y. Lee, H. Liu, Y. -W. Lu, and S. Semoushkina. The contract monitor in this project was Werner Luft. The authors are grateful to members of the Wide Band Gap Team, the Mid Band Gap Team, as well as A. Arya, M. Bennett, Y. -M. Li, N. Maley, and L. Yang of Solarex Thin Film Division, and S. Guha and J. Yang of USSC for helpful collaborations in this study.

Objectives

The objectives of this subcontract are to: 1) Develop a cost-effective amorphous silicon PV technology to foster a viable amorphous silicon PV industry in the United States ensuring that this industry remains a world leader in the a-Si technology; 2) Help the U.S. amorphous silicon PV industry to achieve the U.S./DOE PV Program FY 1995 milestone of 10% stable efficiency commercial thin-film modules; 3) Help the U.S. amorphous silicon PV industry to achieve 12% stable efficiency commercial thin-film modules by 1998; and 4) Achieve 15% stable efficiency multi-junction a-Si:H modules for large-scale utility use by the year 2005.

Scope of Work

The research in this program specifically applies to the activities of the NREL Wide Band Gap Team whose goal is to develop a single-junction, widegap solar cell with stabilized parameters: V_{oc} = 1.1V, J_{sc} = 8.2mA/cm^2, FF = 0.75, and efficiency = 6.8%. Phase I of this research and development program addresses the following issues:

1. Improved Understanding of Stability in Materials and Solar Cells
2. Intrinsic Materials Optimization
3. Solar Cells Optimized for Intrinsic Layer Performance
4. *P*-type Layer Optimization
5. Top Cell Interfaces
6. Solar Cell Grading

Executive Summary

Improved Understanding of Stability in Materials and Solar Cells

Real time *in situ* spectroscopic ellipsometry (RTSE) measurements and *ex situ* optical and electrical measurements were carried out to optimize a-$Si_{1-x}C_x$:H and a-Si:H materials for use as the *i*-layer (absorber) in widegap solar cells. Detailed characterization of both the annealed and stabilized degraded state a-$Si_{1-x}C_x$:H films, deposited with hydrogen dilution at substrate temperatures between 50°C and 300°C, were completed. Corresponding *in situ* and *ex situ* studies on a-Si:H, deposited at different temperatures, have also been undertaken. These studies are being carried out on materials prepared with and without hydrogen dilution. We have been able to compare diluted and undiluted material and cell properties for a-Si:H deposited at $T_S \geq 200$°C.

Progress has been made in the understanding of the relationships between bulk properties of intrinsic materials and *p-i-n* solar cell performance. Detailed studies are being carried out on *n-i*-metal Schottky barrier devices including *i*-layers which are thick enough so that the device characteristics are less sensitive to interface effects. Greater improvement in self-consistent modeling of different characteristics is being obtained with midgap distributions of charged and neutral defects consisting of three Gaussian distributions, rather than with the commonly used two Gaussian distributions, such as those in modeling of *p-i-n*'s using AMPS.

Solar cell devices have been modeled using densities of states (DOS) derived from analysis of thin film properties, and various characteristics of Schottky barrier and *p-i-n* structures were correlated with the bulk properties of the a-Si:H materials. The modeling and measurements of the solar cells under various illumination spectra are used to probe the spatial uniformity of the light-generated DOS. It is found that both red and white tungsten and Xenon light soaking as well as soaking with red light incident from either side of the cell cause only slight inhomogeneity with light induced defects generated in the *i*-layers.

The relationships between bulk parameters and *p-i-n* solar cell performance is also progressing. At this point the modeling of the dark J-V characteristics of the solar cells indicates that as in the Schottky barrier devices, *i*-layers must be thick in order to attain sufficient sensitivity to bulk parameter inputs. It is also likely that after the bulk parameters are unambiguously established, the modeling of thinner devices could be used to establish the interface parameters. At this stage typical device analysis is used, including the light and dark (as a function of temperature) J-V behavior and the quantum efficiency of cells.

Intrinsic Materials Optimization

Widegap materials using conventional PECVD were optimized as guided by the measured material parameters for thin films, including the Urbach tail slopes, the densities and nature of gap defects, and electron and hole mobility-lifetime products. The

degradation of thin films and the relative stabilities of different widegap a-$Si_{1-x}C_x$:H and high H-content materials were compared and related to their microstructure. Novel approaches to fabrication of intrinsic widegap materials were initiated based on the insights gained from the optimization studies of conventional materials on the subsurface equilibration of H and enhanced formation of the desired gas-phase precursors.

RTSE and *ex situ* photoelectric measurements were employed to optimize a-$Si_{1-x}C_x$:H alloy films for use as the absorber layers in widegap solar cells. The best material, which exhibits an optical gap of 1.95 ~ 2.00eV, is obtained at T_S = 200°C and an H-dilution ratio of R = 20. We have correlated the results of measurements on the thickness of surface roughness of a-$Si_{1-x}C_x$:H alloy films by RTSE and, independently, *ex situ* atomic force microscopy (AFM). The results clearly demonstrate that RTSE is providing the correct description of the surface thickness of the roughness and is in direct proportion to the rms roughness deduced by AFM. In addition it appears that RTSE is not affected by well-spaced asperities on the surface (spacing > 1000Å), which appear in some AFM images. On the other hand, RTSE can detect the presence of a 4 Å layer of low Si bond packing density on the surface that is not detected by AFM.

Studies on Si-rich a-$Si_{1-x}C_x$:H materials fabricated at Solarex and Penn State have been carried out. The annealed properties of the films produced with hydrogen dilution, over a wide range of T_S, are close to those of a-Si:H. However their stabilized degraded states are similar to those of the undiluted films, having significantly lower mobility-lifetime products and higher densities of neutral dangling bonds than a-Si:H materials. The large effect that hydrogen dilution has on the annealed state, which nearly vanishes in the stabilized degraded states of a-$Si_{1-x}C_x$:H, is not understood but is consistent with results on solar cells. The differences in the degradation between a-Si:H and a-$Si_{1-x}C_x$:H, if accurately modeled, may yield some new insights into the Staebler-Wronski Effect (SWE).

We have improved the growth process for widegap a-Si:H prepared with H-dilution of SiH_4. The boundary between amorphous film growth and mixed-phase amorphous/microcrystalline film growth as a function of H-dilution is quite gradual, depending strongly on the film thickness. For a substrate temperature of 250°C, we found that a dilution ratio R = $[H_2]/[SiH_4]$ of 5 is optimum for high density, microstructurally-stable amorphous films 0.5μm thick. For thinner films, a higher dilution ratio of ~10 can be used without loss of material quality due to void or crystallite development. For films prepared at 200°C the optimum single-phase amorphous films from a microstructural standpoint are obtained with R = $[H_2]/\{[SiH_4]+[CH_4]\}$ = 5 ~ 10. Films with R = 10 show the greatest surface smoothening upon coalescence, and the smoothest final film surface, whereas films with R = 5 achieve the highest bulk film density. For even larger R values (*e.g.*, R = 20, which is found to be optimum for a-$Si_{1-x}C_x$:H with a gap of 1.95eV), high quality very thin films (< ~ 200Å) can be obtained, but microcrystallinity develops in the thicker films (> ~ 500Å). Overall we conclude that the best a-Si:H is obtained just within the H-dilution boundary between the growth of amorphous and mixed-phase amorphous-

crystalline Si (as was concluded earlier for a-$Si_{1-x}C_x$:H). Currently our widegap pure a-Si:H solar cells prepared in our multi-chamber system are being deposited at 200°C with a reference value of R = 10.

Solar Cells Optimized for Intrinsic Layer Performance

We have developed the procedures for analysis of real time spectroscopic ellipsometry (RTSE) data on full SnO_2:F/*p-i-n* solar cells prepared in a single-chamber system. The procedures have been applied to an optimum midgap a-Si:H baseline cell prepared at 200°C in this system, which exhibited initial open-circuit voltage, fill-factor, short-circuit current density, and efficiency of: (0.83V, 0.71, 12.9mA/cm^2, and 7.6%) when prepared with a 4300Å *i*-layer without H-dilution on textured SnO_2:F. In the RTSE analysis, the thicknesses and optical gaps of the materials are obtained in the actual cell configuration, rather than being inferred from studies on thick layers. In general, our results reflect expectations based on thick layer studies, except for an unanticipated *p/i* interface contaminant layer that forms during single-chamber purging between *p*- and *i*-layer growth. For the midgap baseline cell whose performance parameters have been described here, an a-$Si_{1-x}C_x$:H *p*-layer doped with B using diborane is used. In this case the interface layer thickness is 1.7Å for an optimum interface formation process.

We have fabricated a series of solar cells using ~ 2000Å widegap a-$Si_{1-x}C_x$:H (~ 1.95eV) *i*-layers prepared at different H-dilution ratios under otherwise identical conditions. These cells were made with processing procedures similar to those for the midgap baseline cell, the only exception being the use of trimethylboron (TMB) as the *p*-layer doping source gas in an attempt to reduce p/i interface contamination (see "Top Cell Interfaces"). For cells deposited on specular ZnO, R = $[H_2]/\{[SiH_4]+[CH_4]\}$ = 20, yielded the best combination of initial V_{oc} (0.90V) and fill-factor (0.56). For cells deposited on specular SnO_2:F, R = 10 yielded the best combination (0.92V, 0.67). The latter cell yielded the best overall initial efficiency (3.9%) among samples prepared on three different TCO's with different R values from 2 to 20. The effective interface contaminant layer for the highest efficiency cell is ~ 0.6Å, an improvement attributed to an optimized interface formation process, including use of TMB as the *p*-type doping source gas as well as the beneficial effect of striking a H_2-rich plasma on the *p*-layer surface.

P-type Layer Optimization

As noted in the previous paragraphs, a TMB capability has now been established for the preparation of our widegap *p*-type layers in both multi- and single-chamber systems. For widegap *p*-layers formed both from diborane and TMB, any increase in gap with carbon incorporation is offset by a roughly equivalent increase in the conductivity activation energy. The only materials that we have observed deviating from such offsetting behavior are a-Si:H:B films whose gaps have been widened by post-hydrogenation with filament-generated atomic hydrogen. We have tried to incorporate such materials into *p-i-n* solar cells on SnO_2:F-coated glass substrates; however, the H-treatment is observed to

lead to a degradation of the TCO/*p* interface. Further work will focus on ZnO TCO substrates in an attempt to eliminate the problem.

The quality of the standard Penn State TMB a-$Si_{1-x}C_x$:H *p*-layers prepared in our multi-chamber system have been compared to those of Solarex using *p-i-n* structures, without graded layers, deposited on specular TCO substrates. The Penn State cell with a TMB a-$Si_{1-x}C_x$:H *p*-layer has V_{oc} = 0.92V, J_{sc} = 9.6mA/cm^2, and FF = 0.69 under AM1 light while the corresponding cell incorporating the Solarex TMB a-$Si_{1-x}C_x$:H *p*-layer has V_{oc} = 0.88V, J_{sc} = 9.6mA/cm^2, and FF = 0.58. The lower V_{oc} and FF can be due to the fact that Solarex *p*-layers were exposed to air much longer than Penn State *p*-layers and the H-treatments were not optimized.

We have also started to investigate *n-i-p* solar cell structures prepared on stainless steel and SnO_2 substrates in our multi-chamber system. Stainless steel/*n-i* structures have been fabricated with our a-$Si_{1-x}C_x$:H *p*-layers or μc-Si *p*-layers from USSC with both semitransparent Cr and specular TCO top contacts. A procedure has been established for obtaining the V_{oc} with the 10% transparent Cr contacts which corresponds to AM1.5 illumination of the transparent TCO structures. Comparisons have been made between cells with a-$Si_{1-x}C_x$:H *p*-layers and μc-Si *p*-layers and TCO as top contacts deposited at USSC on the same batch of stainless steel/*n-i* structures.

Even though the USSC structures were exposed to air for a long time before μc-Si *p*-layer deposition, higher V_{oc}'s were obtained with μc-*p*-layers prepared with BF_3. (It should be pointed out that *p-i* contacts in the case of the *n-i-p* cell structures have not been optimized.) Thus far the highest V_{oc}'s were obtained with hydrogen diluted a-Si:H layers deposited at 170°C. The cell structures, with no graded layers and USSC μc-Si *p*-layers had a V_{oc} of 0.96V, about 90meV higher than the corresponding *n-i-p*(SiC:H) structure. This value is very close to the highest V_{oc} obtained for an all a-$Si_{1-x}C_x$:H cell fabricated in a single-camber system at Penn State and monitored by RTSE. Fabrication of *n-i-p*(μc-Si) solar cells is now being undertaken at Penn State and the stability of the *p-i-n* and *n-i-p* structures with different *p*-layers is being investigated.

Top Cell Interfaces

Techniques are continuing to be developed for analysis of RTSE data collected during the preparation of the top junction (SnO_2/*p-i*) of the a-Si:H *p-i-n* solar cells in our single-chamber system. The monolayer-by-monolayer, optical fingerprint of standard cell preparation using a diborane-based *p*-layer on specular SnO_2 has been established. Such preparation yields an efficiency of 7.6% as determined from co-prepared cells on textured SnO_2 (which cannot be monitored directly by RTSE due to light scattering from the surface). The optical fingerprint deduced from RTSE includes the evolution of the bulk and roughness layer thicknesses, and the dielectric functions and optical gaps for the *p* and *i* layers, as well as the characteristics of the contaminant layer that forms between the two

layers during chamber flushing. Using the optical fingerprint to guide *p/i* interface formation procedure, optimization of the standard midgap cell has been carried out. The resulting further improvements yielding efficiencies as high as 8.4% are establishing a baseline for (i) incorporating widegap *i*-layers and (ii) for testing *p*-layer improvements.

The *p/i* interface structures of the solar cells fabricated with *p*-layers doped with either diborane or TMB, but otherwise prepared similarly, have been compared. Thinner interface layers have been achieved with an optimum *p*-layer doped with TMB (0.6Å) versus diborane (1.7Å) and the highest efficiency midgap and widegap a-$Si_{1-x}C_x$:H cells (~ 8.4% and 3.9%, respectively), were obtained when the thinnest interface layers were observed. Thus far no clear evidence has been found for V_{OC} being controlled by the interface layer thickness although this layer may affect the short-circuit current and/or fill-factor. However, such relationships cannot yet be determined unequivocally owing to the variation of other factors that may influence the cell parameters and efficiency.

RTSE has been used to obtain insights into the top-junction preparation in a single-chamber system and plasma shut-down and flushing procedures have been developed that reduce the thickness of the contamination layer at the *p/i* interface to < 1 monolayer when TMB is used as the doping gas. We have also applied filament H-treatments in our multi-chamber cell deposition process to diffuse H into the *p/i* interface region. With this process step, the efficiency of our mid-gap baseline cells has been increased from ~ 8% to 8.6%. It has been found in the RTSE studies of SnO_2:F and a-$Si_{1-x}C_x$:H *p*-layer exposure to *p*-type gases that there is no thermal decomposition in the case of TMB, indicating why TMB has led to further reduction of contamination at the *p/i* interface.

Solar Cell Grading

Procedures have been developed to fabricate and characterize layers prepared using continuously varying H-dilution. Such layers exhibit a continuously varying void volume fraction with thickness, and because of the non-linear dependence of growth rate on H-dilution, it is difficult to determine and control the thickness of the deposited layer. Using RTSE, we are able to determine the accumulated thickness versus time and the void volume fraction versus thickness, and thus establish the protocol for controlling these layers. Such an approach will be incorporated into either the *p*-layer or buffer layer process in widegap cells, designed so as to minimize TCO damage. Hydrogen-dilution grading has been employed in attempts to improve the open-circuit voltages of our optimum widegap solar cells prepared on specular SnO_2:F. The decrease in V_{OC} for cells on SnO_2:F, observed when R is increased from 5 to 20, is thought to result from reduction of the TCO upon penetration of H from the *i*-layer plasma through the *p*-layer. As a result, we have incorporated an H-dilution ramp from R = 2 to 20 in the first 200Å of the growth of the a-$Si_{1-x}C_x$:H *i*-layer where the properties of the resultant graded layer are deduced from RTSE measurements.

The capability of characterizing the optical gap profile versus thickness for widegap *p/i*-interface buffer layers using RTSE has also been developed. The incorporation of an optimized widegap buffer layer into our widegap a-$Si_{1-x}C_x$:H solar cells on specular SnO_2:F has led to an increase in V_{oc} from 0.93 to the highest value of 0.96V. However there was a corresponding drop in the fill factor from 0.62 to 0.60 which resulted in the same initial cell efficiency. We are currently characterizing the carbon concentration profiles and optical gap profiles of buffer layers which have resulted in the increase of initial efficiencies by 20% for cells prepared on ZnO TCO's.

1. Improved Understanding of Stability in Materials and Solar Cells

1.1 Improved Understanding of Stability in Materials

As in the case of intrinsic amorphous silicon films it was found that the charged defects in a-$Si_{1-x}C_x$:H films play a major role in determining their photoconductivity and sub-bandgap absorption. The a-$Si_{1-x}C_x$:H films deposited at T_S from 50°C to 300°C were characterized in both the annealed and the stabilized degraded states. Using the same defect distributions as in amorphous silicon, albeit, with increased overall defect densities, very good fits to the annealed state sub-bandgap $\alpha(h\nu)$ data could be obtained. The diluted a-$Si_{1-x}C_x$:H films have a lower charged and neutral defect density than the undiluted films but these densities are significantly greater than those in both H_2-diluted and undiluted a-Si:H. The values of α(1.3eV) in the annealed and the stabilized degraded states (steady state of 10AM1.5 illumination) are shown in Fig. 1.

The results for the a-$Si_{1-x}C_x$:H films deposited at $T_S \geq 200°C$ with and without hydrogen dilution reconfirmed the vast difference in these two types of materials. In the annealed state the electron mobility-lifetime products of the diluted films are very close to those of a-Si:H, which is about 20 to 50 times higher than those of the undiluted films. This is illustrated by the open symbols in Fig. 2 where the mobility-lifetime products versus generation rate are shown for diluted and undiluted a-$Si_{1-x}C_x$:H as well as for an a-Si:H film deposited at T_S = 250°C. It should be noted here that the sub-bandgap absorptions at 1.3eV in both of the a-$Si_{1-x}C_x$:H films are quite close together as seen in Fig. 4. In Fig. 3 the corresponding results are shown for the a-$Si_{1-x}C_x$:H films deposited with hydrogen dilution at different T_S. It is important to note that there is a spread in the results for the different T_S samples; however, the electron mobility-lifetime products of these diluted films, and the diluted films in Fig 2, exhibit similar characteristics in the annealed and the stabilized degraded states.

It appears more plausible at this point to associate such large differences in mobility-lifetime products of the diluted and undiluted a-$Si_{1-x}C_x$:H as due to the differences in lifetime rather than those in mobility. The similarities in the characteristics of the diluted, relatively low carbon content, a-$Si_{1-x}C_x$:H films to those of a-Si:H on the other hand suggest that there is also a strong resemblance in the gap states of these two types of materials. Consequently these can be self-consistently modeled with the defect distributions that have been used earlier for a-Si:H.

The characteristics of both diluted and undiluted a-$Si_{1-x}C_x$:H materials in the stabilized degraded state however are quite different from those of a-Si:H in the corresponding state. They now both exhibit similar electron mobility-lifetime products which are up to about 100 times lower than those of a-Si:H. This is illustrated in Fig. 2 by the filled symbols where the mobility-lifetime products are shown as a function of generation rate. In the stabilized degraded state the sub-bandgap absorptions of the a-$Si_{1-x}C_x$:H films are

nearly the same and about a factor of 5 higher than that of a-Si:H. This is illustrated in Fig. 4 where the sub-bandgap absorption measured with dual-beam photoconductivity (DBP) at low generation rate is shown as a function of photon energy for the diluted and undiluted $a\text{-}Si_{1-x}C_x$:H films and a-Si:H film of Fig. 2. The higher sub-bandgap absorptions of the $a\text{-}Si_{1-x}C_x$:H films reflect the higher densities of neutral dangling bonds - as verified by electron-spin resonance (ESR) measurements. However these higher densities are not sufficient to explain the 100 times different mobility-lifetime products. These results point to some fundamental differences in the nature of the degradation in both diluted and undiluted $a\text{-}Si_{1-x}C_x$:H and that of a-Si:H. Understanding of these differences in the degradation should offer new insight into the mechanisms responsible for SWE.

1.2 Improved Understanding of Stability in Solar Cells

The degradation of 0.6 to 0.8μm solar cells was investigated using illuminations with white light from a Xenon arc and an ELH halogen lamp, as well as the halogen lamp illumination with a red filter transmitting at wavelengths $\lambda > 640$nm. This allowed comparisons to be made between the two commonly used white light spectra (Xenon arc versus ELH halogen) and volume absorbed red light (ELH halogen + red filter). Because of the different intensities, I, involved, the comparison between the different illuminations was made using exposure times, t, where t was determined from the empirical relation, $I^{1.8}t$ = constant, reported by Yang *et al.*, *Appl. Phys. Lett.* **59**, 840 (1991). The relative intensities I were determined from the ratio of the photocurrents obtained with the different illuminations on cells under large reverse biases. Both homojunction and heterojunction solar cells were studied and the degradation characterized not solely by the light J-V's, as is generally done, but also by dark J-V and QE measurements. The latter two types of measurements are more sensitive to the actual gap state distributions and parameters than the light I-V's.

We found that the empirical relation found by Yang *et al.* for Xenon arc illuminations gave very good agreement for the white and red light from the ELH halogen illuminations when the intensities were normalized using the procedure developed here. Examples of this are illustrated with the QE and light J-V results in Fig. 5 and 6 for the case of a heterojunction cell and a homojunction cell. Also shown in the figures are the results for white light illumination from the Xenon arc lamp which is commonly used in the degradation studies of solar cells. These results clearly show that: 1) the large component of the blue light that is present in the Xenon arc white light spectrum is inefficient in degrading solar cells; 2) the large component of the red light in ELH halogen spectrum is the illumination which dominates the degradation in solar cells. This is clearly indicated by the same results obtained with and without the red light filter which implies that white ELH halogen illumination can be safely used to obtain essentially volume absorbed light effects.

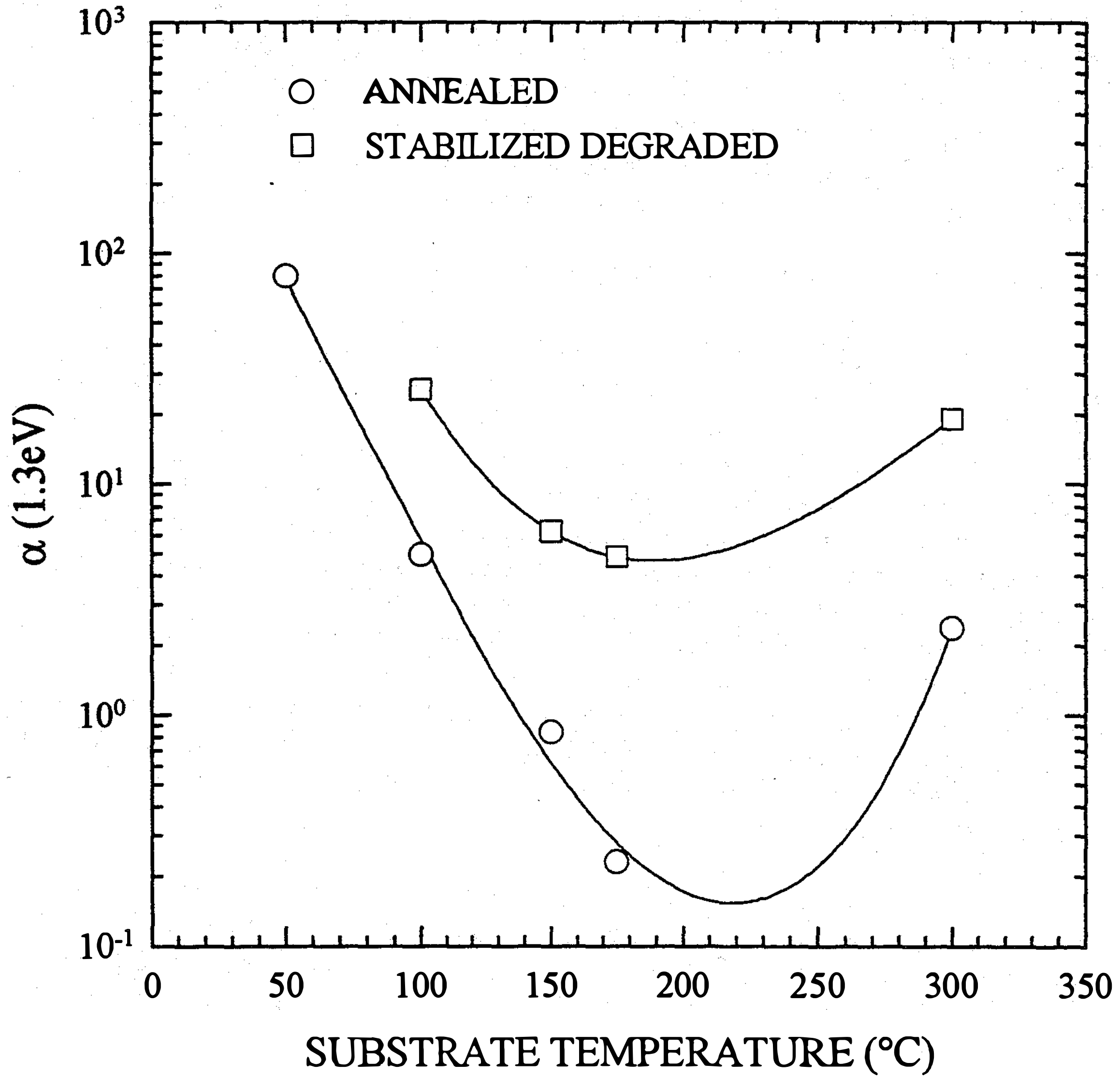

Fig. 1 α(1.3eV) for hydrogen diluted a-$Si_{1-x}C_x$:H deposited at substrate temperatures from 50°C to 300°C.

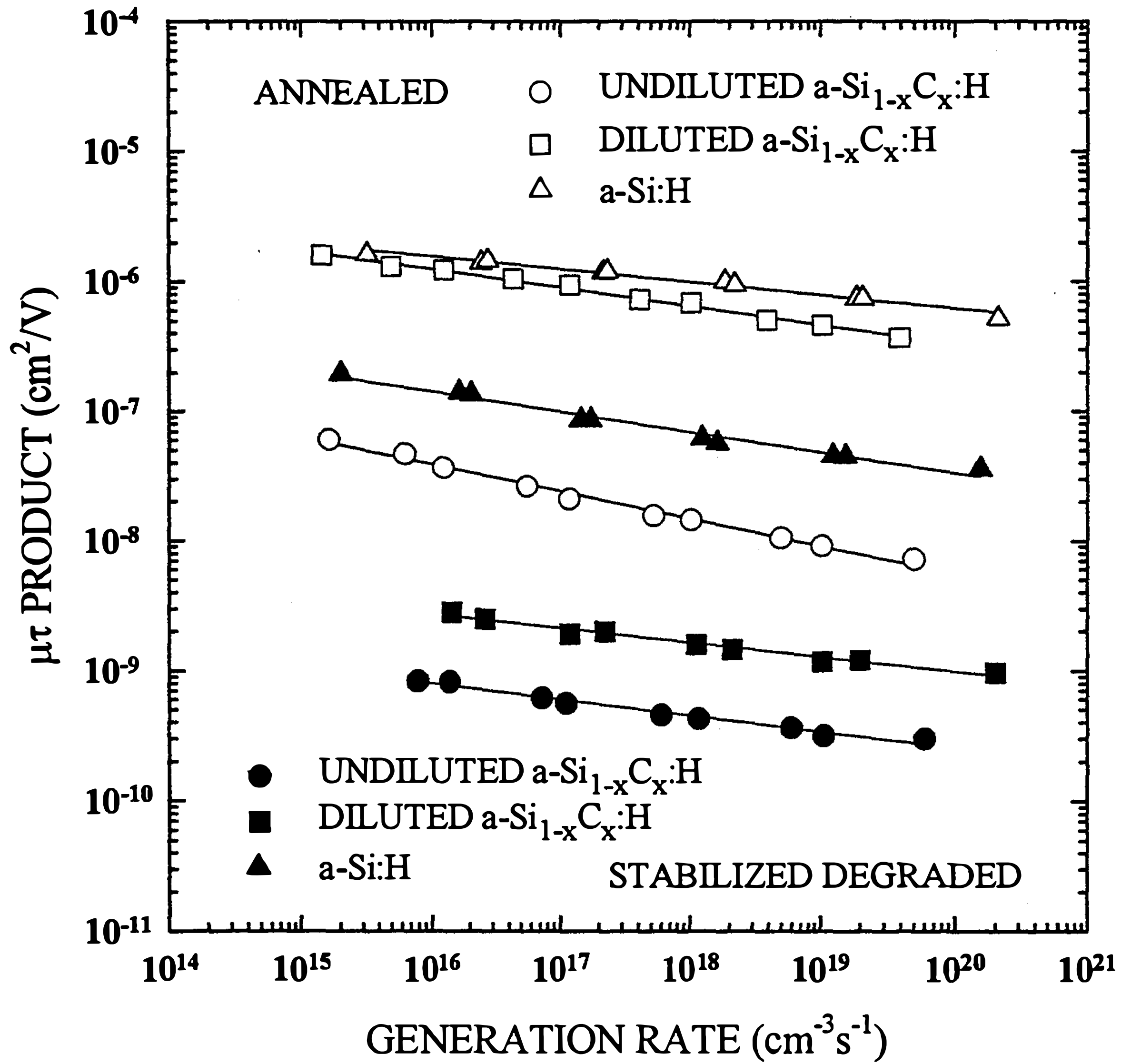

Fig. 2 Mobility-lifetime products versus generation rate for a-Si:H, undiluted and diluted a-Si$_{1-x}$C$_x$:H deposited at 250°C.

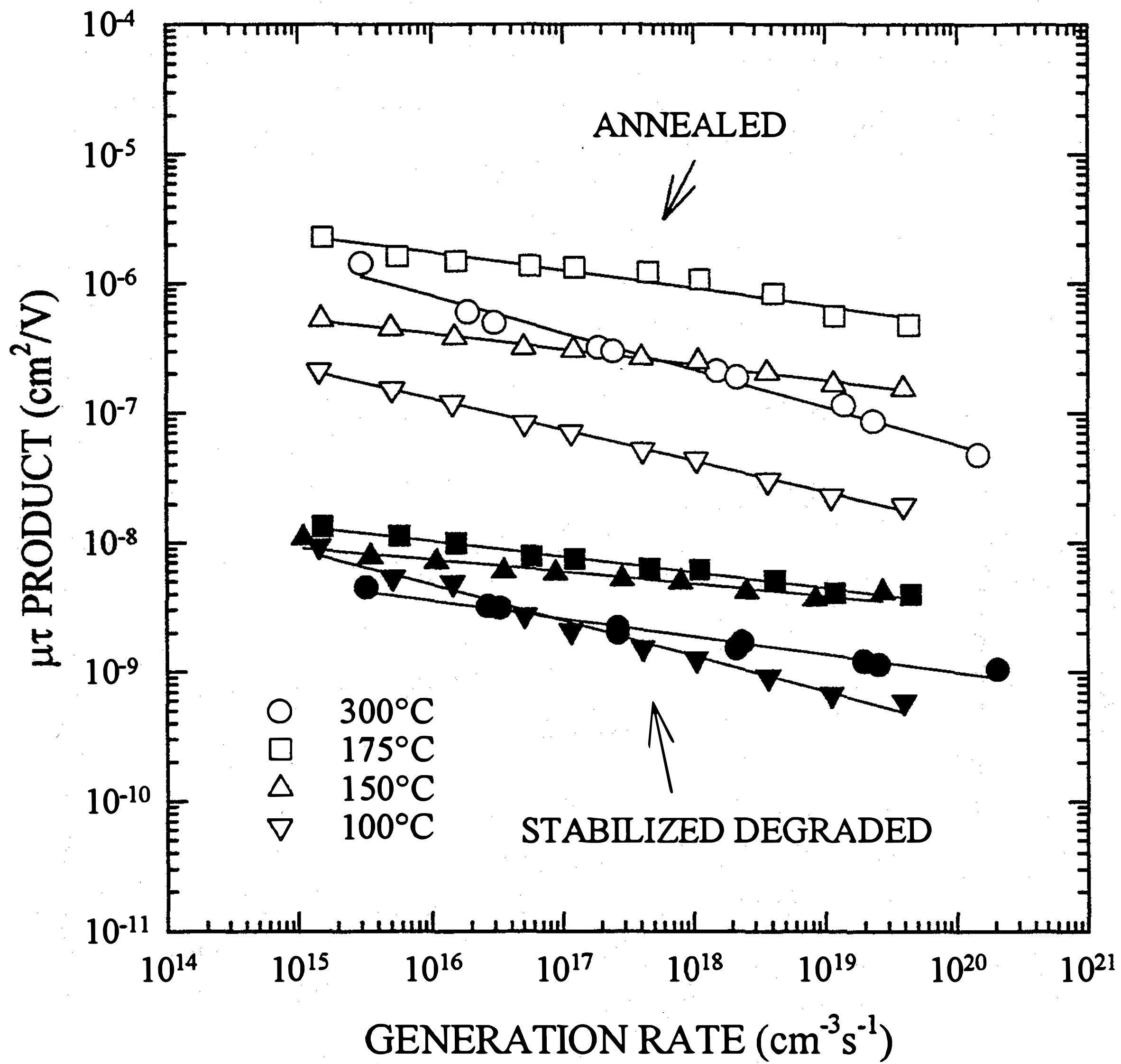

Fig. 3 Mobility-lifetime products versus generation rate for a-$Si_{1-x}C_x$:H films deposited at substrate temperatures from 100 ~ 300°C.

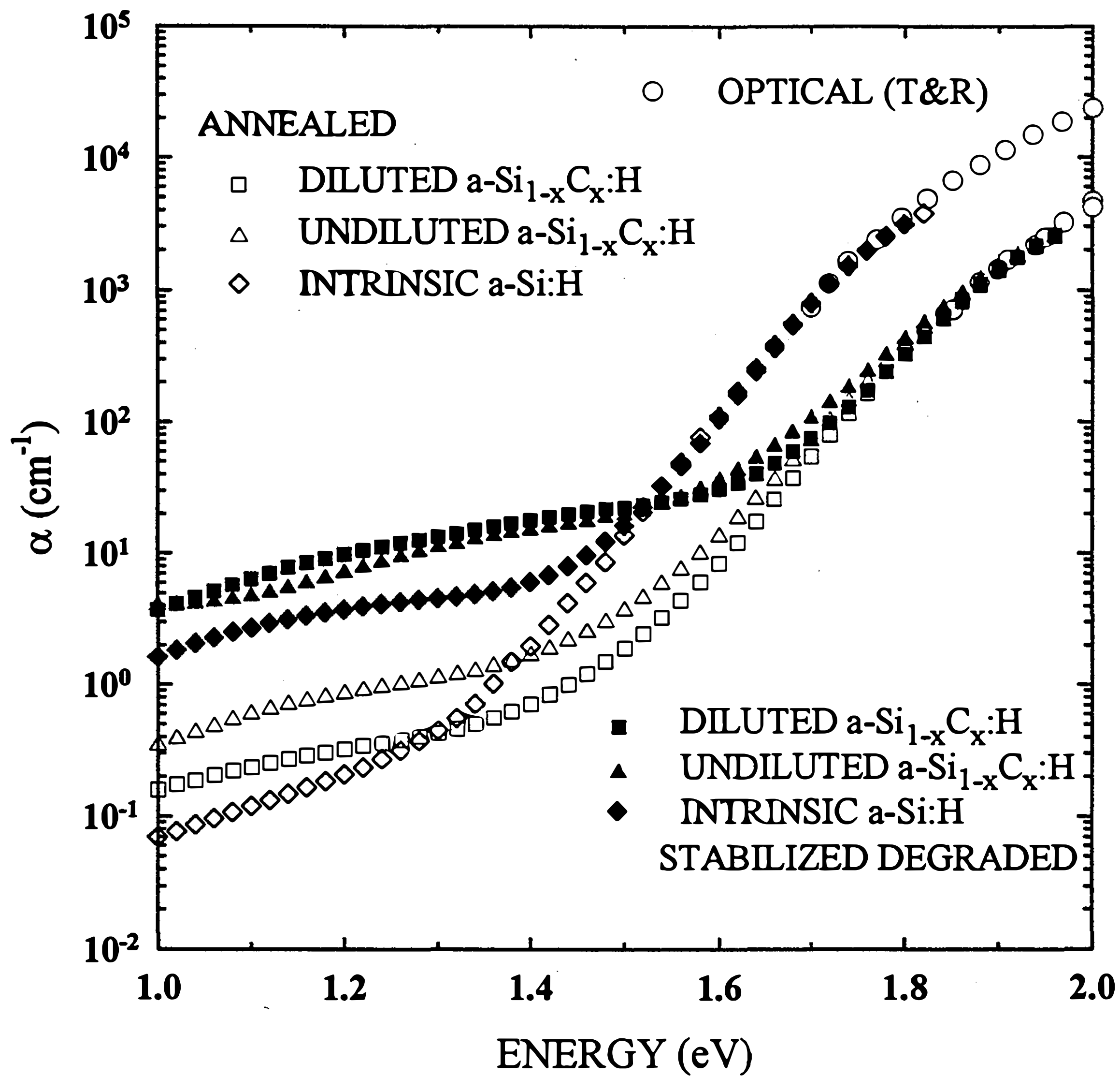

Fig. 4 Sub-bandgap absorption versus photon energy for a-Si:H, undiluted and diluted a-$Si_{1-x}C_x$:H.

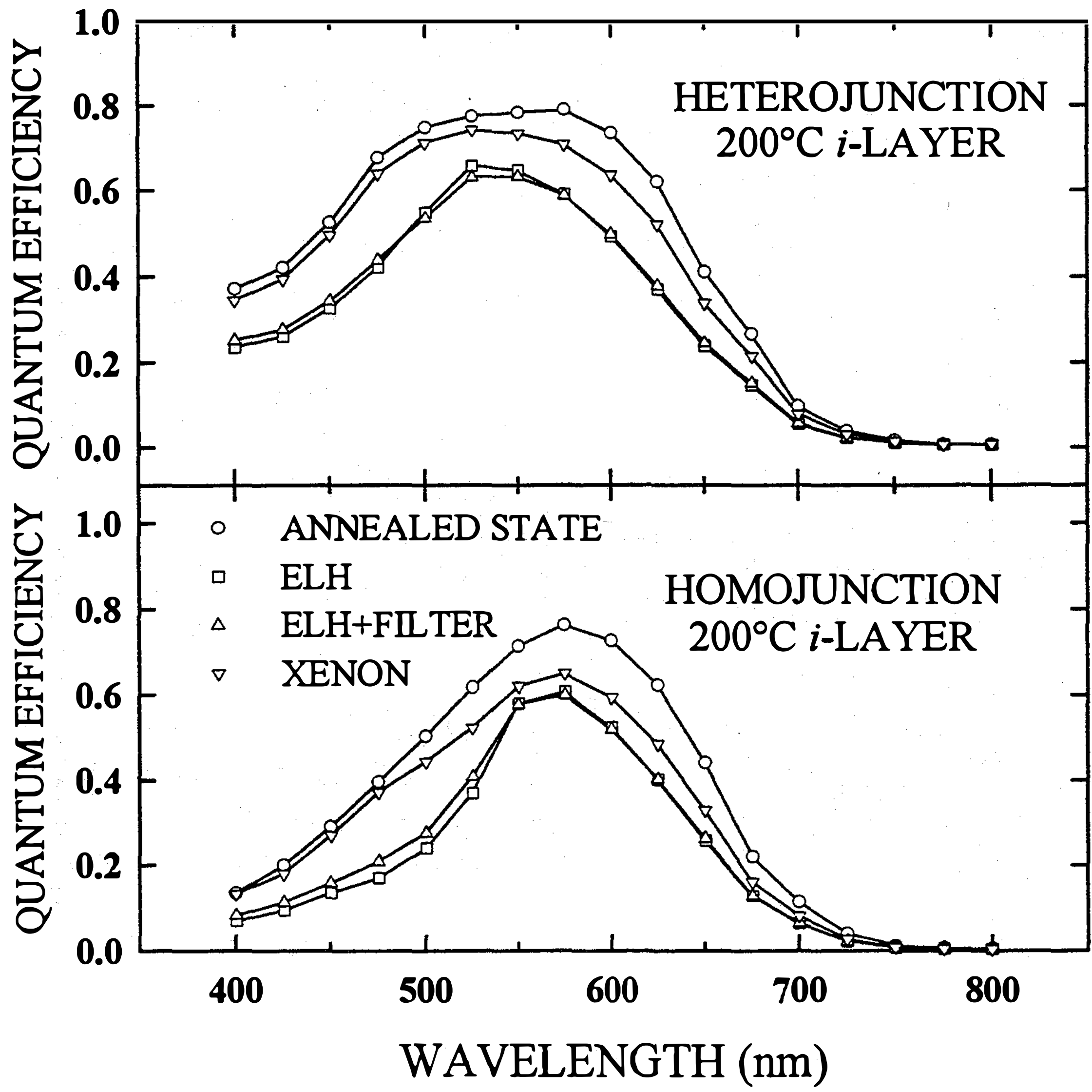

Fig. 5 Degradation of quantum efficiency of p-a-$Si_{1-x}C_x$:H heterojunction and p-a-Si:H p-i-n solar cells with Xenon arc, and ELH illuminations.

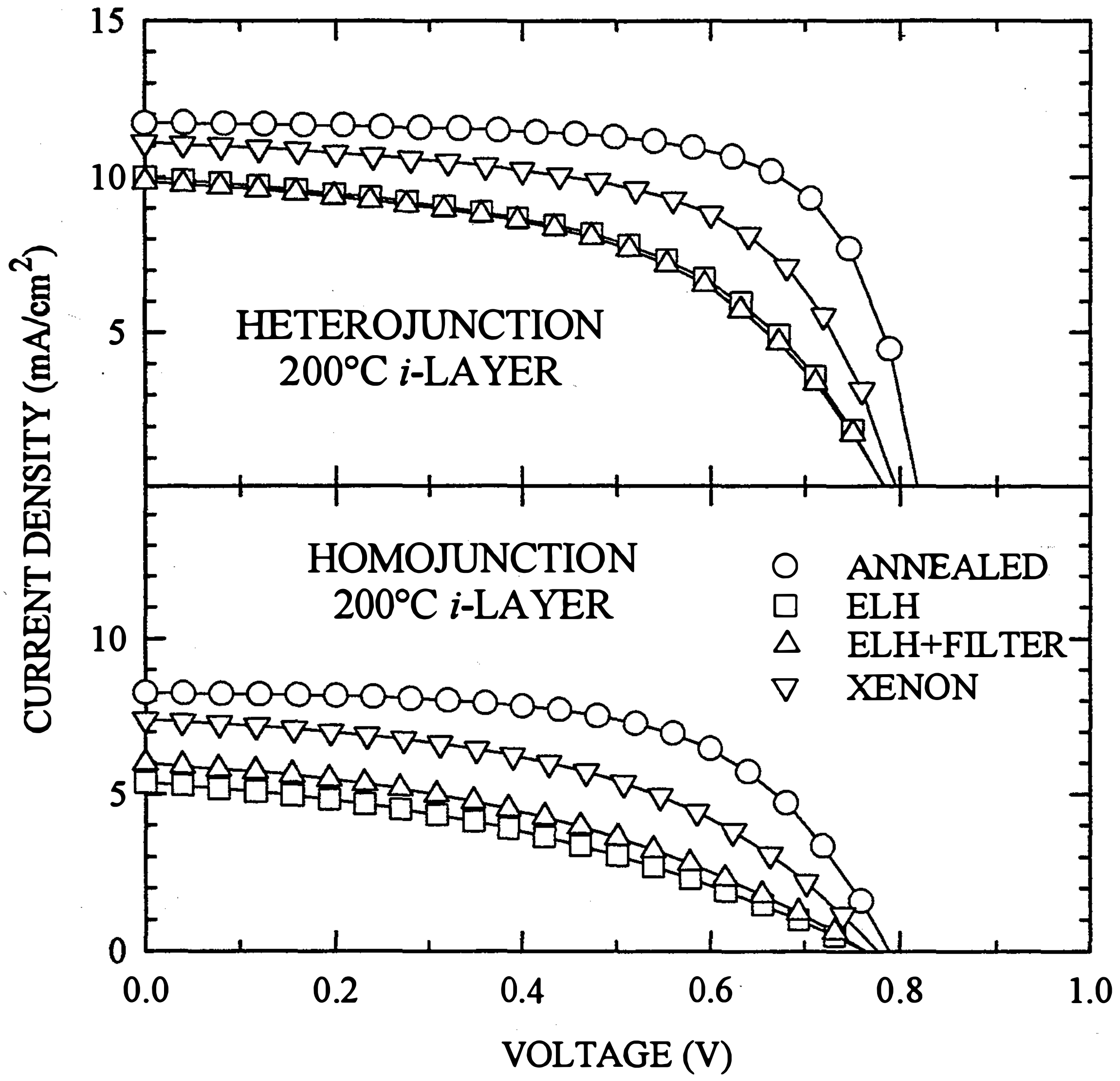

Fig. 6 Degradation of light I-V of *p*-a-$Si_{1-x}C_x$:H heterojunction and *p*-a-Si:H *p-i-n* solar cells with Xenon arc, and ELH illuminations.

2. Intrinsic Materials Optimization

2.1 Widegap Silicon Materials

We studied H-dilution of SiH_4 in a-Si:H preparation as a possible alternative route to more stable, wider-gap solar cells. Initial studies in which a-Si:H prepared with H-dilution of SiH_4 is characterized in terms of its optical gap, Urbach slope, defect density, and microstructure are needed for our concurrent modeling studies. We characterized a-Si:H films prepared as a function of substrate temperature (T_S) at H-dilution levels of R (= $[H_2]/[SiH_4]$) = 0 and 10. It was found that lower T_S yielded higher optical gaps because of the higher hydrogen content observed in earlier studies. There is a shrinking of the differences between the optical gaps of the undiluted and diluted films as T_s is lowered. The high activation energies, E_σ, of the dark conductivity 1.00 to 1.05eV for different T_S indicate that the Fermi levels are close to midgap in these materials. When assessed using sub-bandgap absorption and inverse Urbach slope, the best material (presumably having minimum disorder and lowest defect density) within the explored parameter range was obtained at T_S = 200°C and R = 10, as indicated in Fig. 7. The electron mobility lifetime products, $\mu\tau$, of the two types of films at different T_S are shown in Fig. 7(a), where it can be seen that the diluted films have higher $\mu\tau$ products than the corresponding undiluted films. Shown in Fig. 7(b) are the α(1.2eV) values for the diluted and undiluted films at different T_S, where all the diluted films show lower α(1.2eV) values than their corresponding undiluted films.

We have also studied the effect of H-dilution on the microstructural development of a-Si:H films prepared at 200°C. The goal of this work was to identify the optimum H-dilution ratio for use in solar cells prepared in our single-chamber system, based solely on RTSE. There is reason for optimism that this can be done considering our earlier studies of a-$Si_{1-x}C_x$:H in which it was demonstrated that the films exhibiting the greatest surface smoothening in the first 50Å of bulk film growth, not only exhibit the smoothest final film surface, but also the lowest density of midgap defects and least disorder. There is also a practical reason for applying RTSE alone, namely that thick films on smooth glass, Cr, or c-Si substrates have a tendency to peel immediately upon removal from the deposition system, making *ex situ* measurements of fundamental properties virtually impossible. Optimized solar cells can be fabricated, however, since the *i*-layer films prepared on textured SnO_2:F substrates do not peel due to the stress relief of the texturing. We are also interested in the fundamental insights that RTSE can provide concerning the differences between a-Si:H films prepared with pure SiH_4, and those prepared with H-dilution of SiH_4, owing to the observed higher stability of solar cells incorporating *i*-layers prepared under dilution conditions.

Fig. 8 shows the nuclei development and surface roughness layer evolution (d_s), along with bulk layer growth (d_b) for two films, both prepared on c-Si substrates at 200°C but

with two different values of $R = [H_2]/[SiH_4]$, namely R = 0 and 10. In preparing these films, the partial pressure of the source gases $[SiH_4]$ was maintained constant at 0.07Torr. Thus, the total pressure varies from 0.07 to 0.5Torr as R is increased from 0 to 20. For T = 200°C, the low pressure operation (0.07Torr) at low dilution tends to lead to improved properties due to the elimination of polysilane groups that form in the film at the higher pressures (0.5Torr). By maintaining a constant partial pressure, rather than a constant total pressure, one sees lesser improvement in the film properties with increasing H-dilution (since the starting film properties are already good), but an important improvement is observed nonetheless. The key parameter to be deduced from Fig. 8 is Δd_s, the decrease in roughness layer thickness that occurs during coalescence, *i.e.*, in the first 50 Å of bulk film growth. A significant increase in Δd_s occurs from 2.7 to 7.2Å as R is increased from 0 to 10. Based on previous observations, we conclude that films with R = 10 should exhibit superior electronic properties.

Fig. 9 shows Δd_s as a function of R for the full series of samples prepared at 200°C. (Also included in Fig. 2 are the corresponding results for a series of samples prepared at a substrate temperature of 250°C to be discussed later.) Overall, the coalescence improves with increasing R all the way up to R = 20. For $R \geq 40$, microcrystalline nuclei develop on the c-Si substrates right from the start. When this occurs, coalescence is incomplete and a more complicated optical model is required for interpretation of the RTSE data, namely one that includes the evolution of the crystalline structure. One also notes from Fig. 9 the well-known observation that the greatest improvement in film properties with H-dilution occurs at lower substrate temperature. One might conclude on the basis of Fig. 9 that one should use T_s = 200°C and R = 20 for optimum film properties. However, Fig. 10 shows the surface roughness evolution as a function of bulk film thickness in the first 1000 Å for the 200°C films of Fig. 9 prepared with R = 10 and 20. One observes that the film with R = 10 has a stable 9Å roughness layer throughout, whereas the roughness layer on the film with R = 20 increases in thickness rapidly to ~ 40Å as the bulk thickness increases above 200Å. This is found to be related to the development of crystallites which nucleate, not directly from the c-Si substrate in this case, but from the a-Si:H after ~ 200Å of film have been deposited. Clearly this film would not be suitable for a solar cell. In contrast, the structure of the film with R = 10 remains amorphous throughout the growth of a 5000Å thick film, and thus would be closer to optimal for use in a solar cell.

This points out a limitation in making conclusions solely on the basis of Δd_s in Fig. 9. Before choosing the optimum R value, one must also inspect the properties of the final film to ensure that it remained amorphous throughout the growth process. It likely that for a 100Å amorphous film, the optimum value of R is 20; however, these conditions lead to crystallinity for a 5000Å film and thus are not suitable for *i*-layer preparation. To complete this picture, Fig. 11 shows the relative void volume fraction, the surface roughness thickness, and the crystalline Si volume fraction after 200 Å of growth and in the final film for the series of films prepared at 200°C. From these results we conclude that R = 5 ~ 10 yields better microstructural properties for a-Si:H in comparison to R = 0. In fact R = 5 yields the highest thick film density but R = 10 yields the smoothest surfaces. From this

figure we conclude that R = 10 is quite close to the boundary of c-Si formation for thick films. As was observed earlier for a-$Si_{1-x}C_x$:H we conclude that the best a-Si:H is obtained just within the H-dilution boundary between the growth of amorphous and mixed-phase amorphous-crystalline Si.

2.2 Widegap Silicon-Carbon Materials

We have combined real time optical measurements, along with *ex situ* electronic characterization, in order to optimize a-$Si_{1-x}C_x$:H alloys (x = 0.09; E_g = 1.90 ~ 1.95eV) as a function of the H-dilution ratio R = $[H_2]/\{[CH_4]+[SiH_4]\}$ for widegap solar cell applications. In the earlier studies, we found that the H-dilution conditions for which maximum thin film nuclei coalescence occurs on the monolayer scale, as determined by RTSE, are precisely those conditions yielding the best photoresponse, lowest midgap state density, and steepest Urbach edge. This correlation provided further evidence that enhanced precursor diffusion and/or more effective cross-linking, observed at the atomic level, lead directly to a reduction in the disorder and defects that degrade the electronic properties of the resulting film. In the previous work, it was found that the optimum H-dilution ratio of R = 20 ~ 25 is the maximum that can be sustained without the formation of Si microcrystals during the preparation of a thick film.

In the previous optimization study, the only variable parameter was the H-dilution ratio R. Other parameters were fixed at typical values used for unalloyed a-Si:H; for example, a substrate temperature (T_s) of 250°C and an rf power of ~ 130mW/cm^2. We have fixed the optimum dilution ratio (R = 20) found for T_s = 250°C and have performed a series of a-$Si_{1-x}C_x$:H depositions as a function of substrate temperature. In this series, as in the earlier one with variable R, the $[CH_4]/[SiH_4]$ flow ratio was maintained at 2/3 to yield an alloy composition x in a-$Si_{1-x}C_x$:H of 0.09 at T_s=250°C. As an example of the information that RTSE provides, Fig. 12(a) shows the evolution of the two-layer structure of the a-$Si_{1-x}C_x$:H film prepared with R = 20 and T_s = 100°C. The surface layer of thickness d_s is characterized by its low density, and represents the nuclei in the early stages of growth and the roughness in the later stages of growth. The underlying bulk layer of thickness d_b is characterized by its bulk-like density, and represents the fully coalesced layer. The critical aspect to be observed in Fig. 12(a) is the smoothening effect in d_s that occurs between the time of nuclei contact (when d_b = 1 monolayer or ~ 2.5Å) and the time at which stabilization of the roughness occurs (when d_b ~ 50 Å). In Fig. 12(a), this smoothening amplitude is determined to be 8±0.5Å. It is interesting to compare the behavior in Fig 12(a) for a-$Si_{1-x}C_x$:H prepared with H-dilution with that for a-Si:H prepared at similar T_s, but from pure SiH_4 (*i.e.*, without H-dilution). Fig. 12(b) shows results for the latter deposition. In this case, a significantly lower smoothening amplitude of 3Å is obtained. Fig. 13 combines data for the smoothening amplitude Δd_s from a number of depositions versus T_s, including a-$Si_{1-x}C_x$:H prepared with R = 20 (plasma power flux ~ 130mW/cm^2) and pure a-Si:H prepared with R = 0 (plasma power flux ~

$50mW/cm^2$). Earlier we proposed that a larger amplitude for Δd_s indicates enhanced film precursor diffusion on substrate and film surfaces, as well as enhanced cross-linking between neighboring nuclei. The significant difference between the results in Fig. 2 for a-Si:H and a-$Si_{1-x}C_x$:H is not attributed to the presence of C, but rather to the H-dilution used for the alloys. From Fig. 13, we conclude that the H-dilution used for the alloys leads to a wider range of T_s over which strong coalescence is observed (150 ~ 250°C, compared to 225 ~ 275°C for a-Si:H with R = 0).

The implications of this result become clearer when the amplitude of the surface smoothening Δd_S is plotted together with other characteristics. In Fig. 14, we show Δd_S, along with the surface roughness thickness at a bulk layer thickness of 100Å, *i.e.*, $d_s(d_b = 100Å)$, the absorption coefficient at 1.2eV, and the inverse slope of the Urbach edge E_U, plotted for the alloys as a function of temperature T_s. It is apparent from this figure that the monolayer scale microstructural development (as indicated by Δd_S) correlates, not only with the surface smoothness of the coalesced film [as indicated by $d_s(d_b = 100Å)$], but also with E_U and $\alpha(1.2eV)$. For this series of samples as well, the monolayer-scale coalescence characteristics are an important indicator of good electronic quality. On the basis of the results in Fig. 14, we suggest that the best a-$Si_{1-x}C_x$:H films for solar cell applications with E_g = 2.0eV are obtained with R = 20 and T_s = 200°C. In general, however, the effect of substrate temperature on the properties of these alloys is quite weak compared to films prepared without H-dilution. Finally, we note that the electronic properties in the stabilized degraded state also follow the behavior of Fig. 14.

2.3 Widegap Silicon versus Widegap Silicon-Carbon

Fig. 15 compares the E_{2000} gaps for "wide gap" materials prepared using either carbon alloying, H-dilution, or alternating growth and *in situ* H-treatments. The former two series are plotted as a function of H-dilution. The deposition temperature was 240 ~ 250°C for these samples (solid points); however, the open points indicate the effect on the gap when the deposition temperature is reduced to 175 ~ 200°C. This figure shows that, for a-Si:H, a 0.06eV increase in gap occurs with increasing H-dilution to R = 10, and an additional 0.03eV increase occurs with the reduction in substrate temperature to 200°C. This yields a total gap increase of ~ 0.09eV over standard a-Si:H prepared without H-dilution (giving an E_{2000} gap value of 1.85eV). A much wider gap can be achieved through carbon incorporation. Incorporating carbon to yield x = 0.09 in a-$Si_{1-x}C_x$:H gives an E_{2000} gap of 1.88eV. Similar to the behavior for a-Si:H, a 0.05eV increase in gap occurs with H-dilution for a-$Si_{1-x}C_x$:H, and an additional 0.04eV increase occurs with the reduction in substrate temperature to 175°C. This yields a total gap increase ~ 0.21eV over standard a-Si:H (giving a gap value of 1.97eV). Typical results for a-Si:H prepared by alternating growth and atomic H-treatment at a deposition temperature of 220°C appear to be similar to those of a-Si:H with H-dilution of R ~ 5. Table 1 lists the basic properties of a-Si:H and a-$Si_{1-x}C_x$:H prepared as a function of H-dilution and substrate temperature. Results are also given for the Solarex a-$Si_{1-x}C_x$:H baseline series (presented along with our

a-$Si_{1-x}C_x$:H), and for typical a-Si:H prepared by alternating growth and H-treatments (presented along with our H_2-diluted a-Si:H).

In our earlier studies of a-$Si_{1-x}C_x$:H alloys, we found optimum values of T ~ 200°C and R = 20 ~ 25, as highlighted in Table 1. In these studies, it was concluded that there was a well-defined optimum value of R just within the amorphous side of the amorphous/(mixed-phase amorphous-microcrystalline) phase boundary (*i.e.*, the (a/μc)-boundary]. Because of the sensitivity of the quality of the a-$Si_{1-x}C_x$:H alloys to the value of R, it is important to perform even more detailed studies (*i.e.*, with a finer mesh in R) for a-Si:H. It is of interest to locate more accurately the (a/μc)-boundary as a function of thickness for pure a-Si:H and also to see if a-Si:H can be further optimized by operating on the amorphous side of this point. One might expect that the (a/μc)-boundary for a-Si:H is at a lower value of R than for a-$Si_{1-x}C_x$:H, owing to the role of carbon in suppressing crystallinity in the growth process.

Figs. 16 and 17 show the results of the effect of H-dilution on the microstructure of a-Si:H, fixing the substrate temperature at 250°C. Except where otherwise noted, the SiH_4 gas flow was 5sccm and the partial pressure of SiH_4 was fixed at ~ 0.075Torr. This leads to total pressures ranging from 0.16 to 0.52Torr for R ranging from 3 to 20. Fig. 16 provides a measure of the surface stability, defined as the rate of surface roughness increase with increasing bulk film thickness in the thick film regime (d = 3500Å). This figure shows that films prepared with $R < 10$ have a relatively stable microstructure, whereas for R = 10 and above there is a stronger increase in the surface roughness. The latter behavior is characteristic of the type of microstructural development that either presages or accompanies microcrystallinity. Further information on this aspect is shown in Figs. 17(a) and (b) where the volume fractions of voids and c-Si in the final film are given (open circles). There is no evidence of any c-Si in the films prepared with $R \leq 10$, and the void volume fraction in this range is low (< 3 vol.%.). However, we find that at high H-dilution, $R \geq 20$, the volume fractions of c-Si and voids are relatively large. Similar behavior was also observed in the a-$Si_{1-x}C_x$:H alloy films for $R \geq 30$, namely the appearance of silicon crystallites was accompanied by a relatively large volume fraction of voids.

The decrease in c-Si volume fraction with increasing $R \geq 20$ in Fig. 17(b) is an artifact associated with the thickness dependence of the microstructure. The final films prepared with larger R were thinner, and there is a general trend to increasing c-Si content with increasing thickness during deposition for films with $R \geq 20$. In general, we have found that the microstructure of the films with high H-dilution, $R \geq 10$, evolve with thickness (see Fig. 16). Specifically, the film with R = 10 is fully amorphous throughout the growth process, but exhibits a roughening trend with increasing thickness. The film with R = 20 nucleates as a-Si:H, but exhibits a roughening trend that accompanies the development of crystallites after the initial 50Å of growth (compare open and solid points in Fig. 17). After this initial development of crystallites, the volume fraction of the c-Si increases with increasing thickness. The films with R = 40 and 80 nucleate in a mixed

amorphous/crystalline phase with an increasing volume fraction of c-Si with increasing thickness. This behavior in which there is a gradual microstructural transition with increasing H-dilution from R = 10 (amorphous, but roughening) to R = 40 (mixed-phase amorphous/crystalline) contrasts with the relatively abrupt transition versus H-dilution for $25 < R < 30$ in the a-$Si_{1-x}C_x$:H alloys. The reason for this difference may have its origins in the differing microstructure of the two materials, taking into account the observation that Si crystallites can only readily nucleate from an amorphous network with a low packing density of tetrahedrally-bonded atoms. The a-$Si_{1-x}C_x$:H prepared with R = 20 may have a low bond-packing density relative to a-Si:H with R=5. For a-Si:H, a low bond-packing density develops gradually with thickness at high H-dilution (R = 20) and this is what initiates the formation of crystallites. In contrast, in a-$Si_{1-x}C_x$:H prepared at high H-dilution, the lower bond-packing density may exist from the onset of deposition. The conclusion based on the overall results in Figs. 16 and 17 is that from a microstructural standpoint, a dilution ratio of R = 5 appears optimum for thick films prepared at a substrate temperature of 250°C. At this dilution level, the highest density microstructure is obtained, and this microstructure is stable throughout the growth of thick films. Additional detailed studies similar to these have been performed at lower substrate temperatures in order to supplement the results obtained at 200°C and described earlier. However at this point a full analysis of the ellipsometric data has yet to be completed.

Table 1 A comparison of some of the properties of "widegap" a-Si:H and a-$Si_{1-x}C_x$:H versus H-dilution and substrate temperature. Also shown for comparison are results for films of the Solarex a-$Si_{1-x}C_x$:H baseline series (presented along with our a-$Si_{1-x}C_x$:H), and for typical a-Si:H prepared by alternating growth and filament-generated H-treatments (presented along with our H-diluted a-Si:H). The asterisks highlight optimized thick film materials.

a-Si:H

substrate temp (°C)	H-dilution ratio R	E_{2000} (eV) (α=2000cm^{-1})	E_U (meV)	α (cm^{-1}) (at 1.2eV)	$\mu\tau$ ($10^{-6}cm^2/V$) (G=$10^{19}cm^{-3}s^{-1}$)
170	0	1.83	51.2	0.393	1.69
200	0	1.80	50.8	0.282	1.26
240	0	1.76	50.6	0.457	1.62
280	0	1.74	50.7	0.862	3.42
170	10	1.86	-	-	-
*200	10	1.85	48.3	0.20	3.04
240	10	1.82	49.8	0.266	4.86
280	10	1.82	50.6	0.66	16.9
*220	growth/H-treat 10/20 min	1.82	47.0	0.18	18.0

a-$Si_{1-x}C_x$:H, effect of substrate temperature (R = 20) and H-dilution (T_s = 250°C)

substrate temperature (°C)	E_{2000} (eV) (α=2000cm^{-1})	E_U (meV)	α (cm^{-1}) (at 1.2eV)	$\mu\tau$ (cm^2/V) (G=$10^{19}cm^{-3}s^{-1}$)
50	2.00	91	58.0	-
100	2.00	57	3.05	2.41×10^{-8}
150	1.98	55	0.59	1.75×10^{-7}
*175	1.97	52	0.12	6.49×10^{-7}
250	1.93	56	0.24	4.57×10^{-7}
300	1.88	60	1.65	1.01×10^{-7}
Solarex A3006-1	1.91	50	0.10	1.79×10^{-7}
Solarex A3019-2	1.98	63	0.62	3.50×10^{-8}

H-dilution R	E_{2000} (eV) (α=2000cm^{-1})	E_U (meV)	α (cm^{-1}) (at 1.2eV)	$\mu\tau$ (cm^2/V) (G=$10^{19}cm^{-3}s^{-1}$)
0	1.88	62	1.41	6.6×10^{-8}
2	1.89	61	0.96	7.2×10^{-8}
10	1.91	61	0.80	-
20	1.93	54	0.34	2.5×10^{-7}
40	1.91	116	10.7	-

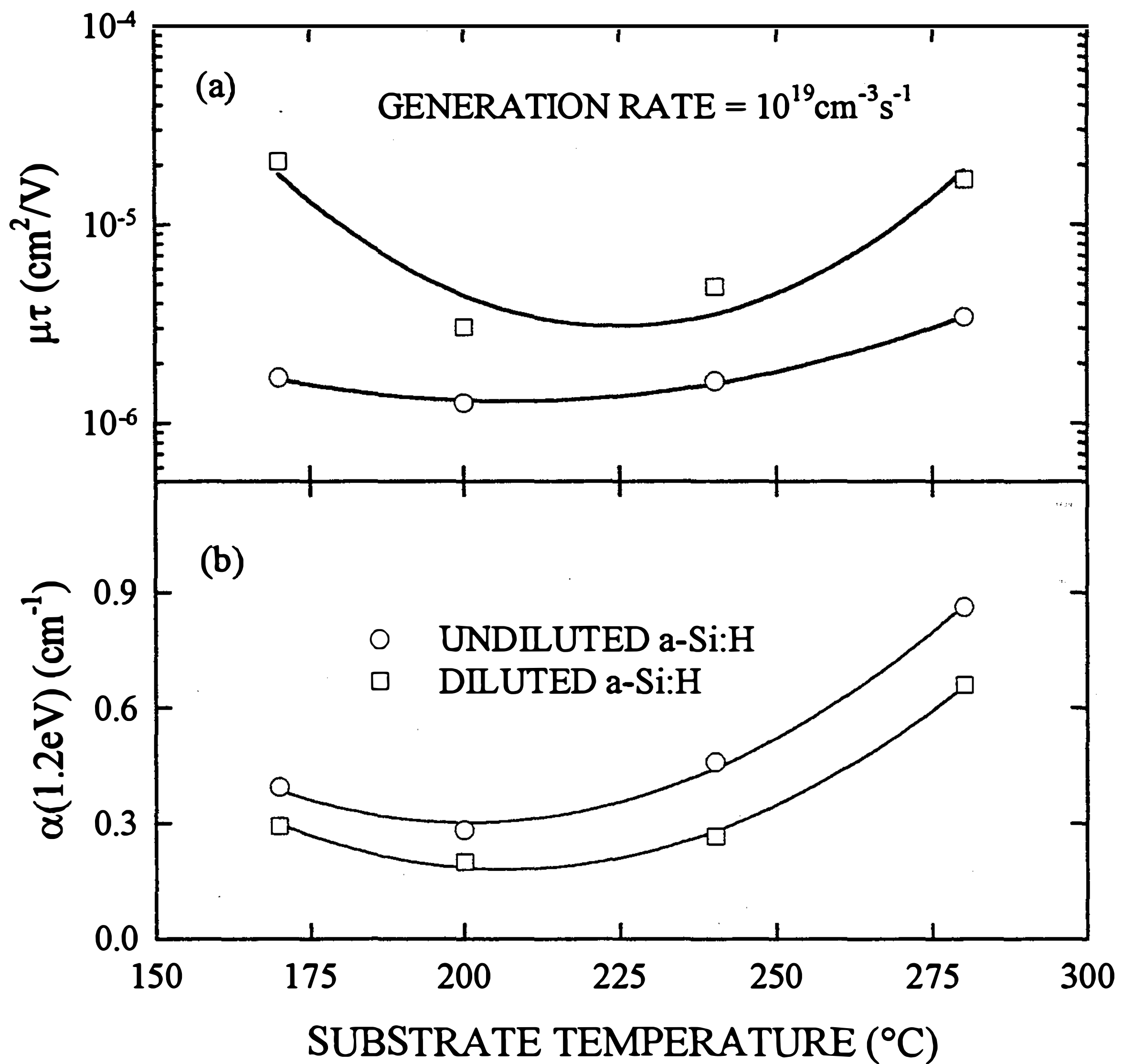

Fig. 7 The dependence of the electron mobility-lifetime product and the absorption coefficient at 1.2eV on substrate temperature for hydrogen diluted and undiluted a-Si:H films.

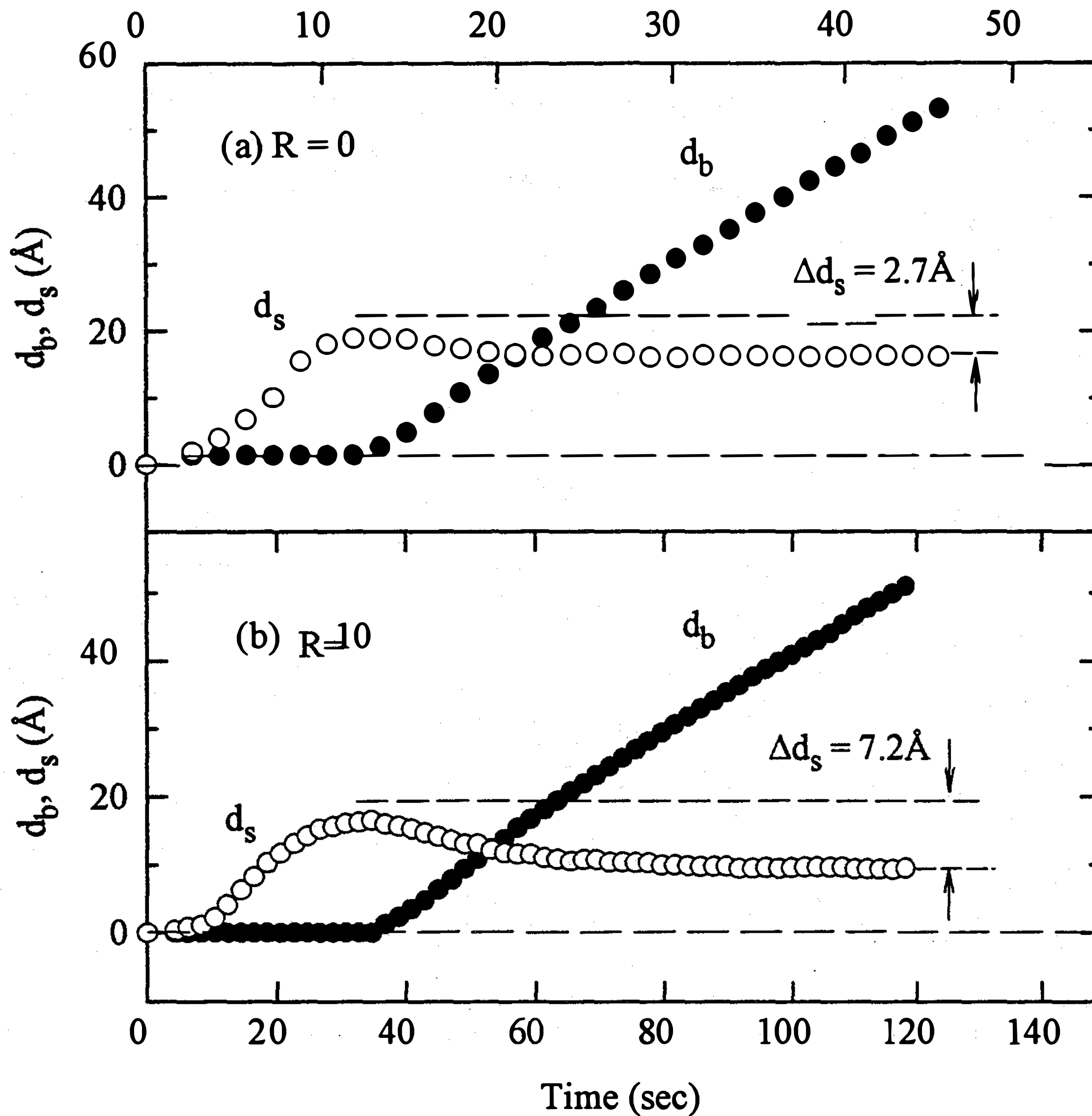

Fig. 8 Time evolution of the low density surface layer (d_s) and bulk layer (d_b) thicknesses deduced from RTSE data collected during the deposition of two a-Si:H films prepared on c-Si with H_2-dilution ratios (a) R = $[H_2]/[SiH_4]$ = 0 and (b) R = 10, both at 200°C. The results for the deposition with R = 10 exhibit a greater degree of coalescence of initial nuclei. Both depositions were performed with a fixed rf power flux of ~ 70mW/cm^2.

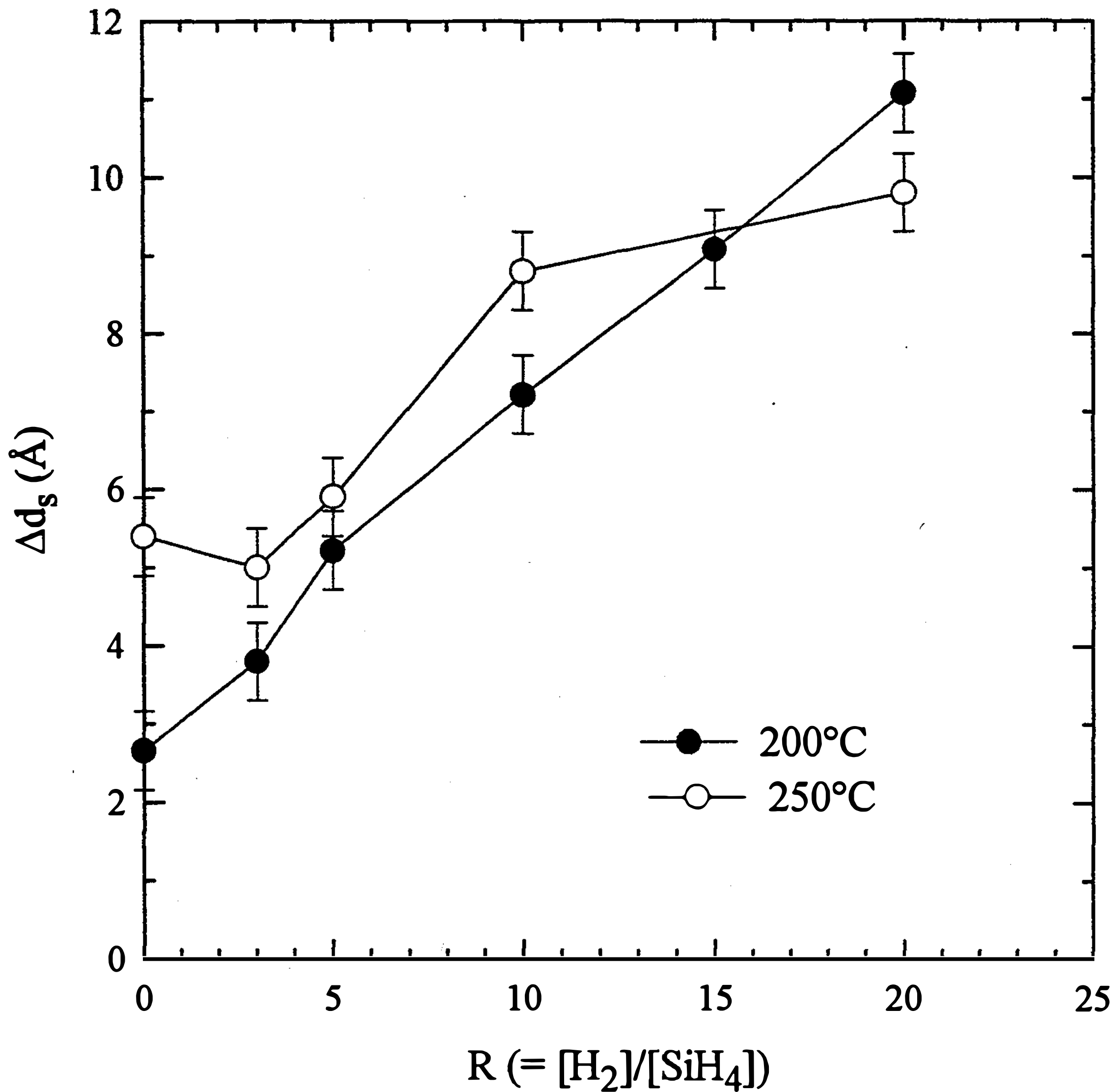

Fig. 9 A measure of the degree of coalescence of a-Si:H thin film nuclei plotted as a function of the H-dilution level used in the film growth process. Δd_s is the amount of surface smoothening that the film undergoes between the time of nuclei contact, when the roughness is generally largest, and the time when the bulk film is 50Å thick, when the film has coalesced and the roughness has stabilized. Results are given for a series of a-Si:H samples prepared at 200°C (solid points) and a series prepared at 250°C. The plasma power flux was ~ 70mW/cm^2 for both series.

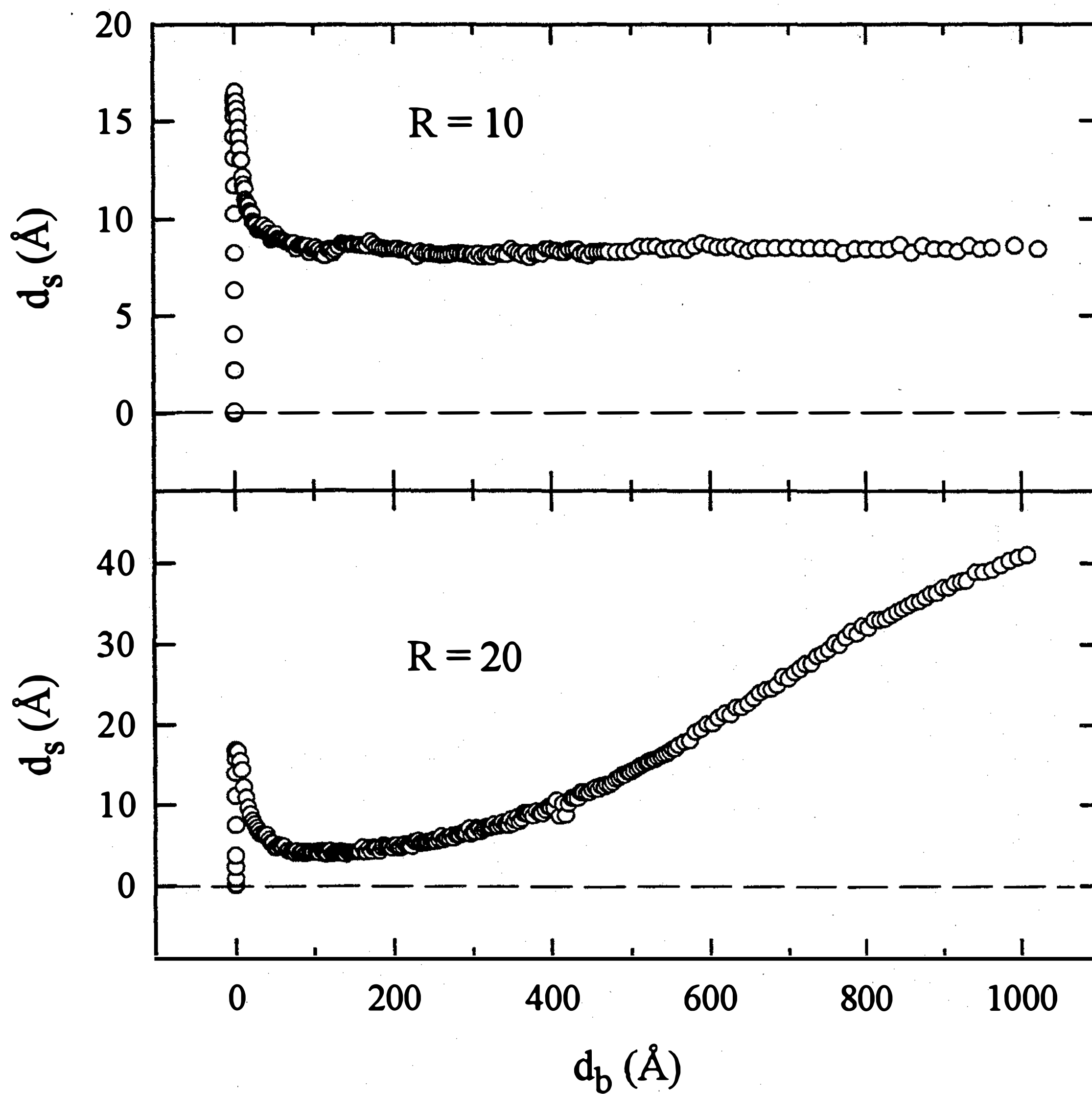

Fig. 10 Evolution of the surface roughness layer thickness as a function of the bulk layer thickness for two a-Si:H films prepared at a T_s value of 200°C with R = 10 (top) and 20 (bottom). The extreme roughening for R = 20 has been attributed to the nucleation of crystallites which occurs after a bulk layer thickness of ~ 200Å.

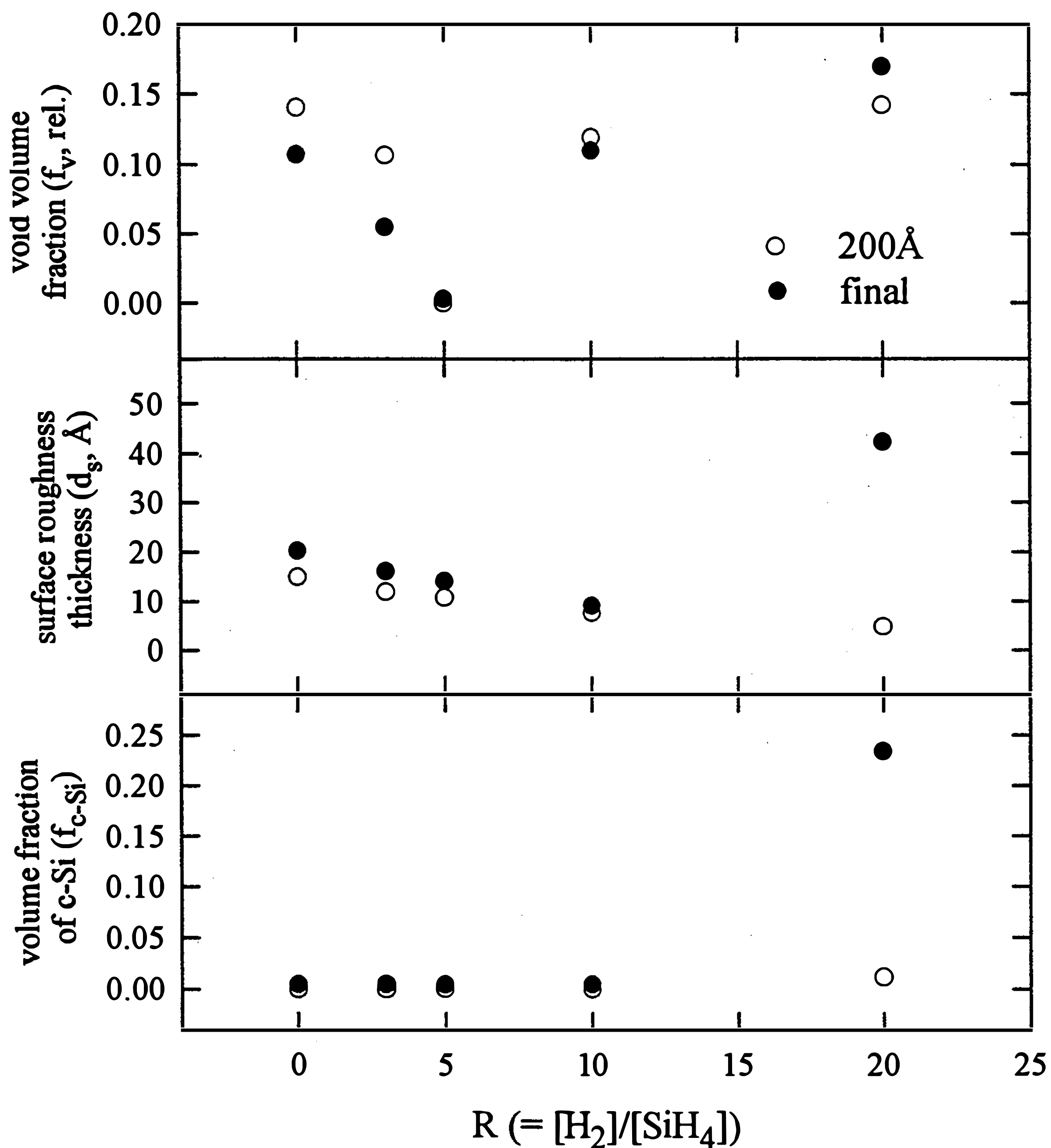

Fig.11 The relative void volume fraction, the surface roughness thickness, and the crystalline Si volume fraction plotted as a function of the H-dilution ratio R for a series of a-Si:H films prepared on c-Si at 200°C. The rf power flux for these depositions results was ~ 70mW/cm^2. These results were deduced from analyses of the RTSE spectra collected at a thickness of 200Å (open points) and upon plasma termination at the end of deposition (solid points).

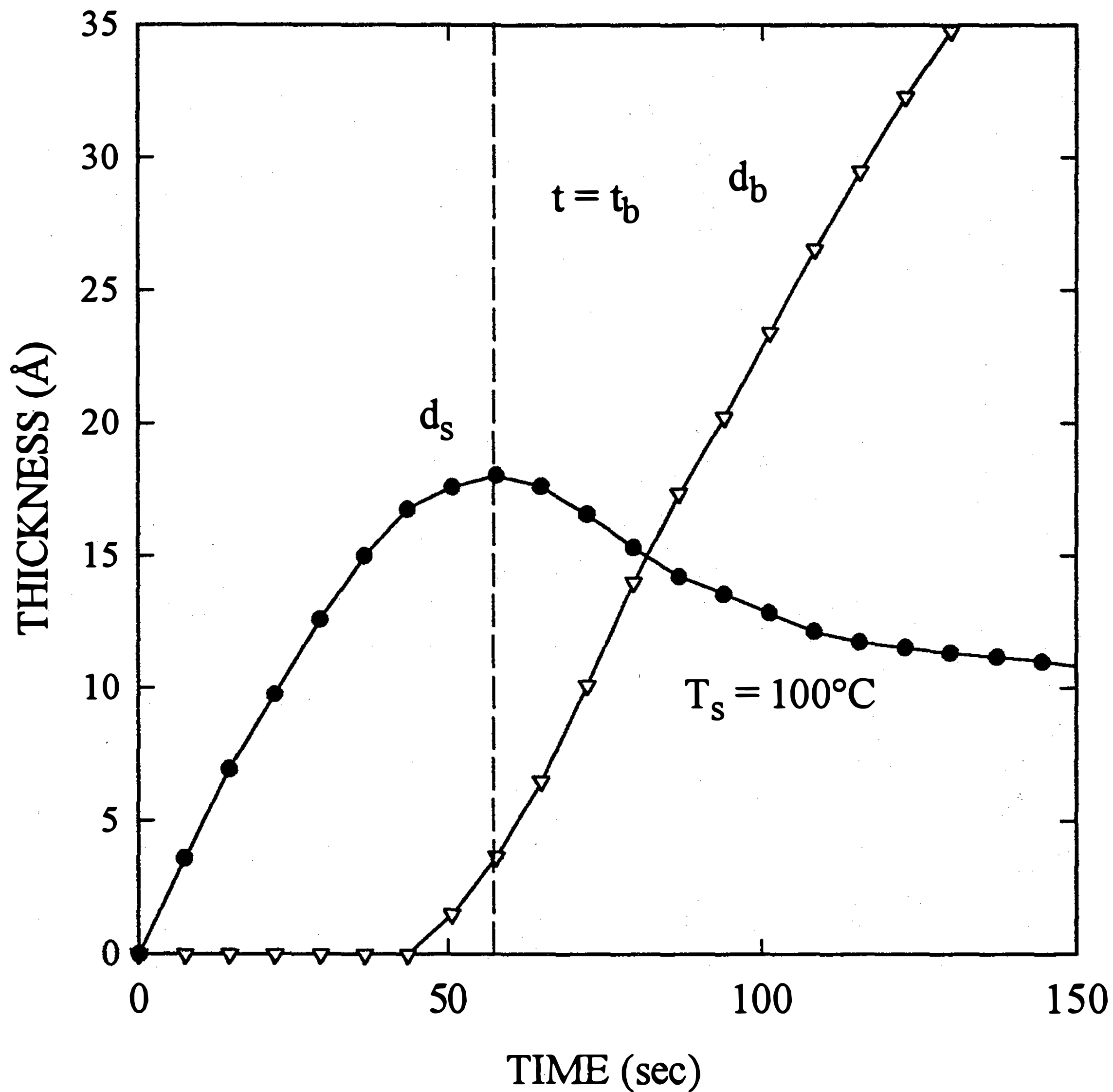

Fig. 12(a) Evolution of d_b, which denotes the bulk layer thickness, and d_s, which denotes either the low density nucleating layer thickness when $t < t_b$ or the overlying surface roughness layer thickness when $t > t_b$. t_b is the time at which the first bulk-like monolayer is formed ($d_b \sim 2.5$Å). These results were deduced from RTSE data collected during the growth of a-$Si_{1-x}C_x$:H with R = 20 and T_s = 100°C. The rf power flux was ~ 130mW/cm^2.

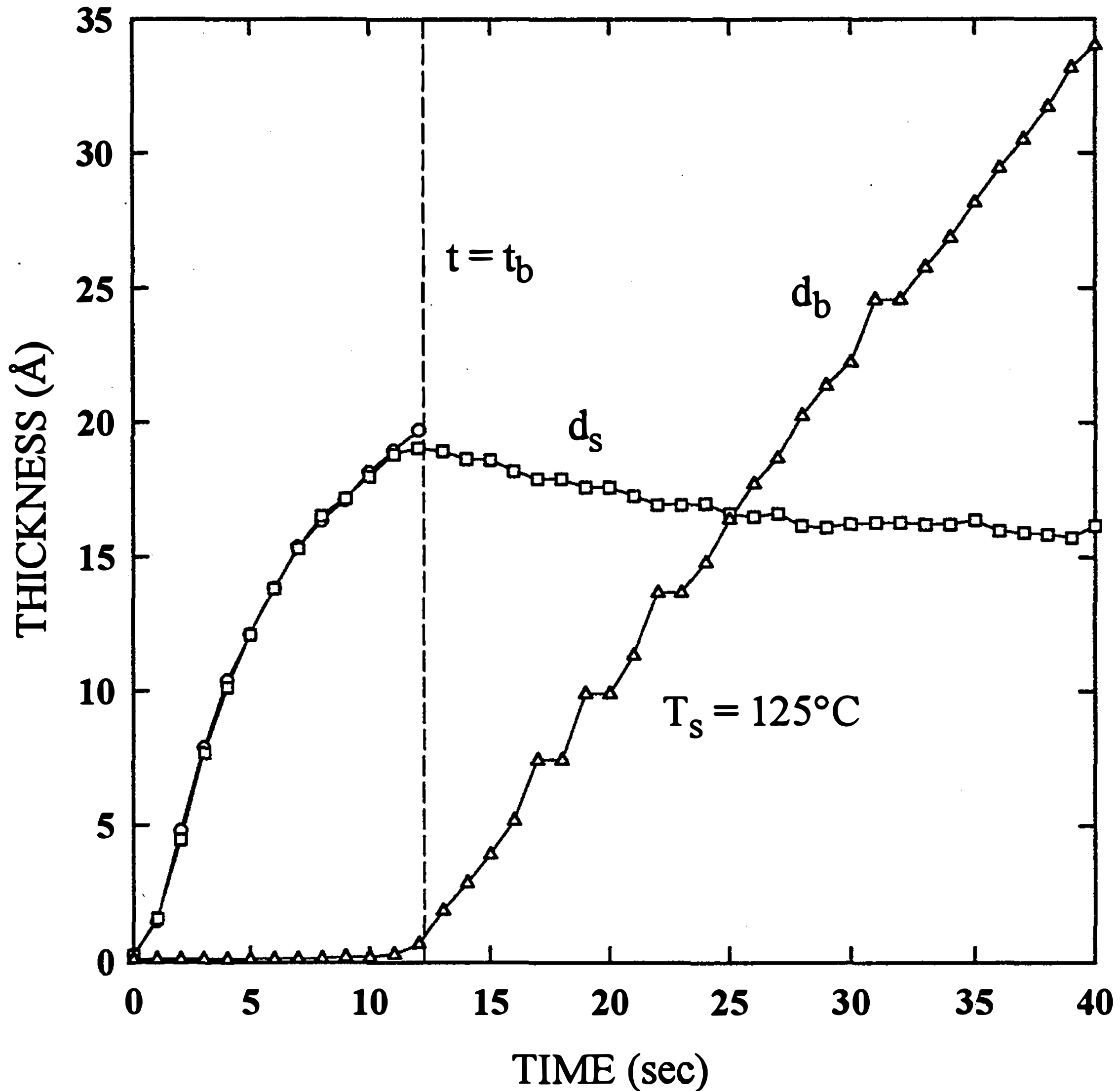

Fig. 12(b) Evolution of d_b, which denotes the bulk layer thickness, and d_s, which denotes either the low density nucleating layer thickness when $t < t_b$ or the overlying surface roughness when $t > t_b$. These results were deduced from RTSE data collected during the growth of a-Si:H with R = 0 and T_s = 125°C. The rf power flux was ~ 70mW/cm^2.

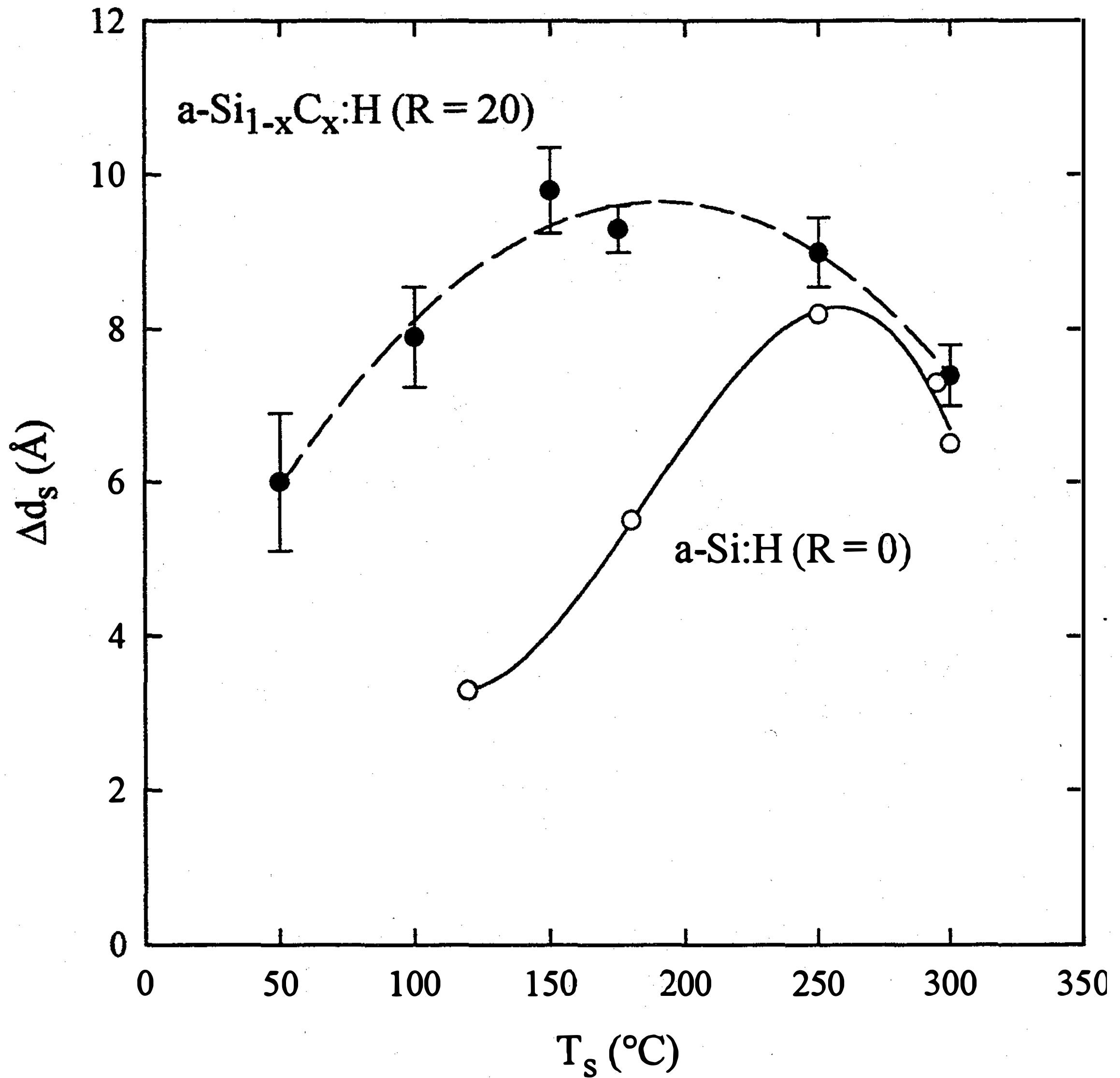

Fig. 13 Amplitude of surface smoothening in the first 50Å of bulk layer growth, plotted as a function of substrate temperature for two series of films. The solid points represent a-$Si_{1-x}C_x$:H alloy films with an optimum H-dilution of R = 20, and an rf power of ~ 130mW/cm^2 and the open points represent a-Si:H films prepared without H-dilution (R = 0) and an rf power flux of ~ 70mW/cm^2.

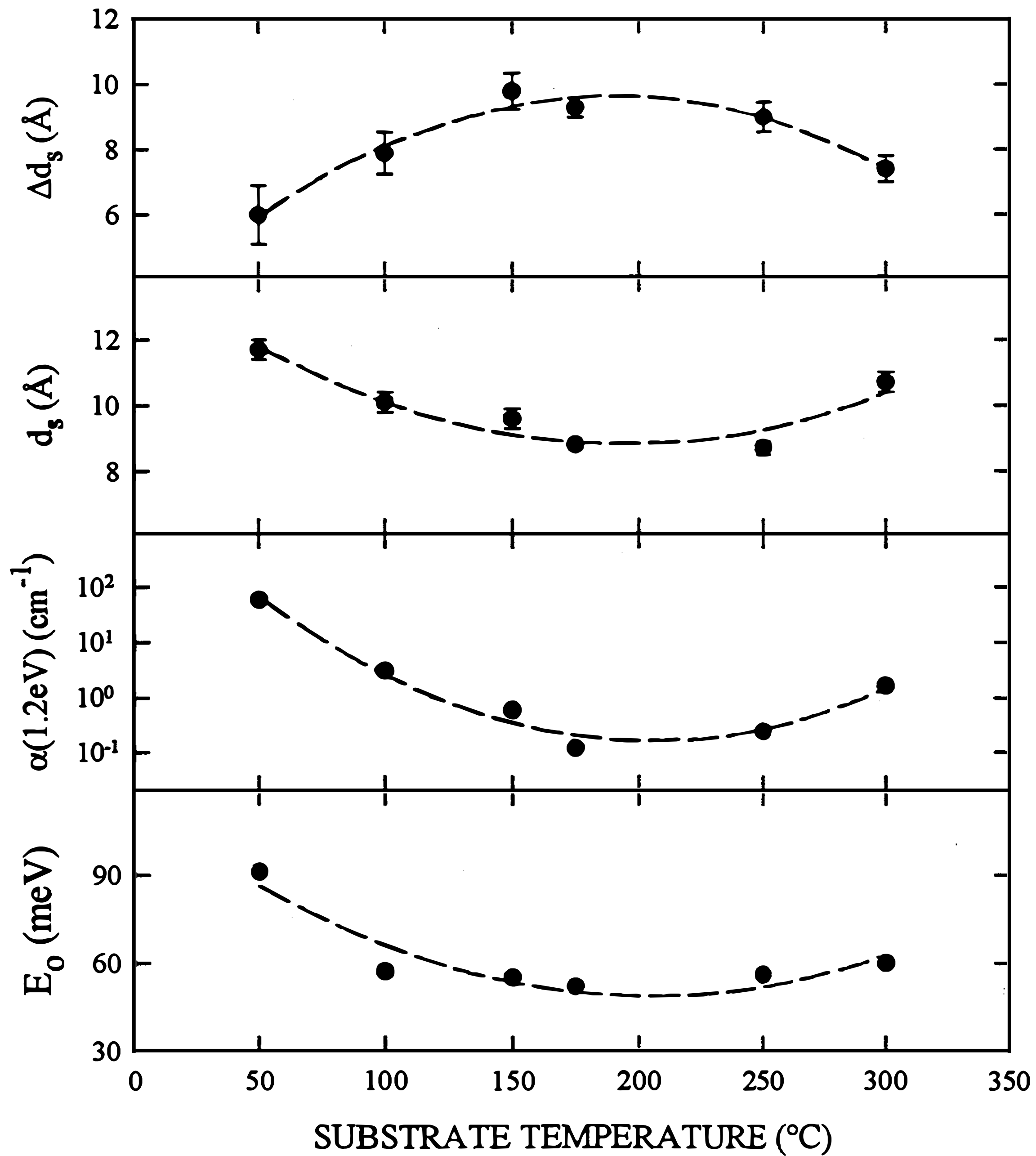

Fig. 14 Microstructural and electronic parameters measured in real time and *ex situ*, respectively, for a-$Si_{1-x}C_x$:H films versus substrate temperature. An optimum H-dilution level of R = 20 was employed. From top to bottom: amplitude of surface smoothening during coalescence, surface roughness after 100Å of bulk film growth, absorption coefficient at 1.2eV, and inverse slope of the Urbach tail.

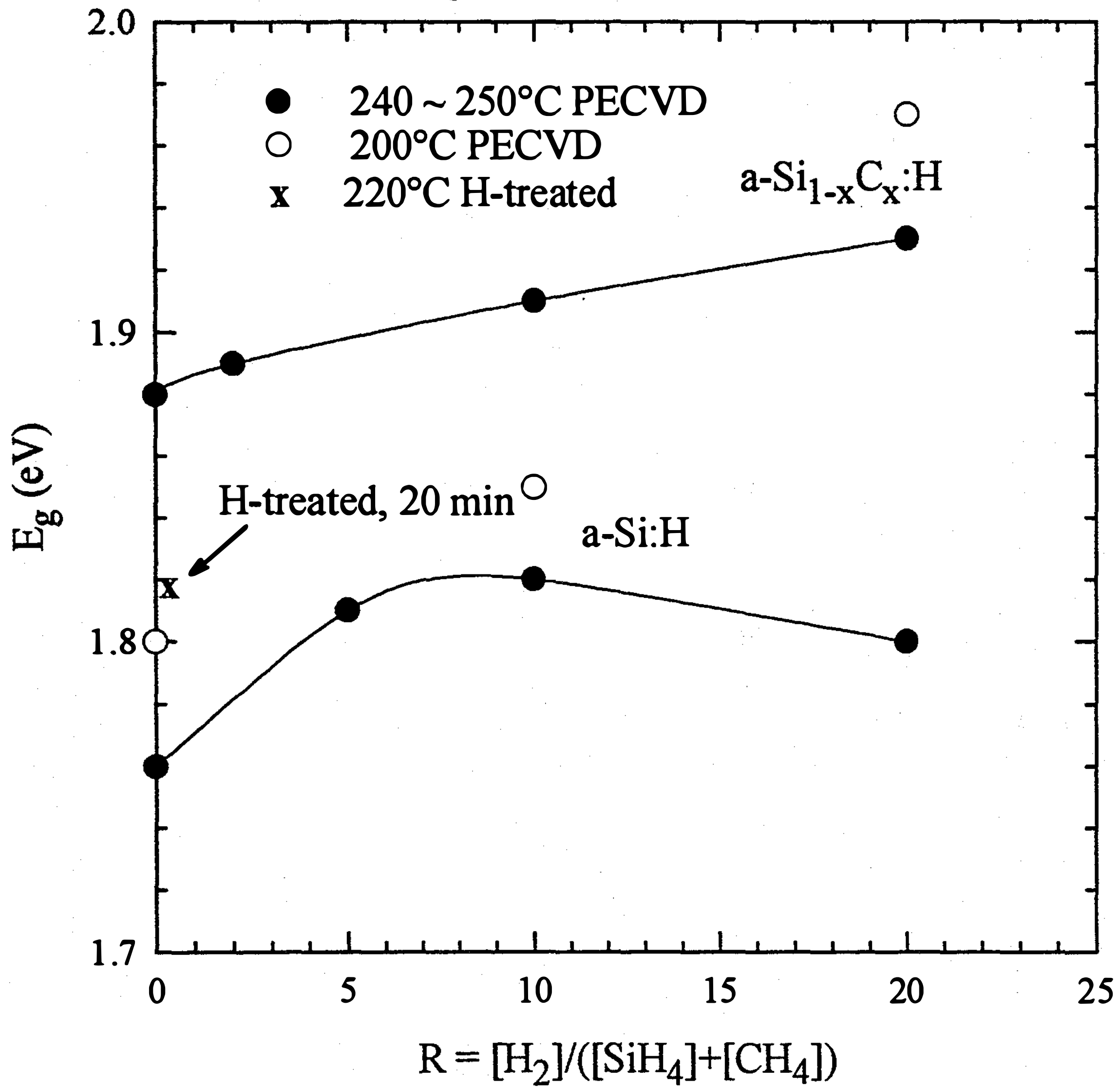

Fig. 15 E_{2000} versus H-dilution ratio R for a-Si:H and a-$Si_{1-x}C_x$:H prepared at 240 ~ 250°C (solid circles) and 170 ~ 200°C (open circles). Also shown at R = 0 is the estimated gap for an a-Si:H film prepared by alternating growth and H-treatment at a substrate temperature of 220°C.

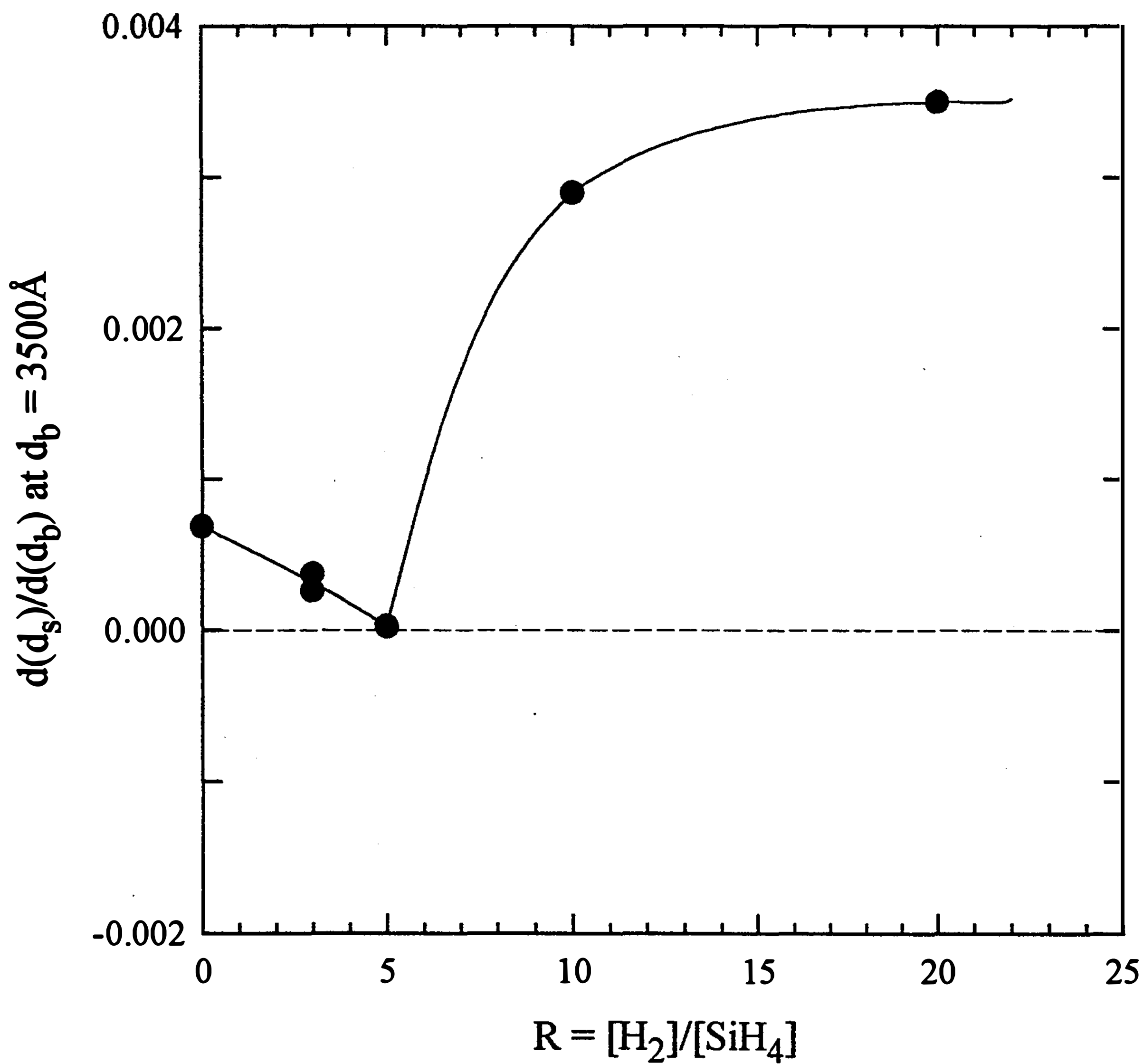

Fig. 16 Surface stability, defined as the rate of surface roughness increase with bulk film thickness in the thick film regime (d = 3500Å), for a-Si:H prepared as a function of H-dilution ratio $R = [H_2]/[SiH_4]$. The substrate temperature was 250°C. The partial pressure of SiH_4 was kept constant for this series at ~ 0.075Torr.

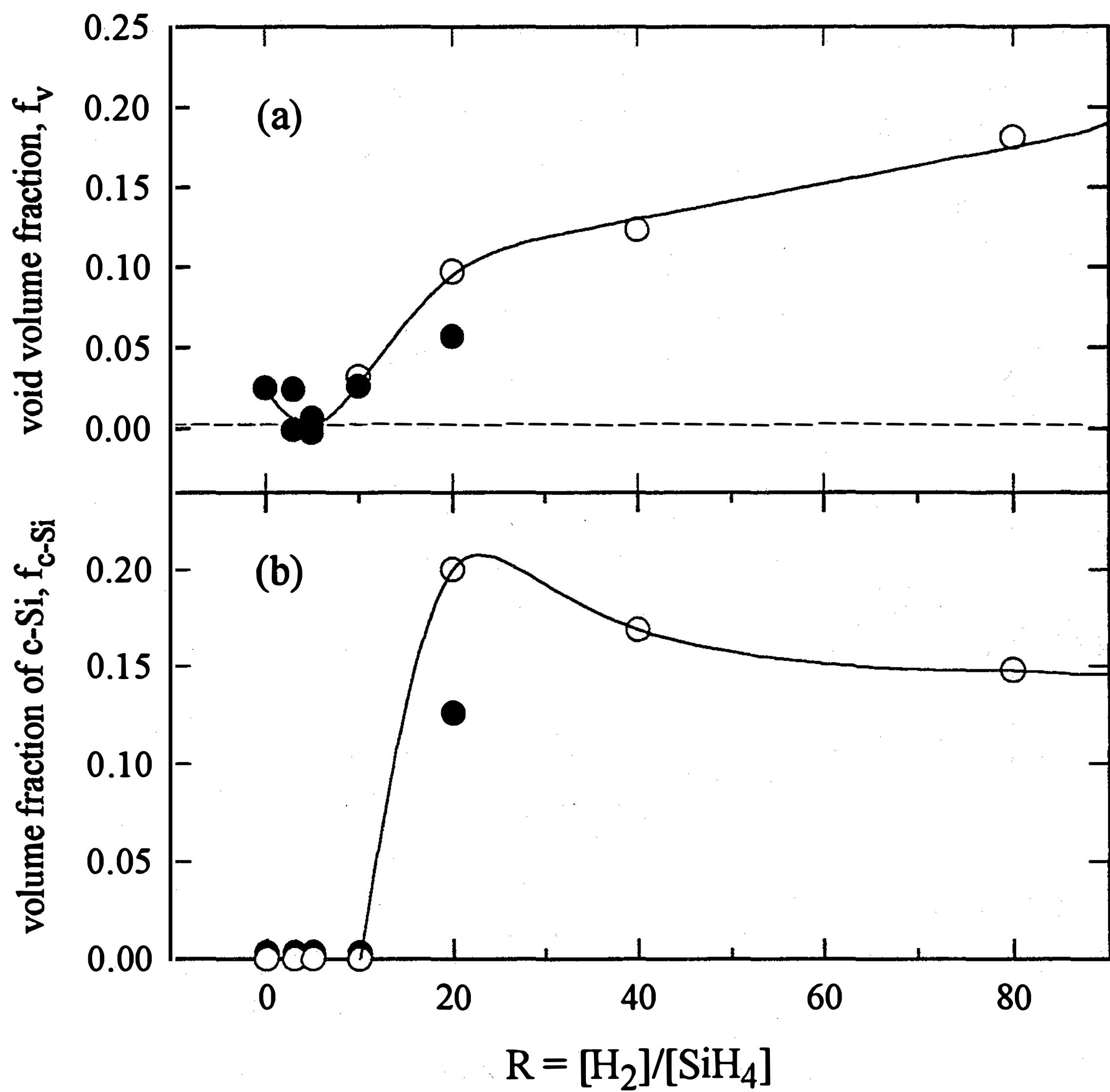

Fig. 17 (a) Void volume fraction and (b) crystalline silicon volume fraction as a function of R for the films of Fig. 16. The solid points are obtained at d=200Å, and the open points at the end of film deposition.

3. Solar Cells Optimized for Intrinsic Layer Performance

3.1 Midgap Baseline Cell Deposition Monitored by RTSE

The results reported in this part provide the first example in which the full structural evolution and optical properties of the *p*-layer, *p/i*-interface, *i*-layer, and *n*-layer have been determined from RTSE measurements collected during solar cell fabrication. In previous analyses, the *n*-layer was not studied since our single-chamber system used for RTSE studies did not have *n*-type doping capability. Recently this capability has been added, so we are now able to characterize the full cell. The full analysis procedure has been applied first to an optimum midgap a-Si:H baseline cell whose performance parameters were discussed in the previous quarter's report (efficiency 7.6%). The a-Si:H *p-i-n* baseline solar cell was prepared in the single-chamber system onto three types of substrates held at 200°C. Textured and specular SnO_2:F-coated glass was used for devices, while a specular SnO_2:F-coated Si wafer was used for RTSE with enhanced sensitivity. The plasma power-flux density was 70mW/cm^2 for the *p*-, *i*-, and *n*-layers. The a-$Si_{1-x}C_x$:H (x = 0.05 ~ 0.10) *p*-layer was prepared using flow ratios of [SiH_4]:[CH_4]:[B_2H_6]:[H_2] = 6:4:0.01:0.99 (in sccm) at a total pressure of 0.13Torr. Under these conditions, the formation of a metallic Sn layer via the reduction of the SnO_2:F by *p*-layer plasma hydrides is below detection limits (< 1Å). This is achieved by the combination of a low H-dilution (R ~ 0.1) and low substrate temperature (200°C). Upon termination of the *p*-layer, the gas flow and plasma were shut down nearly simultaneously in order to avoid CVD of a-Si:H:B from the *p*-layer gas mixture. However, a 50min Ar flush was needed after *p*-layer deposition, in order to reduce contamination of the *i*-layer with residual boron (B-carryover). For the *i*-layer, a-Si:H was deposited without H-dilution (*i.e.*, a midgap cell) using a 20sccm flow of SiH_4 at 0.19Torr. The a-Si:H *n*-layer was prepared using a flow ratio of [SiH_4]:[PH_3] = 10:0.2 (in sccm). To complete the devices, 1000Å Cr contacts were evaporated onto the *n*-layer *ex situ* (*i.e.*, in a different chamber than that used for cell preparation and RTSE studies).

Although we have presented information on RTSE analysis procedures in earlier reports, we will provide a brief review of those procedures used for solar cell analysis, focusing initially on the case of *p*-layer growth on the rough (although specular) SnO_2:F substrate films. For SnO_2:F the roughness is a characteristic of the polycrystalline structure. For rough substrates such as specular SnO_2:F, a more complicated optical analysis is required for overlying film growth than in the case of growth on smooth substrates such as c-Si, used in the nucleation study of the previous section. In Fig. 18, schematics of optical models representing (a) interface formation and (b) bulk layer growth are shown for a-$Si_{1-x}C_x$:H *p*-layer deposition on rough SnO_2:F. Model (a) is used before a well-defined a-$Si_{1-x}C_x$:H:B bulk layer has formed. Here, we assume that the roughness layer on the SnO_2:F can be described as a ~0.5/0.5 volume-fraction mixture of SnO_2:F/void using the Bruggeman effective medium theory. Initial film growth on SnO_2:F is then characterized by two parameters: (i) f_i, the volume fraction of a-$Si_{1-x}C_x$:H:B that

fills the modulations in the SnO_2:F roughness layer (yielding a three-phase ~0.5/f_i/(0.5-f_i) mixture of SnO_2:F/a-$Si_{1-x}C_x$:H:B/void of thickness d_i), and (ii) d_s, the thickness of the overlying a-$Si_{1-x}C_x$:H:B surface roughness layer, described as a 0.5/0.5 mixture of a-$Si_{1-x}C_x$:H:B/void. When f_i reaches its maximum value near 0.5, indicating that the SnO_2:F surface modulations are completely filled, then model (b) of Fig. 18 is used. In this case as well, two parameters characterize film growth: (i) d_s, the surface roughness layer thickness, again a 0.5/0.5 mixture of a-$Si_{1-x}C_x$:H:B/void, and (ii) d_b, the bulk layer thickness. Analysis of the (ψ, Δ) spectra throughout the two regimes of Fig. 18 requires determining at most two photon-energy-independent parameters at each time, either (f_i, d_s) or (d_s, d_b), and one time-independent pair of spectra, the complex dielectric function ε_p of the bulk a-$Si_{1-x}C_x$:H:B material. The analysis involves a minimization scheme that utilizes mathematical inversion to obtain ε_p and least-squares regression to obtain (f_i, d_s) or (d_s, d_b).

The upper two panels of Fig. 19(a) show the final results of this analysis for a-$Si_{1-x}C_x$:H *p*-layer growth on SnO_2:F at 200°C. The SnO_2:F bulk and surface layer thicknesses and dielectric function are deduced from an analysis of the (ψ, Δ) spectra prior to deposition ($t < 0$). The initial roughness layer thickness on the SnO_2:F is found to be ~ 105Å by minimizing interference- and substrate-related artifacts in the SnO_2:F dielectric function. In the first 40s of *p*-layer growth, an optical model that includes only the 105Å interface roughness layer is sufficient. In this time, f_i increases to 0.50, meaning that the interface layer composition changes from a 0.48/0.52 SnO_2:F/void mixture to a 0.48/0.50/0.02 SnO_2:F/a-$Si_{1-x}C_x$:H:B/void mixture. For $40 < t < 60$ s, the a-$Si_{1-x}C_x$:H:B surface roughness layer must be added, and it increases in thickness to 85Å. For $t > 60$s, the bulk layer must be added since the interface modulations are completely filled with a-$Si_{1-x}C_x$:H:B, *i.e.*, $f_i = 0.52$. The bulk layer thickness increases linearly at a rate of 1.47Å/s, and in this regime the *p*-layer exhibits a smoothening trend as the substrate-induced roughness is dampened out. When extrapolated back to $t = 0$, this trend yields a value close to the initial SnO_2:F roughness thickness. At the end of *p*-layer deposition, we found: d_i = 105Å, d_b = 112Å, and d_s = 75Å, for an effective thickness of 0.52(105) + 112 + 0.50(75) = 204Å. This value is in excellent agreement with the intended thickness (200Å). The lower panel of Fig. 19(a) shows the dielectric function of the *p*-layer (inset) obtained along with the microstructural parameters in the analysis. The optical gap is determined using the method of Cody as shown in the main part of the panel. The resulting 200°C optical gap of 1.72eV obtained by the Cody method is in general ~ 0.18eV lower than the 25°C Tauc gap. (Thus, the predicted 25°C Tauc gap of the *p*-layer is 1.90eV.)

The optical model is sufficiently complex that some independent corroboration of the analysis results is needed. First, we have found that the roughness layer thicknesses (d_s) on a-$Si_{1-x}C_x$:H films deduced by RTSE correlate with those measured *ex situ* by atomic force

microscopy (AFM) in accordance with the relationship: $d_s = 1.4d_{rms}(AFM) + (4Å)$. The slope (1.4) indicates that the optically deduced roughness is closer to a peak-to-peak value, while the intercept (4Å) may reflect differing sensitivities of AFM and RTSE. Second, the roughness value for the SnO_2:F measured by AFM and that estimated by RTSE (from the extrapolation of the *p*-layer smoothening trend) also obey this same relationship. Third, we found that the Cody method optical gap of Fig. 11(a) (1.72eV) is within 0.01eV of the corresponding value deduced from *ex situ* transmission and reflection measurements of a thicker film at 25°C (1.80eV), taking into account the -5×10^{-4}eV/K gap shift with temperature. This observation demonstrates consistency in that earlier studies have suggested that, for bulk-like amorphous semiconductor films (not clusters), the optical gap is independent of thickness. Thus, the three observations enumerated above suggest that the roughness evolution and optical gap obtained using the three-layer model are correct. An accuracy of ~ 5% is estimated for the roughness thicknesses; as will be seen, the precision is ±0.2 Å.

An analysis approach similar to that of the *p*-layer has been used to study: (i) *i*-layer growth, (ii) *n*-layer growth, and (iii) *p/i* interface contaminant layer formation during Ar gas flushing, as shown in Figs. 19(b)-(c) and 20, respectively. For the *i*- and *n*-layers, the insets in Figs. 19(b) and (c) depict a wider range of d_b, including plasma termination. Although the interpretation of these results parallel those of Fig. 19(a), the *p/i* interface layer formation of Fig. 20 deserves further comment. The *p/i* interface layer is ascribed to contaminants that accumlate on the *p*-layer surface during the Ar flush. The key parameter here is the effective layer thickness, given by $f_i d_i + 0.5 d_s$. For the solar cell of Fig. 19 prepared at 200°C, the average growth rate in the first 5min and the final effective thickness of the contaminant layer are 0.2Å/min and 1.7Å. For the previous "best" cell prepared at 250°C using an identical *p/i* interface formation procedure, the corresponding values are 0.5Å/min and 3.8Å (open triangles in Fig. 20). These results are consistent in that greater contamination from the internal chamber components is expected at higher temperature. Because of the thinness of the contaminant layer, the gap value in the lower part of Fig. 20 should be considered only an estimate of its absorption onset energy.

For the 200°C solar cell prepared on textured SnO_2:F, the short-circuit current, open-circuit voltage, fill-factor, and efficiency were respectively (12.9mA/cm^2, 0.83V, 0.71, and 7.6%). The corresponding parameters for the previous best cell prepared at 250°C were (13.7mA/cm^2, 0.74V, 0.65, and 6.6%). It is well known that the cell parameters are very sensitive to the nature of the p/i interface. Thus, the thicker contaminant layer in the 250°C cell may account in part for its poorer performance, especially in view of the low energy absorption onset for the layer, which indicates a high density of states at the *p/i* interface below the *p*- and *i*-layer bandgaps. Ascribing the poorer performance to the interface layer for the cell prepared at 250°C is reasonable since the fundamental properties of the midgap a-Si:H *i*-layer prepared without H-dilution do not degrade significantly as the substrate temperature is increased from 200 to 250°C. Overall, the example of Fig. 20 shows how RTSE is now providing a better understanding of the

relationships between monolayer-level interface structure and device performance that is inaccessible to *ex situ* characterization tools.

To summarize this part, Table 2 reveals the final data for the layered structure and optical gaps of the 200°C and 250°C cells discussed in the above paragraphs. For the latter, the n-layer was not monitored since it was prepared in a different deposition reactor in order to complete the device. (In this case, it was ascertained based on experiments with control cells that the sample transfer through the ambient, followed by a weak acid etch to remove contaminants, did not degrade the device performance.) Some points regarding the data in Table 2 deserve comment. First, the B- and P-doped layer thickness are remarkably close to the intended values of 200Å and 300Å, respectively. The largest deviation is 7Å for the n-layer of the 200°C cell. The average error for the three doped layers monitored by RTSE is 2.4%. This result suggests that we have our doped layer processes well under control. The error for the two *i*-layers is significantly larger, 12 ~ 14%, indicating that the deposition rate used in timing the *i*-layers has been overestimated. Such errors can be corrected in the next cell iteration since an updated, more accurate deposition rate can be obtained from the data for the cells of Table 2. Finally, we want to point out that the attractiveness of RTSE is the ability to deduce the final effective thicknesses, deposition rates, and optical gaps of the separate *p*-, *i*-, and *n*-layers *in the actual cell configuration*, rather than from separate layers deposited independently.

3.2 Widegap Baseline Cell Deposition Monitored by RTSE

We have fabricated a series of solar cells incorporating ~ 2000Å widegap a-$Si_{1-x}C_x$:H (~ 1.95eV) *i*-layers prepared using different H-dilution ratios. In addition to the specular SnO_2:F covered c-Si substrates used for RTSE with enhanced sensitivity, the solar cell deposition was performed simultaneously on three glass substrates coated with different TCO's for device measurements: specular SnO_2:F, textured SnO_2:F, and specular ZnO. These cells were fabricated at 200°C using similar processing procedures as developed for the midgap baseline cell described in the previous section. However, one exception was the use of TMB instead of diborane as the *p*-type doping source in an attempt to reduce *p/i* interface contamination. Thus, the *p*-layer was prepared using the following mixture: $[SiH_4]:[CH_4]:[B(CH_3)_3]:[He]$ = 6:4:0.02:0.98, with all other deposition parameters fixed at the values for the *p*-layer of the midgap baseline cell noted in the previous section. In the preparation of the *p*-type material from TMB, the doping gas was diluted in He rather than in H_2, and a factor of two higher flow was used to account for the TMB molecule containing one boron atom versus two for diborane. The widegap a-$Si_{1-x}C_x$:H *i*-layers were prepared as a function of R using the formula developed in earlier optimization studies. The plasma power flux density was 78mW/cm^2, and the partial pressure of the source gases $[SiH_4]+[CH_4]$ was fixed at 0.075Torr, leading to an increase in gas pressure to ~ 0.5Torr as $R = [H_2]/\{[SiH_4]+[CH_4]\}$ is increased to 20.

Fig. 21(a) and (b) show typical single photon energy (2.45eV) trajectories for the full widegap solar cells having i-layers prepared with R = 10 and 20. The *p*-layer, *p-i* interface,

i-layer, and *n*-layer can all be discerned. At this point, we have not completed analysis of the full RTSE data sets corresponding to these trajectories (as was done for the midgap cell of the previous section), however, we have made a rather crude assessment of the magnitude of the *p-i* interface problem which will be discussed further below. In Table 3, we present the initial performance parameters for the widegap solar cells. Including results for the three different TCO's and four values of R: R = 2, 5, 10, and 20. The results also appear graphically in Figs. 22 and 23. As discussed in previous reports the cell prepared with R = 20 should show the best performance, assuming that best *i*-layer properties [*e.g.*, lowest α(1.2eV), lowest Urbach slope E_U] translate into the best solar cell performance. In fact, for cells deposited on specular ZnO, this expectation is closest to being be borne out since R = 20 yielded the best combination of initial V_{oc} (0.90V) and fill-factor (0.56). For cells deposited on specular SnO_2:F, R = 10 yielded the best combination (0.92V, 0.67). The latter cell yielded the best overall initial efficiency (~ 4%) among all those prepared on three different TCO's with different values of R from 2 to 20. The overall best V_{oc} (0.93V) was obtained for the cell prepared with R = 5 on specular SnO_2:F.

Table 2 Information deduced from RTSE studies of a-Si:H *p-i-n* solar cell preparation on SnO_2:F at two substrate temperatures. For the 250°C cell, the n layer deposition was not monitored. The final solar cell characteristics were measured from a cell co-deposited onto textured SnO_2:F along with the specular substrate used for RTSE. Note that the optical gaps are characteristic of the substrate temperatures used in the processes.

	250°C a-Si:H solar cell			200°C a-Si:H solar cell			
	p	*p/i*	*i*	*p*	*p/i*	*i*	*n*
RTSE Results							
Optical Gap[+] (eV)	1.65	1.3*	1.56	1.72	1.24*	1.62	1.59
Interface Roughness Thickness (Å)	98	---	67	105	---	75	25
Final Bulk Layer Thickness (Å)	111	0	4250	112	0	4312	283
Final Surface Roughness Thickness (Å)	67	3	21	75	1	25	22
Effective Layer Thickness (Å)	194	3.8	4294	204	1.7	4361	307
Intended Thickness (Å)	[200]	[0]	[5000]	[200]	[0]	[5000]	[300]
Bulk Layer Deposition Rate (Å/s)	1.53	0	1.0	1.47	0	1.21	1.47
Solar Cell Characteristics							
Short Circuit Current (mA/cm^2)			13.7			12.9	
Open Circuit Voltage (V)			0.74			0.83	
Fill-Factor			0.65			0.71	
Efficiency (%)			6.6			7.6	

\+ The optical gaps reported here are obtained from $\varepsilon_2^{1/2}$ plots. At 200 and 250°C, these values are ~ 0.18 and 0.20eV narrower than the conventional Tauc optical gaps at 25°C, respectively.

* Because of the thinness of these layers, this should be interpreted as an absorption onset, and not as a true gap within the material.

Table 3 Initial performance parameters, including the open-circuit voltage, short-circuit current, fill-factor and efficiency for widegap *p-i-n* solar cells incorporating 2000Å a-$Si_{1-x}C_x$:H *i*-layers. In this series the H-dilution level for the *i*-layer was the only variable parameter in the cell preparation. Results are provided for four values of the H-dilution ratio R = $[H_2]/\{[SiH_4]+[CH_4]\}$: 2, 5, 10, and 20, and three different TCO's: specular SnO_2:F, textured SnO_2:F, and ZnO.

preparation	substrate	V_{OC} (V)	J_{SC} (mA/cm^2)	FF	EFF.
200°C, TMB p	specular SnO_2:F	0.88	5.6	0.61	3.0
a-SiC:H i-layer	textured SnO_2:F	0.88	5.7	0.53	2.7
R = 2	specular ZnO	0.78	5.8	0.47	2.1

preparation	substrate	V_{OC} (V)	J_{SC} (mA/cm^2)	FF	EFF.
200°C, TMB p	specular SnO_2:F	0.93	5.6	0.62	3.2
a-SiC:H i-layer	textured SnO_2:F	0.88	6.3	0.52	2.9
R = 5	specular ZnO	0.89	6.7	0.52	3.1

preparation	substrate	V_{OC} (V)	J_{SC} (mA/cm^2)	FF	EFF.
200°C, TMB p	specular SnO_2:F	0.92	6.4	0.67	3.9
a-SiC:H i-layer	textured SnO_2:F	0.88	7.6	0.56	3.7
R = 10	specular ZnO	0.87	7.6	0.57	3.8

preparation	substrate	V_{OC} (V)	J_{SC} (mA/cm^2)	FF	EFF.
200°C, TMB p	specular SnO_2:F	0.88	5.8	0.56	2.9
a-SiC:H i-layer	textured SnO_2:F	0.87	7.2	0.54	3.4
R = 20	specular ZnO	0.90	6.9	0.56	3.5

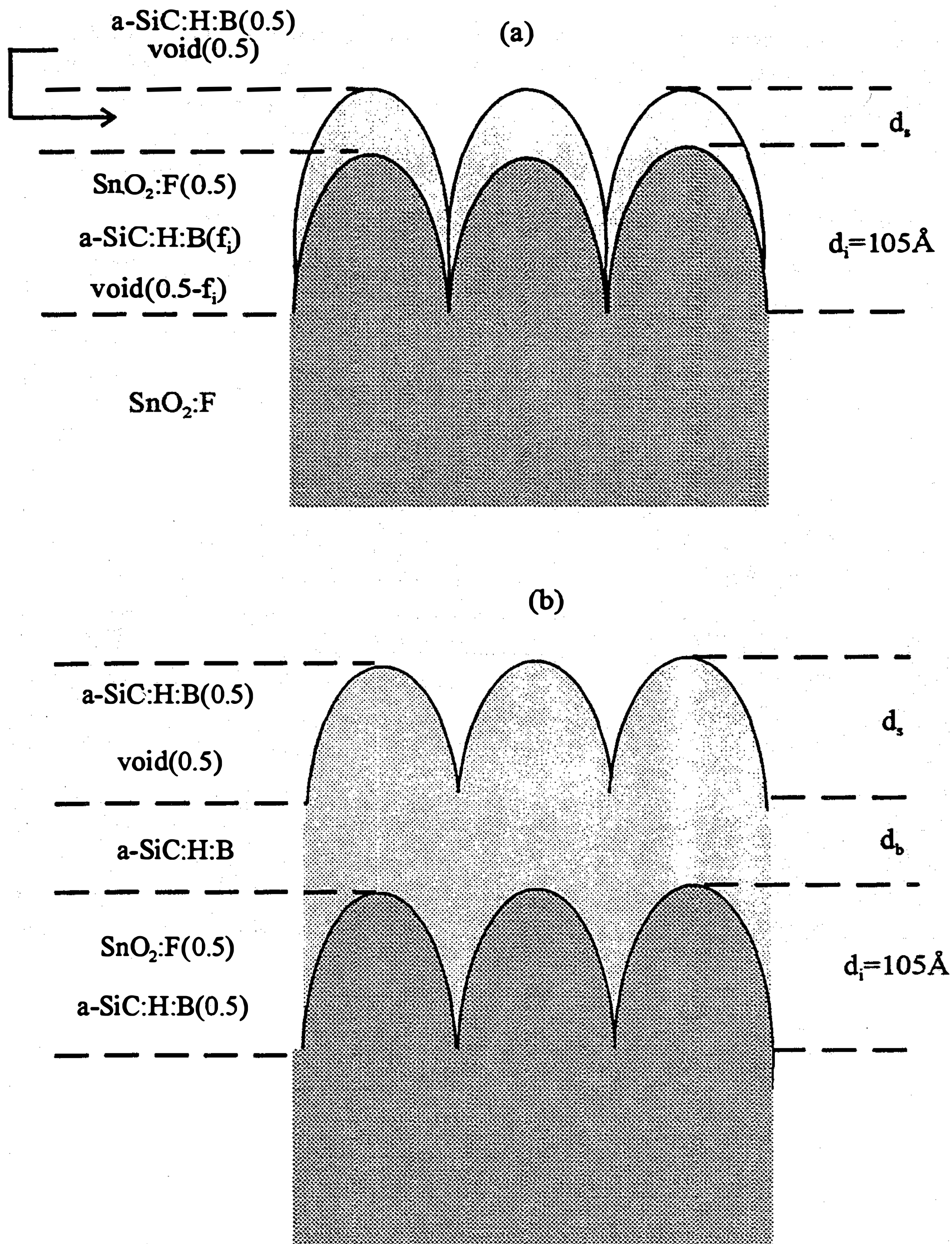

Fig. 18 Schematic optical models of (a) interface formation and (b) bulk layer growth regimes for a-$Si_{1-x}C_x$:H:B deposited on specular (but rough) SnO_2:F. In (a) two free parameters used in the model: f_i, the volume fraction of a-$Si_{1-x}C_x$:H filling the modulations in the SnO_2:F surface roughness layer and d_s, a low density a-$Si_{1-x}C_x$:H surface roughness layer induced by the SnO_2:F roughness. In (b), two free parameters are also used: d_s and d_b, the latter being the bulk layer thickness. All roughness layers (d_s) are modeled as ~ 0.5/0.5 mixtures of bulk materials/void.

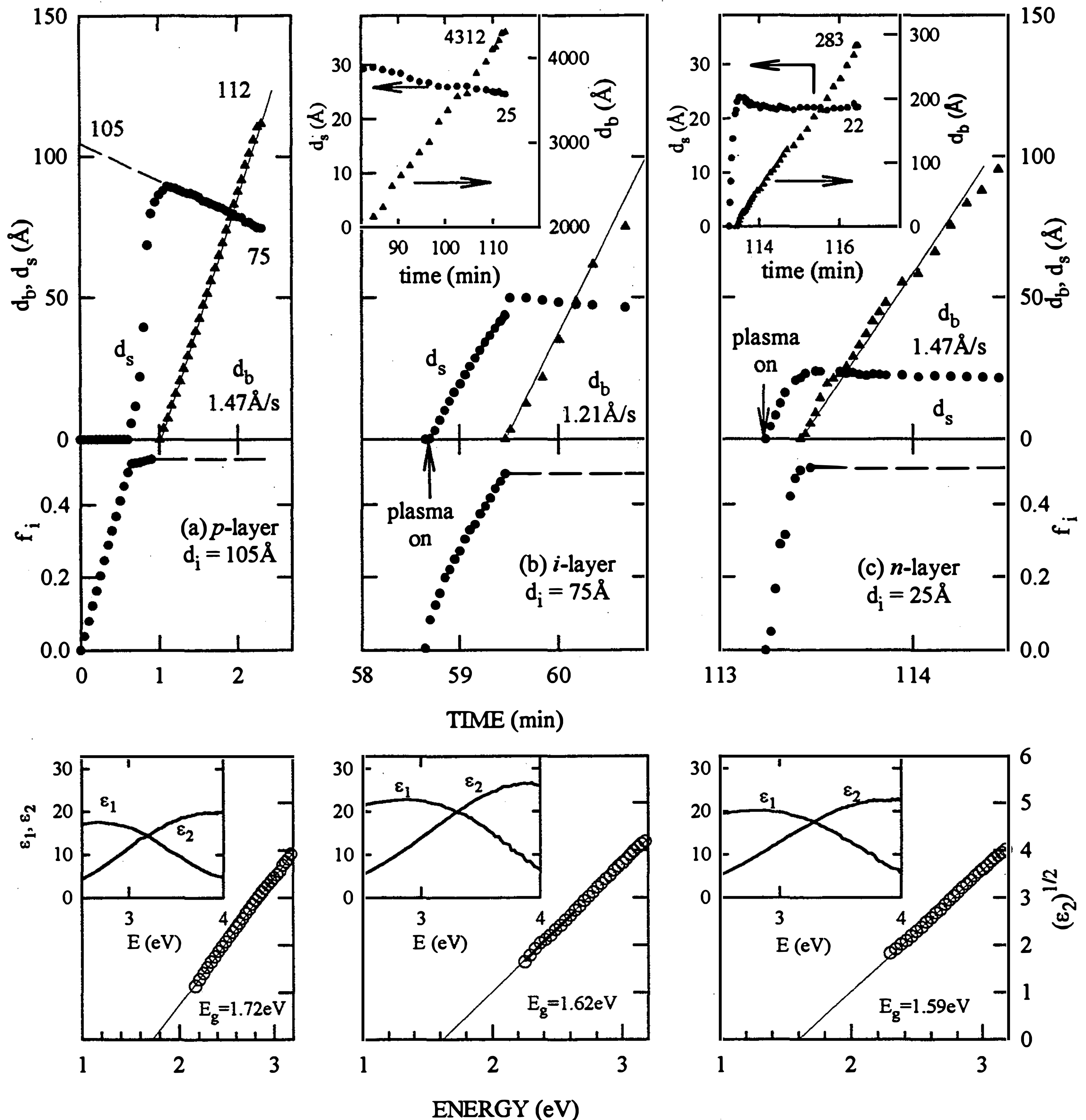

Fig. 19 Layer thicknesses and volume fractions (upper panels), and optical properties at 200°C (lower panels) obtained in a post-deposition analysis of RTSE data acquired during solar cell fabrication. Results are provided for: (a) B-doped a-$Si_{1-x}C_x$:H; (b) undoped a-Si:H; and (c) P-doped a-Si:H. The thicknesses d_s, d_i, and d_b are for the surface and interface roughness and bulk layers, respectively, and f_i is the volume fraction of the film that forms within the modulations of the substrate film roughness. Values in the figures correspond to final layer thicknesses, bulk layer deposition rates, and optical gaps.

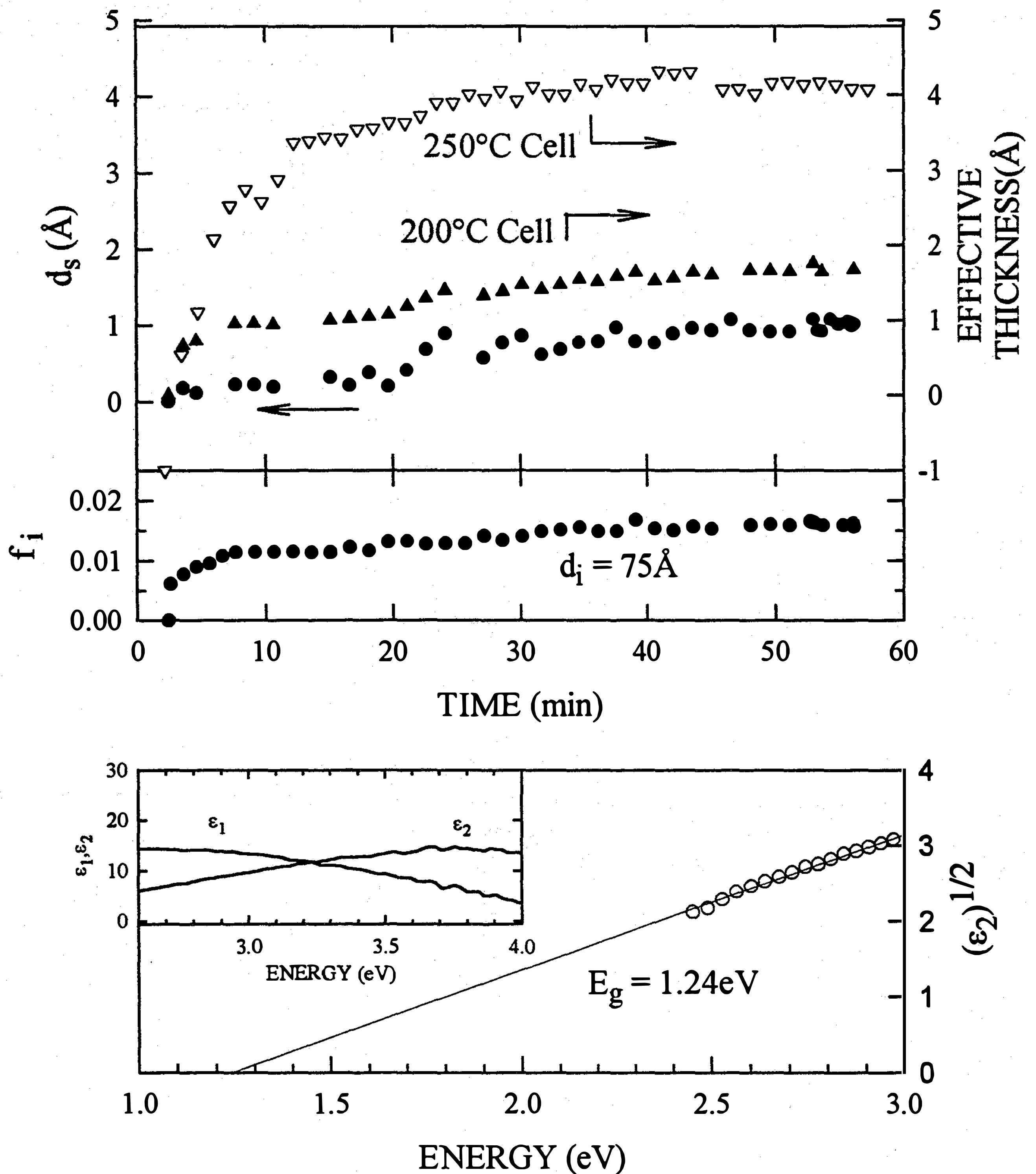

Fig. 20 Layer thicknesses and volume fractions (top panels) deduced from RTSE data collected during ~ 50mins of Ar flushing when p/i interface contamination occurs. The thicknesses d_s, and d_i are for the contaminant and substrate surface roughness layers and f_i is the volume fraction of contaminant forming within the substrate roughness modulation. All results were obtained on the solar cell of Fig. 19 prepared at 200°C, with the exception of the open triangles in the effective thickness ($f_i d_i$+0.5d_s), which are obtained at 250°C. Optical data for the contaminant layer appear in the lower panel.

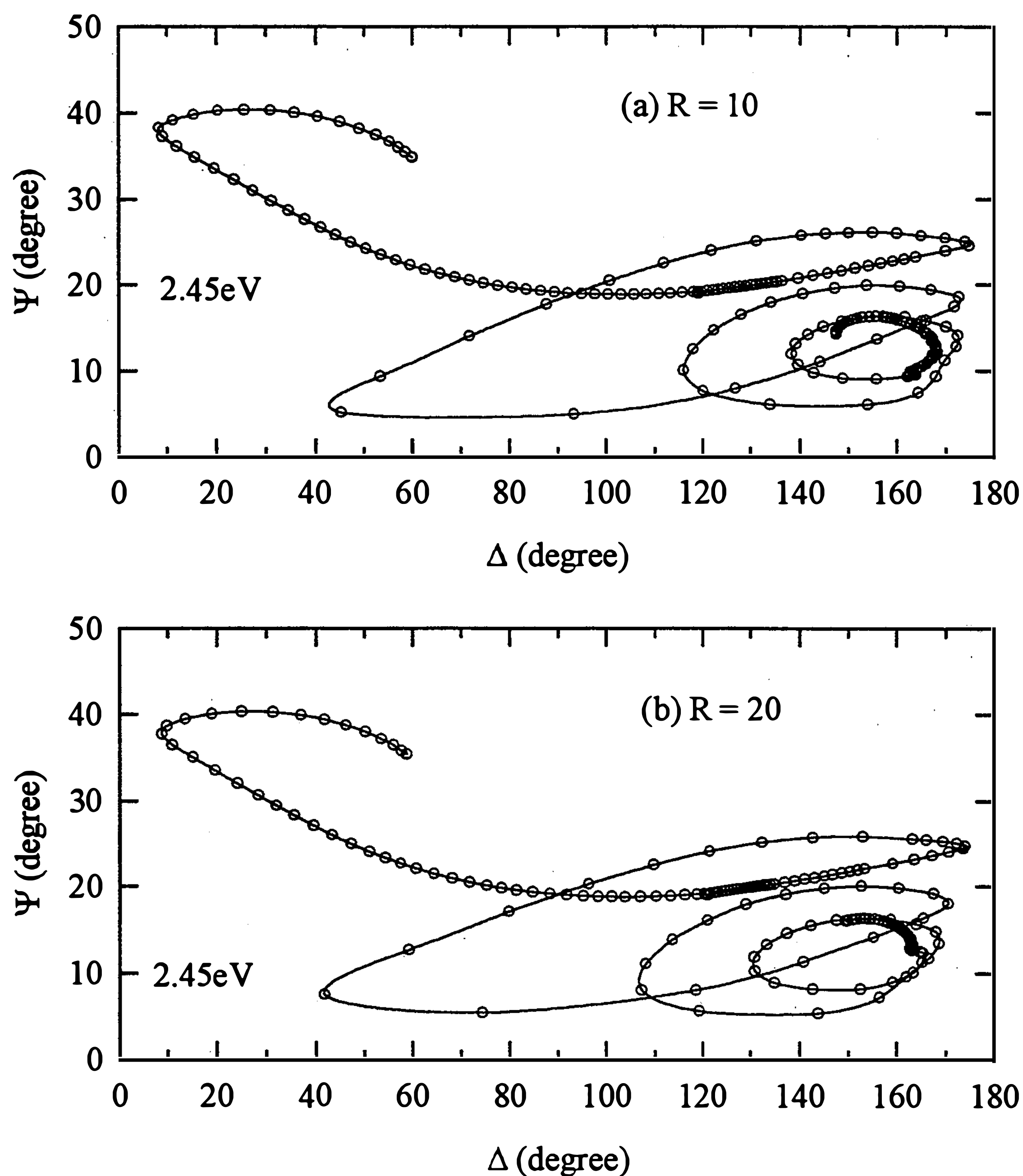

Fig. 21 Trajectories in the ellipsometric angles (Ψ,Δ) for the growth of two *p-i-n* solar cells incorporating widegap a-$Si_{1-x}C_x$:H *i*-layers. In (a) the H-dilution ratio of the *i*-layer R = $[H_2]/\{[SiH_4]+[CH_4]\}$ is 10 and in (b) R = 20. In both cases the i-layer is prepared using a $[CH_4]/[SiH_4]$ flow ratio of 2/3.

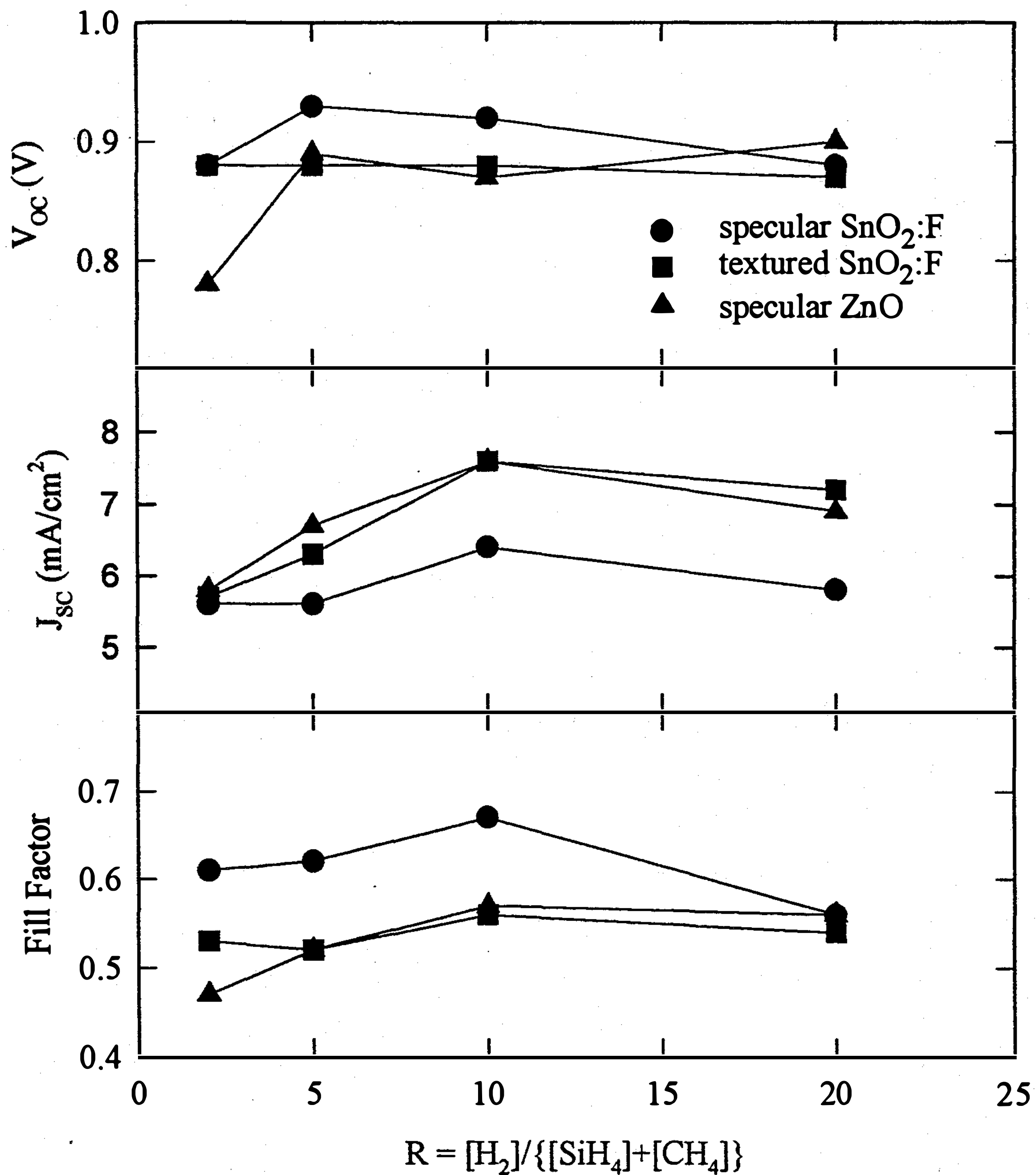

Fig. 22 Initial performance parameters, including the open-circuit voltage, short-circuit current density, and fill factor for a series of *p-i-n* solar cells incorporating 2000Å widegap a-$Si_{1-x}C_x$:H *i*-layers prepared as a function of H-dilution ratio. H-dilution ratio. Results are presented for cells prepared on three types of substrates, glass coated with: (i) specular SnO_2:F, (ii) textured SnO_2:F, and (iii) specular ZnO.

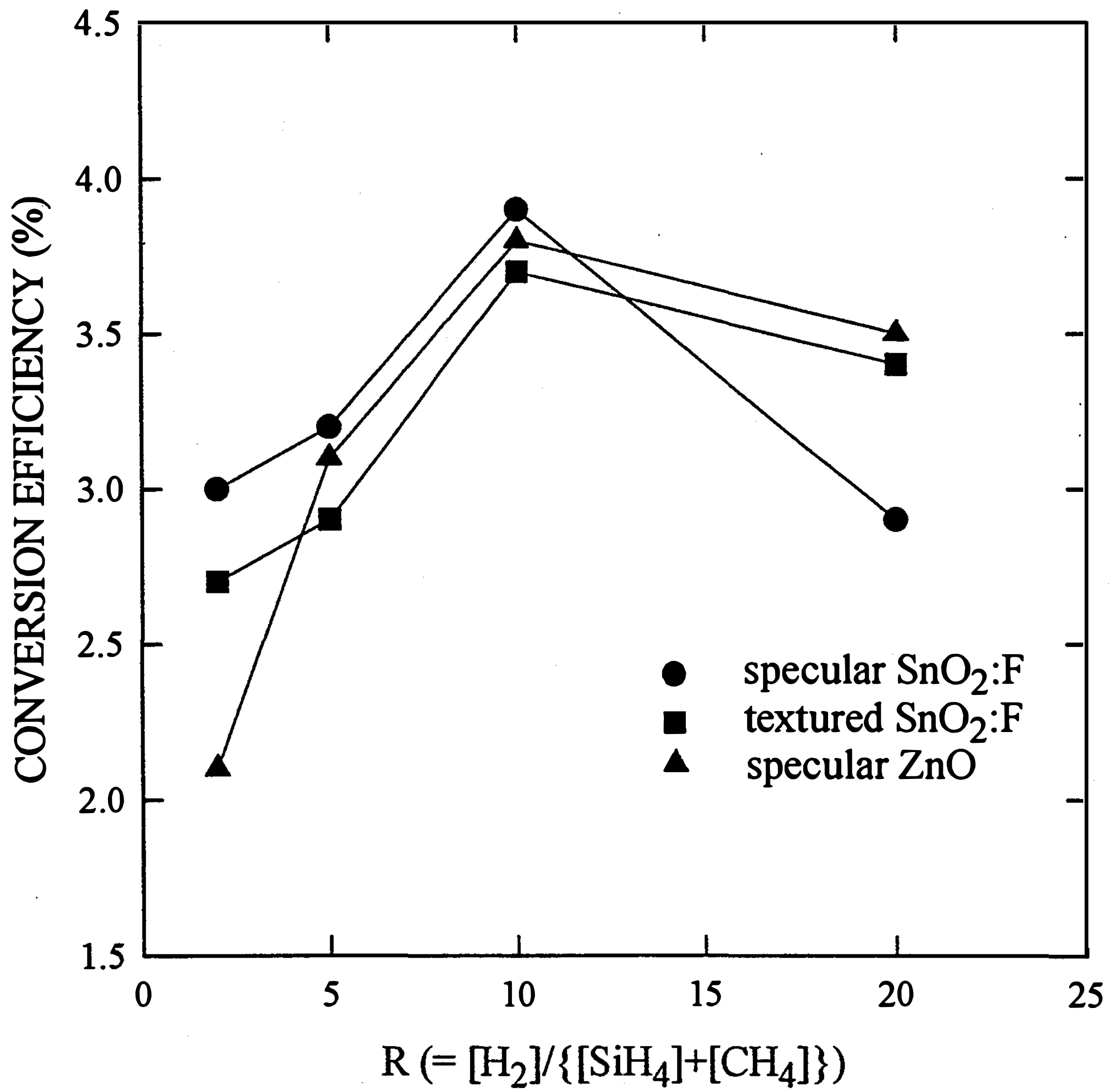

Fig. 23 Initial efficiency for a series of *p-i-n* solar cells incorporating 2000Å widegap a-$Si_{1-x}C_x$:H *i*-layers prepared as a function of H-dilution ratio R.

4. P-type Layer Optimization

4.1 Hydrogen Treatments for Widegap *p*-type Layers

Novel *p*-layer preparation is motivated by the fact that there are a number of problems with conventional *p*-layers in a-Si:H based solar cells in the superstrate configuration. First, because H-rich plasmas degrade the conventional SnO_2:F TCO, low-absorption microcrystalline layers cannot be used. Thus, the bandgap is widened through alloying with carbon. Unfortunately, incorporating the dopant atoms leads to a reduction in the gap that negates the effect of alloying. Second, because the *p*-type layer is deposited first, B-related species can contaminate the surface of the *p*-layer and the overlying *i*-layer, even in load-locked multi-chamber systems in which the *p*-chamber must be flushed before transferring the sample to the *i*-chamber. We are developing an atomic H treatment at the *p-i* interface that may be able to correct both of these problems without significantly damaging the underlying textured TCO. The role of the H-treatment is (i) to remove dopant-related species from the *p*-layer surface and (ii) to passivate defects throughout much of the *p*-layer, in an attempt to widen the gap. The results of this study are included in Fig. 24 and in Tables 4 to 6.

In the initial study we concentrated on two 300Å *p*-layers which were deposited on c-Si. One sample was measured in the as-deposited state, whereas the other underwent an *in situ* filament-generated H-treatment immediately after deposition. The optical properties were monitored during the treatment, and the resulting data were analyzed using a reaction-limited model to determine the volume fraction of the modified material within the film. This volume fraction is proportional to the density of broken Si-Si bonds in the network. The results are plotted continuously as a function of time in Fig. 24. Here, the filament is ignited at a time of 10min, and is extinguished after a 25min treatment. The volume fraction of modified material increases to ~ 0.13 during H-treatment, and about 0.01 of this material reverts back to the original state upon extinguishing the filament. These results indicate that the effect of the H-treatment is to convert a fraction of Si-Si bonds to Si-H bonds in a reaction-limited fashion throughout the thickness of the film. A small fraction of the broken Si-Si bonds re-form once the source of atomic H is removed.

In Tables 4 and 5 we show the kinetic coefficients for H-trapping in three samples of a-Si:H(:B). In general as shown in Table 4, we find that fast and slow reaction rates for hydrogenation coexist in a-Si:H. In samples with a high void volume fraction the fast reaction rate dominates, whereas in optimum a-Si:H the slower reaction rate dominates. Doped materials show similar contributions from both fast and slow rates - an indication that voids may play a role in the hydrogenation behavior of this material. As shown in Table 5, we conclude that a large fraction of the Si-H bonds introduced into the a-Si:H and a-Si:H:B are stable on the time scales needed to cool the sample and freeze-in the new H-structure. Thus, the H-exposed material remains modified as it is brought to room temperature and removed from the chamber.

The properties of this modified a-Si:H:B material have been studied for comparison with the as-deposited material, and with conventional a-$Si_{1-x}C_x$:H:B materials presently used for solar cells prepared both in single and multiple chamber systems in our laboratory. These results are included in Table 6. The results show that the H-modified material is expected to be superior overall to the a-$Si_{1-x}C_x$:H:B. For example, in order to achieve an equivalent room temperature conductivity of 3×10^{-5}S/cm, sufficient B must be incorporated into a-$Si_{1-x}C_x$:H to reduce the gap to 1.75eV, which is ~ 0.16eV lower than that of the H-modified material without carbon. One might expect that H-modified a-$Si_{1-x}C_x$:H:B would be even superior to H-modified a-Si:H:B. However, atomic H has a weaker modifying effect on the alloys, possibly because of the stabilizing influence of carbon and also the presence of Si-CH_3 bonding units which relax the network.

There is a possibility that this approach could fail due to damage of the underlying TCO by diffusing H. Our experience is that ZnO or textured SnO_2:F may be less susceptible to this effect. If significant improvement is obtained, we expect to push the technique further by using higher levels of H that may crystallize the near surface *p*-layer. This could lead to an improved *p-i* interface and reduced optical absorption. Obviously if crystallization can be performed to a greater depth, then there will be a better chance of significant performance improvement. This may be achieved with higher atomic H concentrations at the surface than is possible with a heated filament. As a result, we are also in the process of utilizing a microwave-plasma rather than a heated filament for H generation.

4.2 TMB as *p*-type Layer Source Gas

The studies described in Sec. 3.1 (to be discussed in greater detail in Secs. 5.2 and 5.3) have suggested that limitations in the performance of *p-i-n* solar cells prepared both in our single- and multi-chamber systems may arise from monolayer-level contamination of the *p*-layer surface that occurs during the flushing of the chamber before deposition of the *i*-layer. Two changes in our process procedure for cell preparation in the single-chamber system have been adopted in an attempt to characterize improved cells using our RTSE probe. The first improvement is the reduction in the substrate temperature during cell preparation from 250°C to 200°C which reduces the interface contamination thickness as shown in Sec. 3.1. The second improvement is the incorporation of TMB as the gas source instead of B_2H_6. It has been shown that TMB is more stable and results in less contamination at the TCO/*p* and *p*/*i* interfaces during the cell fabrication.

Table 7 shows the characteristics of our *p*-type layers developed for incorporation into solar cells prepared in the single chamber system used for RTSE monitoring. The deposition temperature was 250°C, except for the last two entries. This table emphasizes that for all conventional *p*-type materials the activation energy, E_σ tracks the Tauc gap E_{Tauc} such that (E_{Tauc} -E_σ) is nearly constant between 1.32 and 1.39eV. Also included in this trend are the materials prepared at lower T_S and with TMB. The only sample that is

significantly outside this trend is the material prepared without any carbon alloying, but with an *in situ* hydrogen treatment after deposition. In this case, (E_{Tauc} -E_{σ}) is 0.15eV larger than for any a-$Si_{1-x}C_x$:H:B materials. Furthermore the H-treatment over-compensates for the gap-narrowing typically observed with doping.

Our next step was to try to incorporate H-treated *p*-type material in the solar cell configuration. In this case, however, we applied the H-treatment to *p*-type a-$Si_{1-x}C_x$:H:B, expecting that the lower penetration depth of H in this material would better protect the SnO_2:F from reduction. Figure 25 and Table 8 summarize the results of this study, including the light I-V's and solar cell characteristics in the initial state for a control cell and two cells that were prepared on textured SnO_2:F using two different atomic H-treatments which were performed just after *p*-layer deposition and chamber flushing. The two treatments were characterized by different filament powers, 9.2W which hydrogenates the bulk *p*-layer without any appreciable etching, and 28W which both hydrogenates the bulk and etches the top few monolayers of the *p*-layer. Thus, the role of these treatments was twofold: first, to remove any monolayer contamination from the Ar flushing (at 28W), and second to hydrogenate the *p*-layer in an attempt to widen its gap while retaining high conductivity as in Table 7 (both 28 and 9W). It is clear that these attempts failed presumably because of reduction of the SnO_2:F underlying the *p*-layer by the diffusing H. It is interesting, however, that the failure occurs primarily through a reduction in fill factor. We expect to perform similar experiments in the future using pure a-Si:H for the *p*-layer and ZnO for the TCO.

Table 4 Kinetic coefficients for the *in situ* hydrogenation of samples of a-Si:H and a-Si:H:B. These coefficients are defined through the equation:

$f(t) = f_{oo}\,[1 - f_{of}\exp(-\alpha_f t) - f_{os}\exp(-\alpha_s t)]$,

where α_j and f_{oj} (j = f, s) are the rate constants and normalized amplitudes for H incorporation through fast and slow pathways.

Sample	$\alpha_f\,(s^{-1})$	$\alpha_s\,(s^{-1})$	f_{of}	f_{os}
a-Si:H (opt.)	0.0050	0.00067	0.07	0.93
a-Si:H (5% void)	0.0032	–	1	0
a-Si:H:B	0.0053	0.00065	0.52	0.48

Table 5 Kinetic coefficients for de-hydrogenation of samples of a-Si:H and a-Si:H:B. These coefficients are defined through the equation:

$f(t) = f_{oo}\,[f_{stable} + f_{of}\exp(-\alpha_f t) + f_{os}\exp(-\alpha_s t)]$,

where α_j and f_{oj} (j = f, s) are the rate constants and normalized amplitudes for H emission from deep traps.

Sample	$\alpha_f\,(s^{-1})$	$\alpha_s\,(s^{-1})$	f_{of}	f_{os}	f_{stable}
a-Si:H (opt.)	0.004	4.00E–4	0.055	0.110	0.835
a-Si:H:B	0.008	3.96E–12	0.082	0.039	0.879

Table 6 Selected properties of p-type amorphous semiconductor films, including as-deposited and H-modified a-Si:H:B, and conventional a-$Si_{1-x}C_x$:H:B. The properties include the Tauc optical gap at room temperature, the conductivity

Sample	$\frac{B_2H_6}{SiH_4 + CH_4}$	Eg(Tauc, 25 °C (eV)	E_{act} (eV)	σ(RT) ($\Omega^{-1}cm^{-1}$)
a-Si:H:B (as-dep.)	0.001	1.73	0.34	1.6E–4
a-Si:H:B (H-treat.)	0.001	1.91	0.39	3.0E–5
a-SiC:H:B (as-dep.)	0.001	1.85	0.48	8.6E–6
a-SiC:H:B (as-dep.)	0.005	1.75	0.43	4.0E–5

Table 7 Comparison of the electrical properties of a-$Si_{1-x}C_x$:H:B prepared using a TMB-based *p*-type gas mixture, $[SiH_4]:[CH_4]:[H_2]:[B(CH_3)_3]$ = 6:4:10:0.1, at 200°C (fifth row), with other *p*-layer preparations described in this report (T_S = 240 ~ 250°C). Also included is a new result for a standard B_2H_6-based *p*-layer deposited at 200°C for comparison with the TMB-based *p*-layer (sixth row).

Sample	$([B_2H_6]$ or $[B(CH_3)_3])/\{[SiH_4]+[CH_4]\}$	E_{Tauc} at 25°C (eV)	E_σ (eV)	$E_{Tauc} - E_\sigma$ (eV)	σ_{RT} ($\Omega^{-1}cm^{-1}$)
a-Si:H:B (as deposited)	0.001	1.73	0.34	1.39	1.6×10^{-4}
a-Si:H:B (H-treated)	0.001	1.91	0.39	1.52	3.0×10^{-5}
a-$Si_{1-x}C_x$:H:B (as deposited)	0.001	1.85	0.48	1.37	8.6×10^{-6}
a-$Si_{1-x}C_x$:H:B (as deposited)	0.005	1.75	0.43	1.32	4.0×10^{-5}
a-$Si_{1-x}C_x$:H:B (as deposited, 200°C)	0.002 (TMB)	1.88	0.55	1.33	7.0×10^{-5}
a-$Si_{1-x}C_x$:H:B (as deposited., 200°C)	0.001	1.87	0.50	1.37	3.2×10^{-6}

Table 8 Initial characteristics of the solar cells of Fig. 25.

CELL	TCO/*p-i* interfaces	J_{sc} (mA/cm^2)	V_{oc} (V)	FF	EFF.
A	standard	13.7	0.74	0.65	6.6%
B	H-treatment 9.2W	11.8	0.74	0.54	4.7%
C	H-treatment 28W	12.9	0.66	0.35	3.0%

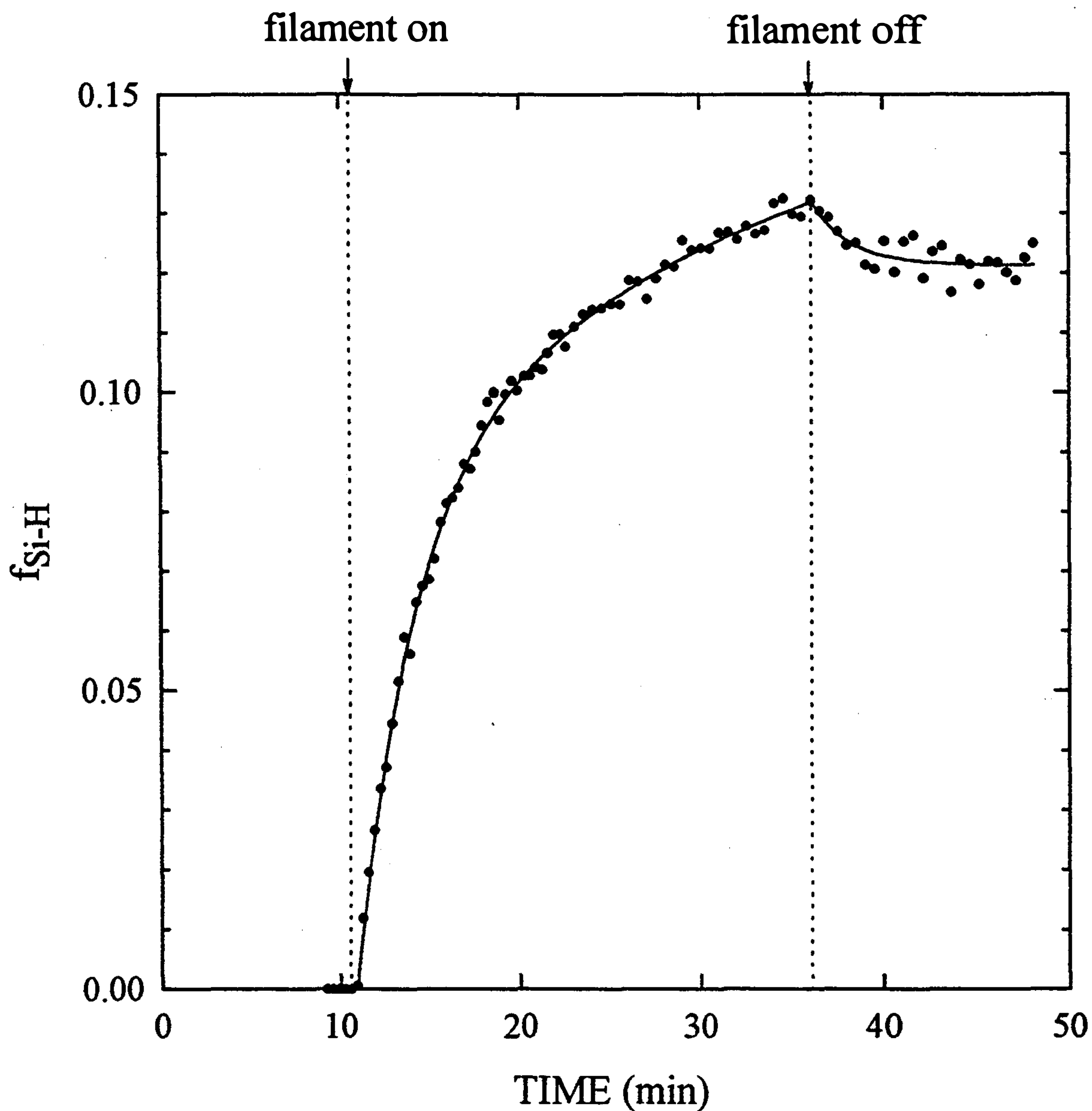

Fig. 24 Volume fraction of H-modified component (proportional to the density of broken Si-Si bonds) deduced in an analysis of RTSE data collected during *in situ* exposure of 300Å thick a-Si:H:B to atomic H at 250°C. The solid lines plotted for filament on and off are fits assuming models for reaction limited breaking of Si-Si bonds (filament on) and thermally activated re-formation of the bonds (filament off).

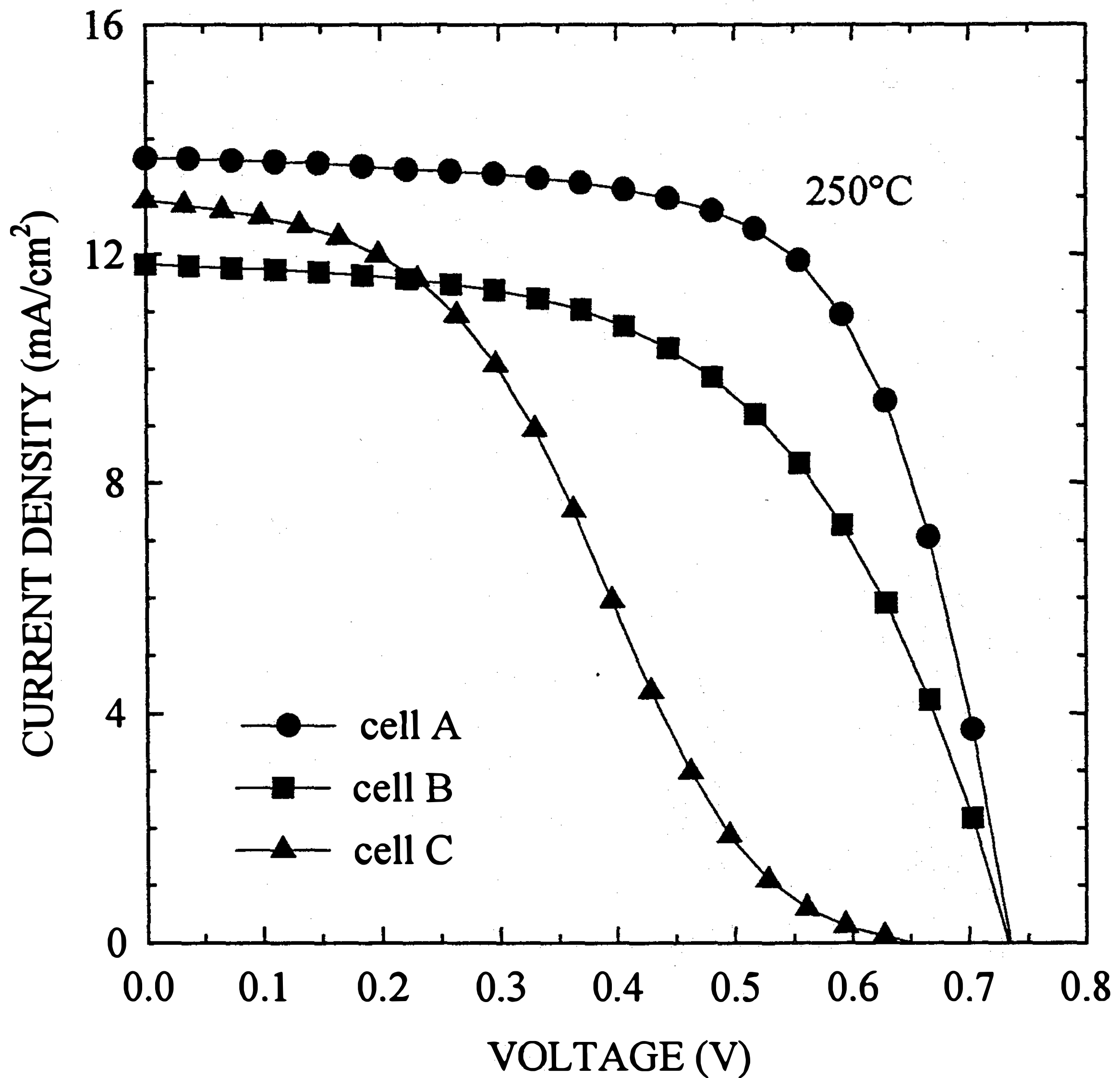

Fig. 25 Initial I-V characteristics of midgap a-Si:H cells prepared in a single-chamber system at 250°C. These characteristics reveal the cell degradation that results from simultaneous attempts to etch away surface contamination and generate a wider gap a-$Si_{1-x}C_x$:H *p*-layer using filament hydrogenation. Cells A, B, and C were prepared using filament powers of 0, 9.2, and 28W.

5. Top Cell Interfaces

5.1 Compositional Gradients

In our recent research, we have developed a new approach for the analysis of RTSE data that is of importance in monitoring solar cell grading. In our previous way of interpreting data, we kept track of the history of the deposition of one or more thin films. Thus, the multilayer optical analysis included a separate layer in the optical model for each film in the substrate structure, as well as for each change in the preparation parameters. For example, a glass/SnO_2/*p-i* structure would include the glass substrate, SnO_2, any SnO_2/*p* interface layer, the *p*-layer, any *p-i* interface layer, the *i*-layer, and finally, the *i*-layer surface roughness. This approach is possible, as long as care is take to prevent the accumulation of errors with the addition of the layers. The approach is not possible, however, for graded layers. For example, ten separate layers - each of slightly different optical properties - would be required to model a 200Å *p-i* buffer layer with 20Å resolution. Ultimately, however, even higher resolution would be desired to determine the precise band gap profile.

In order to solve this problem, we have adapted the "common-pseudosubstrate approximation" to RTSE. This novel approach allows us to obtain the evolution of the optical properties and surface roughness on the top ~ 15Å of the growing film without any knowledge of the underlying sample structure. Our first test of the approach was to form structures having graded void volume fractions. This was achieved by continuously ramping the H-dilution in an a-$Si_{1-x}C_x$:H film, keeping all other deposition parameters constant. As shown in Fig. 26 (top), we started with R = 2 and increased R linearly with time to the optimum value of R = 20, returned to R = 2, and then back to R = 20, all at the same ramping rate. In earlier work, we found that the H-dilution ratio strongly affected the void volume fraction in the a-$Si_{1-x}C_x$:H film, but there was little effect on the C and H contents. Because of this, the void volume fraction is expected to be primary variable parameter in characterizing the property gradients. The top part of Fig. 26 also includes the instantaneous deposition rate extracted from the RTSE data. The rate varies from about 1.3Å/s when R = 2 to 0.6Å/s when R = 20. By integrating the instantaneous deposition rate, the accumulated thickness can be determined versus time.

In the lower part of Fig. 26, the surface roughness layer thickness and the gradient in the void volume fraction are plotted continuously versus accumulated bulk layer thickness. The change in roughness is relatively small throughout the preparation process, however, the relative void fraction shows large gradients that track the variation in R. The results here are unique in that they represent the first successful optical analysis of amorphous semiconductor structures having continuously varying properties with thickness. Obviously, samples with continuously varying void fractions are not directly useful in solar cell applications. However, the procedures we have developed are readily adaptable to samples with continuously varying alloy composition. Further research on this topic is presented in Sec. 6.

5.2 TCO/*p-i* Interfaces

The properties of very thin (150-300Å) doped layers and interfaces have a profound impact on the performance of amorphous semiconductor solar cells. Because of this, the performance of solar cells cannot be predicted from a knowledge of the bulk properties of thick layers alone. For example, it is known that the properties of very thin microcrystalline layers are much different from thick layers due to an increase in the volume fraction of the crystalline component that occurs with thickness. In addition, interactions between TCO substrate layers and the hydrides in the plasma used to deposit the *p*-layer can modify the properties of the TCO, generating free metal at the interface in the case of the SnO_2/a-$Si_{1-x}C_x$:H structure. Finally, *p*-type dopant-related contaminants are often incorporated at the *p/i* interface. Effects such as these yield cell performances that depend sensitively on the details of the processing procedure. In order to extend our knowledge of the properties of very thin layers and interfaces, real time probes of solar cell fabrication are desired.

We here describe the results of RTSE studies of interface formation during single-chamber preparation of the *p-i* layers of a-Si:H solar cells in the superstrate configuration. With the full spectroscopic capability of RTSE, we can obtain information on the microstructural evolution of each layer, including the surface roughness and bulk layer thicknesses and bulk void volume fraction versus time. We can also obtain information on the optical properties of each layer, including the complex dielectric function (1.5 to 4.0eV) and the optical gap. All this information can be obtained from data collected during growth, not only for each individual layer of the solar cell, but also for unintentional interface layers. Figs. 27 and 28 summarize results of our initial studies of a standard cell, starting with the deposition of *p*-type a-$Si_{1-x}C_x$:H ($x \approx 0.1$) on doped SnO_2, followed by the deposition of intrinsic a-Si:H on the p-layer. In previous investigations, we established conditions of *p*-layer deposition that avoid metallic Sn contamination at the SnO_2/*p*-layer interface. Thus, the TCO/*p*-layer interface problem is not of concern in this particular study.

The top part of Fig. 27 shows part of a single wavelength ellipsometry trajectory (at 2.52eV), plotted in terms of the raw pseudo-dielectric function data, as an illustration of the *p-i* deposition process on the specular SnO_2 surface at 250°C. The schematic sample structures along with the associated thickness values, corresponding to the different trajectory segments, are depicted in the lower part of the figure, parts (a-f). As shown in Fig. 28(a-c), the first segment is swept out during the growth of a *p*-layer from a gas flow ratio of $[CH_4]:[SiH_4]:[H_2]:[B_2H_6]$ = 4:6:1:0.01, reaching a bulk thickness of 156Å. Because of the conformal coverage of the rough TCO surface, the measurements also identify a ~ 90Å interface roughness layer between the TCO and the *p*-type a-Si:H, and a ~ 70 Å surface roughness layer on the a-$Si_{1-x}C_x$:H. In the second segment, the *p*-type gas mixture is evacuated from the chamber which is then purged with Ar for 55min. In this time, a very thin layer [dark band in (d-f) of Fig. 28] develops on the surface (in the

absence of any plasma), conformally covering the surface. After purging, *i*-layer growth is initiated using a pure SiH_4 gas mixture.

Fig. 28(a-c) show more detailed quantitative data on the evolution of the layer thicknesses. Figure 28(a) shows that in the first ~50s of film growth, the *p*-layer is filling in the modulations of the rough TCO surface. After 50s, the substrate roughness is filled in by depositing material, and a well-defined bulk layer grows at a linear rate of 1.6Å/s. In the time it takes to grow the 156Å bulk *p*-layer, the substrate-induced roughness on the *p*-layer decreases in thickness from 85 to 66Å. Including the interface layers leads to an effective or mass thickness of the *p*-type a-$Si_{1-x}C_x$:H given by $d_{mass} = f_i d_i + d_b + 0.5d_s$ = 0.5(92)+156+0.5(66) Å = 235Å. Figure 28(b) shows the development of the interface layer during the 55min flushing time at an average rate of 0.46Å/min. Because the thickness of this layer is less than that of the substrate roughness layer onto which it deposits, a bulk layer does not form. The mass thickness of the layer after 55min is given by $d_{mass} = f_i d_i + 0.5d_s$ = 0.27(66)+0.5(15)Å = 25Å. This layer appears to form from the desorption of B-containing species from the reactor walls, followed by re-deposition on the *p*-layer surface. This layer is much thicker than that described in our previous discussion of the optimized midgap cell, owing to the unoptimized gas switching procedure at the end of the *p*-layer. (In particular, the *p*-layer gas was not turned off immediately upon terminating the plasma, leading to CVD growth of B-rich a-Si on the film surface Si-coated internal components of the reaction.) Fig. 28(c) shows the first 3min of *i*-layer growth. In the first 25s, the *i*-layer fills the roughness in the *p*-layer surface, and a bulk layer forms at later times, increasing in thickness at a rate of 1.3Å/s. In the first ~ 200Å of *i*-layer growth, the substrate-induced roughness on the *i*-layer relaxes from ~ 50 to 35Å.

The optical properties of the three separate layers are shown in Fig. 28(d-f). Results are given in the insets for the imaginary part of the dielectric function ε_2 over the range from 2.5 to 4.0eV. For materials of similar composition, the maximum ε_2 increases with decreasing void volume fraction up to a value of ~ 30 for the highest-quality a-Si:H. The main part of the figure shows the linear extrapolation of $(\varepsilon_2)^{1/2}$ used to obtain the optical gap. It should be noted that the gap values obtained here differ in two ways from those typically quoted in the literature. First, the values are characteristic of a sample growth temperature of 250°C, and second, they are obtained using the constant dipole matrix element technique as applied by Cody which provides better linearity of the plot over a wider energy range. To obtain the room temperature Tauc gap (constant momentum matrix element), ~ 0.20eV must be added to each of the gap values shown here.

The results of Fig. 28 are important in that they provide a fingerprint of the top junction of the solar cell. By adding an *n*-layer and back contact onto the *p/i* structures we are able to associate the top junction solar cell structure with the performance of the resulting cell. For the structure of Fig. 28 an initial efficiency of 5.2% has been obtained for cells on textured TCO-coated glass substrate. Thus, these values are characteristic of a cell having the optical fingerprint displayed in Fig. 28. Our recent studies have suggested

that the effect of the narrow gap material at the *p-i* interface, as shown in Fig. 28(e), is to reduce both J_{sc} and FF of the resulting solar cell. Thus, improvements can be made in this cell based on an understanding of the monolayer scale structure. Various approaches are being used to improve the cell characteristics: (i) improved *p*-layer gas switching procedure as noted above; (ii) standard a-$Si_{1-x}C_x$:H:B *p*-layer followed by H plasma exposure of surface to remove contaminants; (iii) standard a-Si:H:B *p*-layer deposition followed by hot-filament H clean and *p*-layer modification as described in the previous section; and (iv) a-$Si_{1-x}C_x$:H:B *p*-layer prepared using a TMB source gas instead of diborane for *p*-type doping. As noted earlier, we have currently installed the TMB in both multi-chamber and single-chamber reactor systems at Penn State. As shown in the previous section, there may be some advantages to using a C-free dopant gas, namely, the ease with which the resulting *p*-type material can be modified or crystallized by H-atom exposure. Thus, we have the capability of using either TMB and diborane in our future studies. Returning to our discussion of the process improvement, we have found that by combining the approaches (i) and (iv) above and reducing the substrate temperature to 200°C, the initial efficiency of midgap cells prepared in our single-chamber system have been increased from 5.2 to 8.4%. By using atomic-H interface passivation treatments, the initial efficiency of our multi-chamber midgap cells has been increased from a best value of 8.1% to 8.6%.

5.3 *p/i* Interfaces

We have added a *p*-type doping capability with TMB gas to our single-chamber solar cell deposition system. As a result, we can now compare the *p/i*-interface structure of solar cells incorporating *p*-layers doped using diborane and TMB gas sources. Some initial insights have been obtained from a comparison of single photon energy trajectories, focusing on (i) the termination of the *p*-layer plasma, (ii) the 50min Ar gas flush, and (iii) the initial stage of *i*-layer deposition. Simple inspection of these raw data can provide a relative magnitude of the *p/i*-interface contamination that occurs during this period, but exact quantitative results must await a detailed analysis of the full *p*-layer of the solar cell. Although this has been done in the case of several cells deposited at 200 and 250°C using a diborane source, it has not been done for any of the cells deposited using the TMB source. Figs. 29(a)-(c) show the *p/i* interface trajectories for three *p/i* interfaces. The results in (a) are for the optimized midgap cell of Figs. 18 to 20, in which the *p*-layer is a-$Si_{1-x}C_x$:H:B formed from diborane and the *i*-layer is a-Si:H. The results in (b) and (c) are for an a-Si:H midgap and an a-$Si_{1-x}C_x$:H widegap cell (R = 10), in which the *p*-layer is prepared with TMB as described in the previous part.

It turns out that the magnitude of the discontinuity in Δ between the end of the *p*-layer and the start of the *i*-layer trajectories in Fig. 29 is a measure of the total effective thickness of interface contamination. As can be seen from Fig. 20 and Table 2, this value is 1.7Å in the case of the optimized diborane-prepared midgap cell of Fig. 29(a). Values of 1.4Å and 0.7Å are estimated in the case of the TMB-prepared midgap and widegap cells of Fig. 29(b) and (c) respectively. It appears that in the case of TMB, the submonolayer-

level contaminant is volatile and some of it appears to blow off the surface upon *i*-layer formation, particularly when the *i*-layer is formed with extensive H-dilution as in the case of Fig. 29(c) with R = 10. We conclude at this point that TMB does appear to be favorable for achieving a higher quality *p/i* interface, however, it is clear that even with TMB the interfaces are not perfect and there remains some run-to-run irreproducibility.

We have described the solar cell performance for a series of widegap cells discussed in the previous part. Fig. 30 shows the estimated effective thickness of the interface layer plotted versus the value of R used in the preparation of the *i*-layer. In considering a possible correlation, one notes that the cell parameters show different variations with R. For example, in the case of specular SnO_2:F, V_{oc} reaches its maximum value near R = 5 whereas J_{sc} and the fill-factor reach their maxima near R = 10. For ZnO, however, V_{oc} is optimal for R = 20 whereas J_{sc} and the fill-factor are again maximum near R = 10. It appears that V_{oc} exhibits different behavior than J_{sc} and the fill-factor, while the latter two parameters show a strong correlation. Thus, it is clear that V_{oc} is not controlled by the interface layer thickness, however, there appears to be an effect of the interface layer on the current and/or fill-factor.

One needs to be cautious in drawing the latter conclusion without a more carefully controlled study in which only the interface layer thickness is varied. At this point however we are optimistic that we have uncovered a key parameter in the interface thickness. For example, it may be argued that the trends in J_{sc} and fill-factor are related to material quality and TCO/*p* interface issues. First the improvement in these parameters for $0 \leq R \leq 10$ may be due to the improvement in a-$Si_{1-x}C_x$:H *i*-layer quality with R. One might then propose that the degradation in these parameters with increasing R from 10 to 20 may be due to a degradation of the TCO/*p* interface by H penetration through the *p*-layer to the TCO where it may generate free metal. However, one can further argue against this effect since it is expected to be absent with ZnO TCO, yet the current and fill-factor still drop from R = 10 to 20 for ZnO. We should keep in mind that the diffusive H-atom reduction of the specular SnO_2:F may, however, account for the decreasing V_{oc} with increasing R above R = 5. This effect occurs to a lesser extent in textured SnO_2:F, which because of its larger grained structure is less susceptible to reduction. (Earlier work has shown that the grain boundary regions of the SnO_2:F are preferentially attacked and reduced to free metal by atomic H.) The solar cells on ZnO, which is not reduced at all to free metal by atomic H, exhibit an increase in V_{oc} out to R = 20, providing further support for a TCO reduction effect. Such features would occur upon striking the *i*-layer plasma, but may also be masked by other features associated with the weak H-chemical annealing of the a-$Si_{1-x}C_x$:H *p*-layer that may occur upon exposure to the H-rich plasma. In summary then, we tentatively conclude that the fill-factor and current of the widegap cells may in fact be influenced by the interface layer, whereas there is not a clear effect on V_{oc} which appears to be influenced at least in part by the nature of the contact to the TCO.

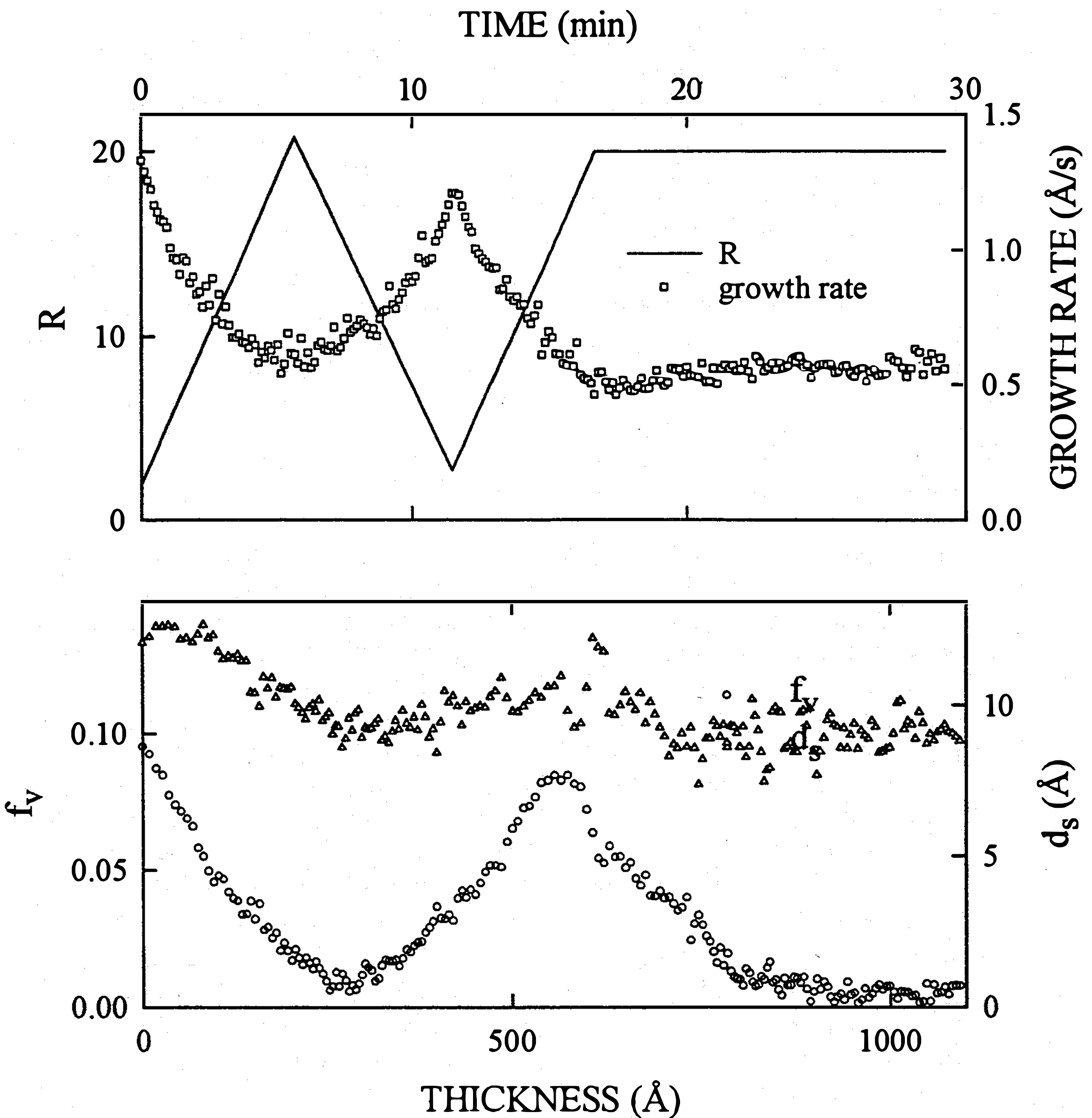

Fig. 26 Results of an RTSE analysis of an a-$Si_{1-x}C_x$:H structure having a graded void volume fraction prepared by ramping the H-dilution ratio R, between 2 and 20 (solid line at the top). Also shown at the top is the instantaneous deposition rate. At the bottom the surface roughness thickness versus accumulated film thickness is shown, along with the gradients in the void volume fraction. It is clear that the microstructure of the film tracks the variation in the gas flow conditions.

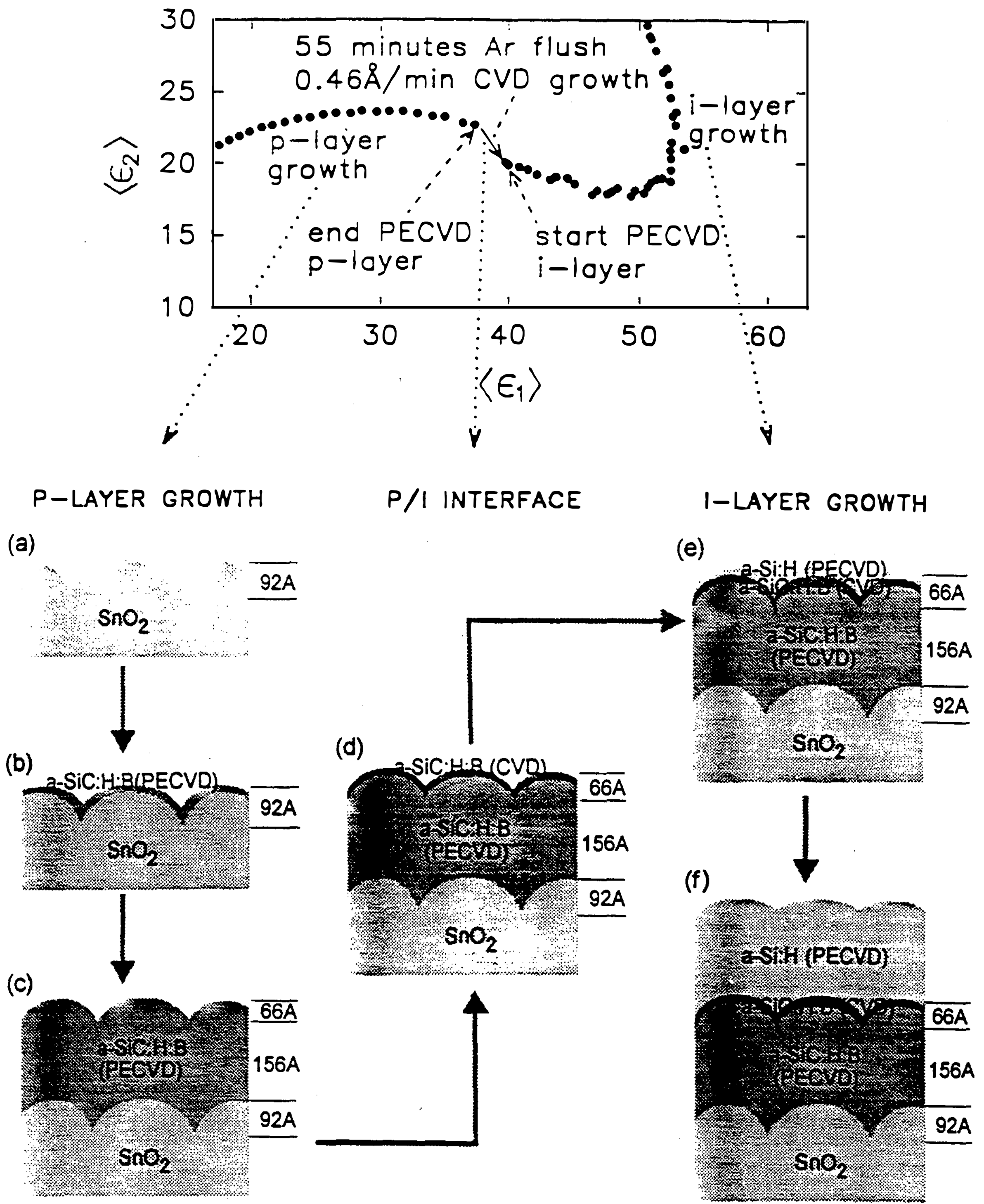

Fig. 27 Single wavelength ellipsometry trajectory (2.52eV) centered near the formation of the *p/i* interface for the sequential growth of a-$Si_{1-x}C_x$:H:B *p*- and a-Si:H *i*-layers on a doped SnO_2 surface. A thin layer forms at the *p/i* interface during purging the chamber with Ar. (a-f) Schematic diagrams of the sample structure at different stages in the growth. The *p*-layer gas shutdown procedure was not optimized for this deposition.

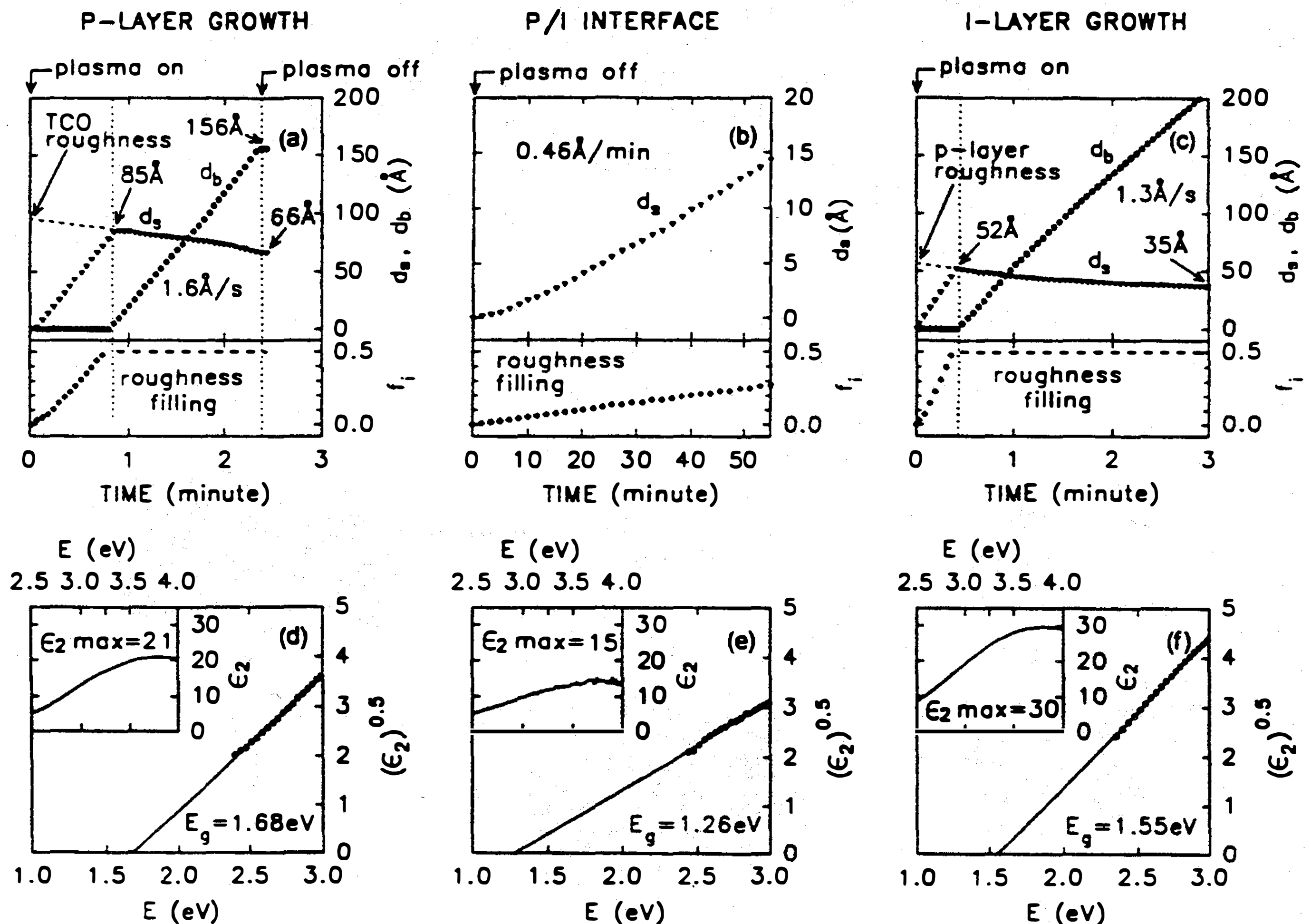

Fig. 28 Thickness and volume fractions versus time and 250°C optical data for the *p*-layer, the *p/i* interface layer, and the *i*-layer of the structure of Fig. 27. d_b is the bulk layer thickness and d_s is the surface roughness layer thickness. f_i is the volume fraction of the film that forms within the roughness on the surface of the substrate layer. The substrate roughness is completely filled in when f_i reaches ~ 0.5. The optical gap is determined by an extrapolation of the linear trend in $(\varepsilon_2)^{1/2}$ to zero ordinate, where ε_2 is the imaginary part of the dielectric function (shown in the inset from 2.5 to 4.0eV). The *p*-layer gas shutdown procedure was not optimized for this deposition, and this accounts for the thick *p/i* interface layer development.

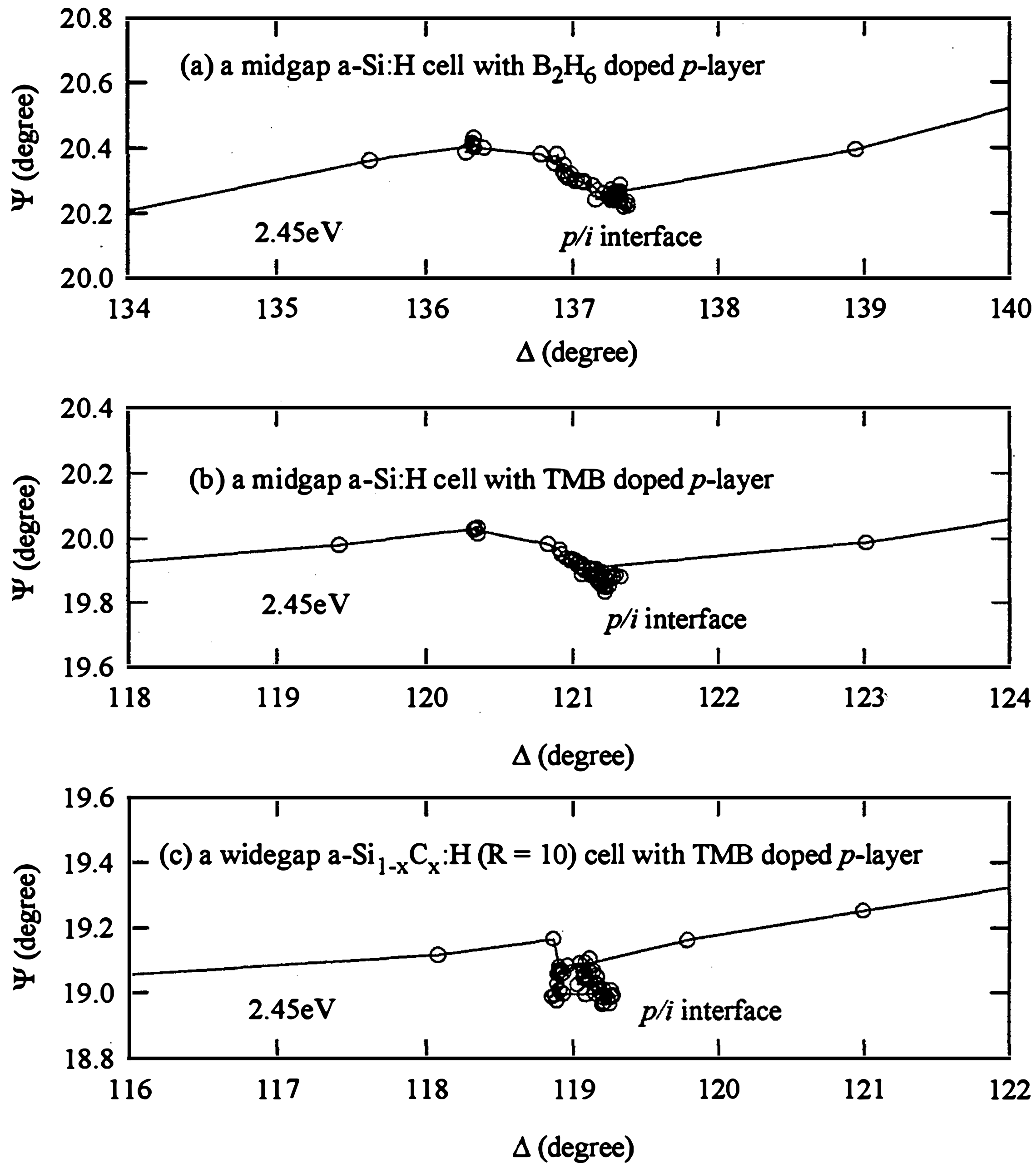

Fig. 29 Trajectories in the ellipsometric angles (Ψ,Δ), focusing on the *p/i* interface formation process for three *p-i-n* solar cells all using an optimium *p*-layer gas shutdown procedure: (a) a midgap a-Si:H cell that incorporates a *p*-layer prepared using diborane as the doping gas source; (b) a midgap a-Si:H cell prepared similarly to that of (a) but with a *p*-layer prepared using TMB as the doping gas source; and (c) a widegap cell incorporating a *p*-layer prepared with TMB similarly to that in (b) and an a-$Si_{1-x}C_x$:H *i*-layer prepared with R = 10. The trajectories show: (i) the end of the *p*-layer preparation, (ii) the 50min Ar purge initiated after the termination of the *p*-layer plasma and gas supply, and (iii) the initial stage of *i*-layer growth.

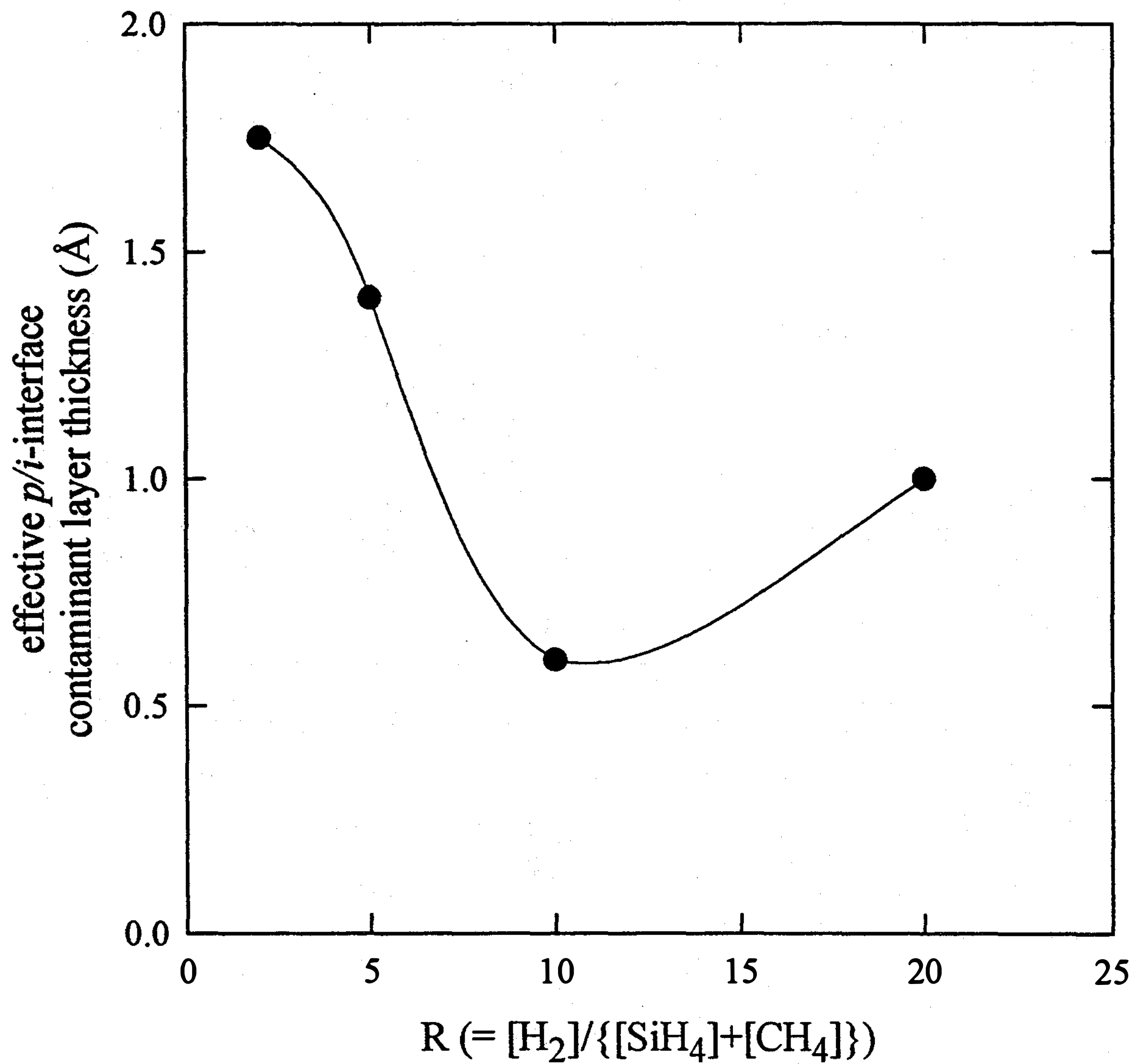

Fig. 30 Estimated effective *p/i* interface contaminant layer thickness formed during the Ar flushing procedure for a series of a-$Si_{1-x}C_x$:H widegap cells. The thicknesses are plotted as a function of the H-dilution ratio used in the preparation of the a-$Si_{1-x}C_x$:H *i*-layer.

6. Solar Cell Grading

6.1 Hydrogen Dilution Grading

Hydrogen-dilution grading has been employed in an attempt to improve the performance of our optimum widegap solar cells (4% efficiency) prepared on specular SnO_2:F by increasing V_{OC}. We have suggested that the decrease in V_{OC} for cells on SnO_2:F, observed when R is increased from 5 to 20 results from H penetration through the *p*-layer to the TCO. As a result, we have incorporated a H-dilution ramp from R = 2 to 20 in the first ~ 200 Å of the a-$Si_{1-x}C_x$:H i-layer growth. Otherwise the deposition conditions are the same as for the R = 20 cell described above (see Table 3). Table 9 compares the parameters for the control cell and those for the cell prepared with the H-dilution gradient. We have chosen to focus on the specular SnO_2:F TCO substrate since in that case the largest improvement is possible if the reduction effect can be eliminated. Results for the ZnO TCO substrate are also provided. The results are very interesting in that there is no change at all in V_{OC} or J_{SC} for the SnO_2:F TCO and only a slight increase in fill factor. This observation suggests three different possibilities. (i) TCO reduction by in-diffusing H is not the cause of the V_{OC} degradation with increasing R. (ii) An improvement in V_{OC} and other performance parameters that might be expected is reversed due to the presence of a defective layer formed at low R near the interface. (iii) Even with the low H-dilution buffer, H is still reaching and degrading the TCO interface.

One of these possibilities, (ii) can be eliminated by inspection of the results for the ZnO TCO substrate in Table 9. In this case, there is also very little change in the cell performance, suggesting that the high void fraction layer near the p/i interface, generated by the low R deposition is not detrimental to the device. To distinguish possibilities (i) and (iii), more experiments are needed with a thicker protective H-buffer. To accompany such experiments, we need the capability of characterizing these H-diluted layers which are expected to exhibit gradients in the void volume fraction. The RTSE data analysis techniques for doing this have been described in detail in Sec. 5.1 and in earlier reports. Here we simply present the results in Figs. 31 and 32. In Fig. 31, the H-dilution ramp, the relative void volume fraction in the top ~ 15Å of the film, and the instantaneous deposition rate are plotted as a function of time for the structure co-deposited with the cells of Table 9. In Fig. 32, the actual depth profile of the void volume fraction is shown. These results are calculated from the data in Fig. 31 by integrating the instantaneous deposition rate. The capability demonstrated in Fig. 32 is very important as we compare the effects of other protective H-buffers designed to distinguish between the possibilities (i) and (iii) provided above.

6.2 Widegap a-$Si_{1-x}C_x$:H Buffer Layers

We have initiated studies of wider gap undoped buffer layers incorporated at the *p/i* interface. Along with these studies, we are also developing the capability of characterizing the optical gap profile versus thickness for graded buffer layers using RTSE. The first

steps in this development have been described briefly in previous reports. Some of the key groundwork, including new data are presented here.

In order to use RTSE to characterize the graded alloy profiles in a-$Si_{1-x}C_x$:H, we need to establish the relationship between the optical properties (or dielectric function) at each photon energy and the value of x. In Fig. 33, we show the dielectric function of i-layers prepared with different values of the [CH_4]:[SiH_4] ratio Z, leading to different values of alloy composition x. These samples were prepared with a fixed value of R = 5, a source gas partial pressure of 0.07Torr, and a total pressure of 0.21Torr. In Fig. 33, the pairs of (Z, x) values are included along side each curve, where the value of x is determined by electron microprobe techniques. To avoid having to prepare a very large number of samples as a function of Z or x, we need to be able to parameterize a more limited data set so that reference dielectric functions can be generated as a continuous function of x. This provides an optical spectrum for comparison purposes so that x can be extracted from the near-surface dielectric function, measured during buffer layer preparation. Furthermore, the ability of the measured dielectric function to closely fit a member of the reference dielectric function set throughout the spectral range provides a criterion from which we can determine the deposition rate and thickness. In Fig. 34, we show the dependence of the dielectric function values on x for several photon energies that serves as an interpolation scheme for generating dielectric functions continuously versus x.

Table 10 shows our first performance results for a cell that incorporates a widegap buffer layer. In this cell, the flows of CH_4 and SiH_4 were varied roughly linearly starting with a flow ratio of [CH_4]:[SiH_4] = 3:2 and decreasing to 2:3 over a time of 330s, for an intended buffer layer thickness of 200Å (see Fig. 35). The control cell, which was prepared under identical conditions without the buffer layer, is the widegap cell with R = 5 in Table 3. For all TCO substrates, an increase of 0.03 ~ 0.04V in V_{oc} is observed. A small drop in fill-factor occurred for the SnO_2:F TCO substrates, while an increase occurred for ZnO substrates. Overall, the cell performance either remained about the same (SnO_2:F) or showed a significant (~ 20%) improvement (ZnO). In current research, we are characterizing the carbon concentration profile and optical gap profile of the buffer layer for the cell in Table 4. Once this information is obtained, modeling will be undertaken to obtain insights into the physical reasons for the cell parameter variations. In future research, we will attempt to optimize the buffer-layered cells using different gap profiles and insights from modeling. We will also compare the stability of the cells with and without buffer layers.

Table 9 Initial performance parameters for two widegap *p-i-n* solar cells incorporating 2000Å a-$Si_{1-x}C_x$:H *i*-layers. For the first, a H-dilution ramp from R = 2 to 20 is used in the early stages of *i*-layer growth. The remainder of *i*-layer growth is performed with R = 20. The second is a control cell prepared with R = 20 throughout the full *i*-layer. Results for solar cells on both specular SnO_2:F and ZnO are provided.

preparation	substrate	V_{OC} (V)	J_{SC} (mA/cm^2)	FF	EFF.
a-SiC:H i-layer	specular SnO_2:F	0.88	5.8	0.58	3.0
R = 2 to 20	specular ZnO	0.89	7.0	0.55	3.4

preparation	substrate	V_{OC} (V)	J_{SC} (mA/cm^2)	FF	EFF.
a-SiC:H i-layer	specular SnO_2:F	0.88	5.8	0.56	2.9
R = 20	specular ZnO	0.90	6.9	0.56	3.5

Table 10 Initial performance parameters for two widegap solar cells incorporating 2000Å a-$Si_{1-x}C_x$:H *i*-layers. For the first, a wider-gap buffer layer with an intended thickness of 200Å was incorporated in the early stages of *i*-layer growth. The buffer layer was generated by ramping the [CH_4]/[SiH_4] ratio Z from 3/2 to 2/3. The remainder of *i*-layer growth was performed with Z = 2/3. The H-dilution ratio R = [H_2]/{[SiH_4]+[CH_4]} was maintained at 5 throughout the *i*-layer deposition. The second is a control cell prepared with a [CH_4]/[SiH_4] ratio of 2/3 and R = 5 throughout the full *i*-layer. Results for solar cells on specular SnO_2:F, textured SnO_2:F, and ZnO are provided.

preparation	substrate	V_{OC} (V)	J_{SC} (mA/cm^2)	FF	EFF.
a-SiC:H i-layer	specular SnO_2:F	0.96	5.7	0.60	3.2
200Å buffer	textured SnO_2:F	0.92	6.6	0.50	3.1
Z = 1.5 to 0.67	specular ZnO	0.92	7.4	0.56	3.8

preparation	substrate	V_{OC} (V)	J_{SC} (mA/cm^2)	FF	EFF.
a-SiC:H i-layer	specular SnO_2:F	0.93	5.6	0.62	3.2
control cell	textured SnO_2:F	0.88	6.3	0.52	2.9
Z = 0.67, R = 5	specular ZnO	0.89	6.7	0.52	3.1

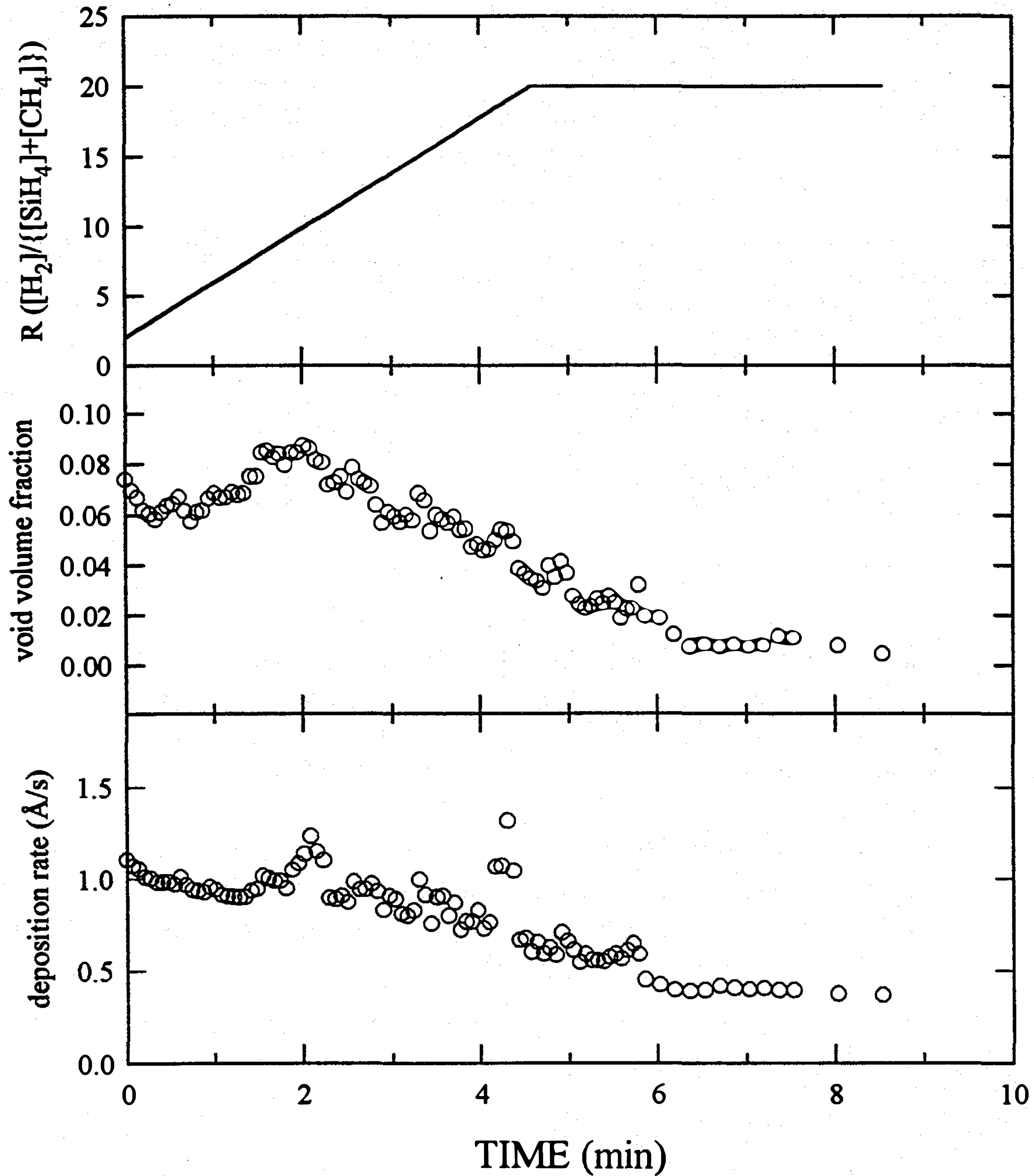

Fig. 31 Near-surface (top ~ 15Å) void volume fraction (center panel) and depositon rate (lower panel) versus time as measured by RTSE during a H-dilution (top panel) ramp in the initial stages of the growth of an a-$Si_{1-x}C_x$:H *i*-layer. R is increased linearly with time from 2 to 20 in an attempt to avoid H-diffusion through the *p*-layer and consequent damage of the SnO_2:F TCO.

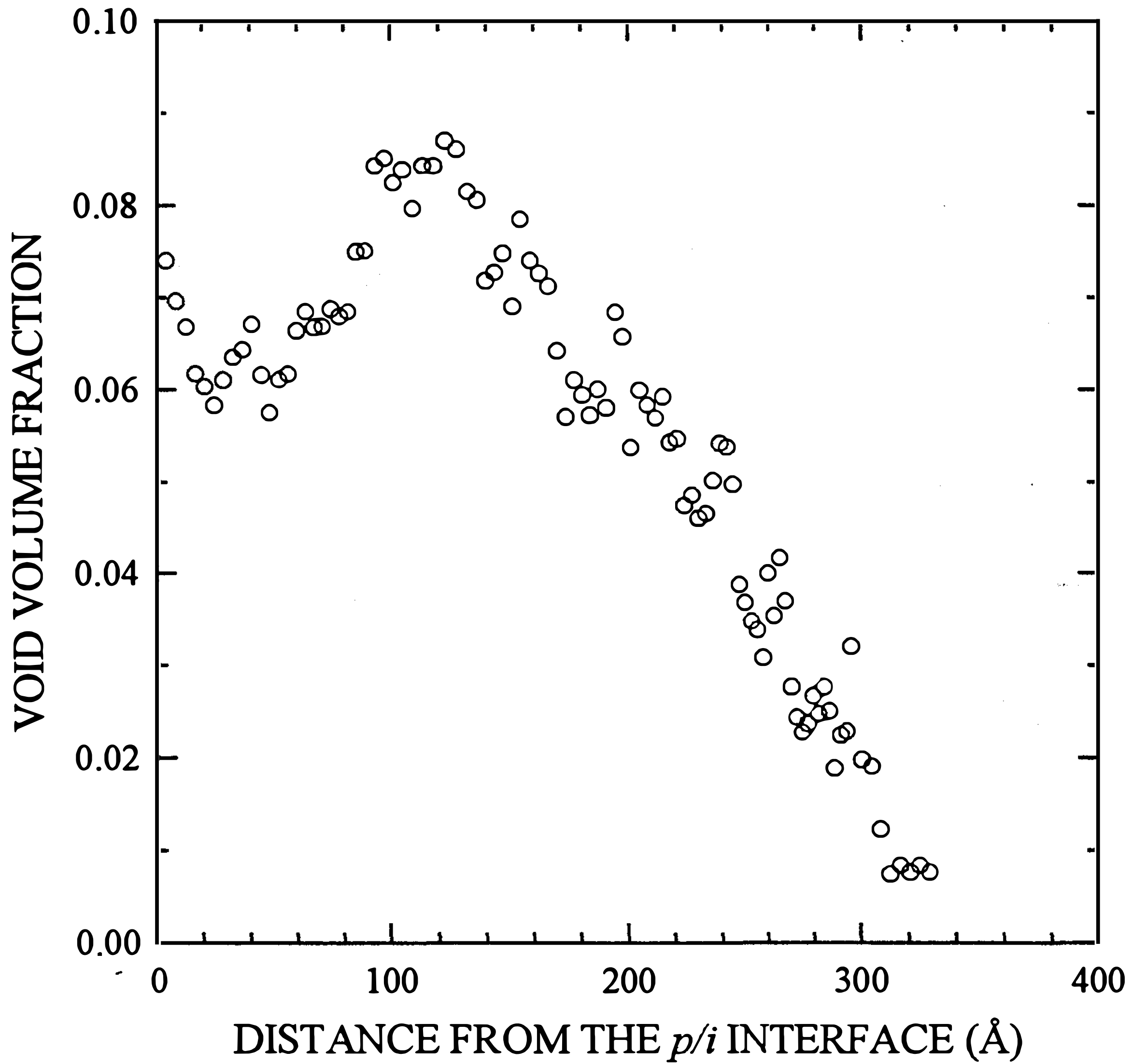

Fig. 32 Depth profile in the relative void volume fraction versus distance from the *p/i* interface as measured by RTSE during a H-dilution ramp in the initial stages of an a-$Si_{1-x}C_x$:H *i*-layer (top panel of Fig. 31). These results were deduced from the data of Fig. 31 (center panel), converting time to thickness by integrating the instantaneous deposition rate.

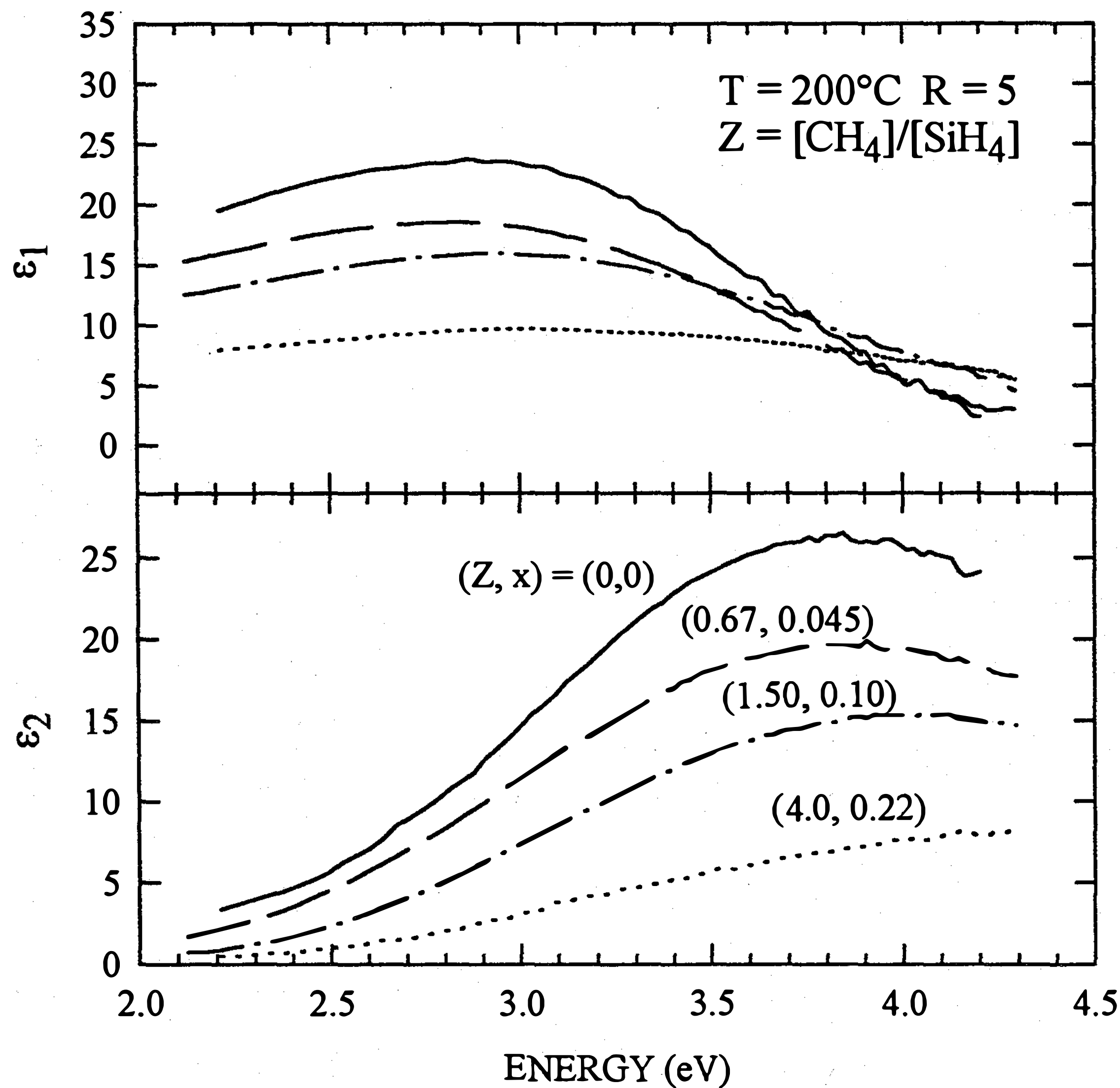

Fig. 33 Real (top) and imaginary (bottom) parts of the dielectric functions of a-$Si_{1-x}C_x$:H *i*-layers, prepared as a function of the $[CH_4]/[SiH_4]$ flow ratio, designated Z. Each spectrum is identified by a pair of values (Z,x), the flow ratio and the alloy composition. Here x has been obtained by electron microprobe measurements. The dielectric functions are characteristic of the measurement temperature of 200°C, having been determined from RTSE during growth.

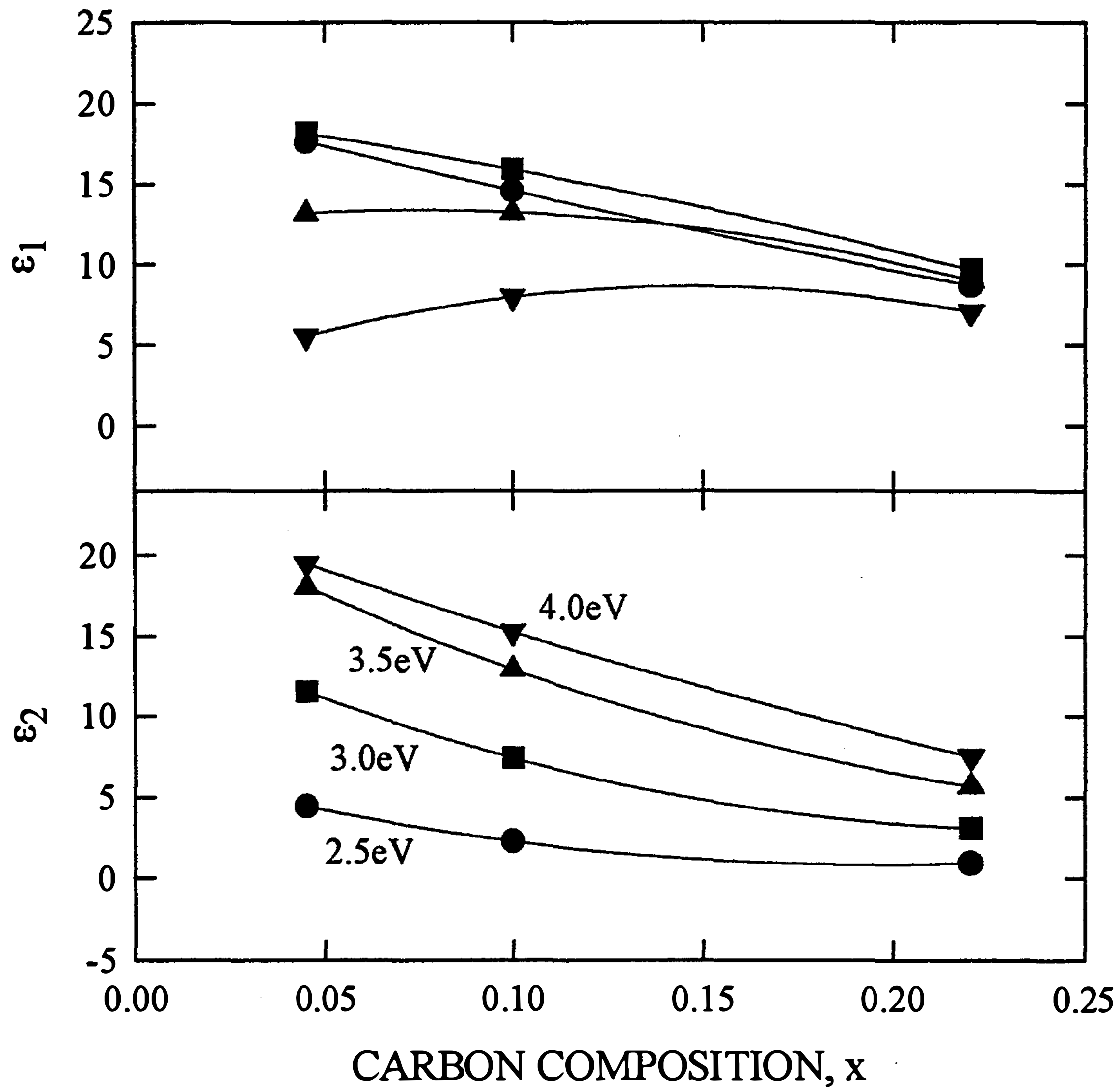

Fig. 34 Dependence of the real and imaginary parts of the dielectric functions at selected energies for a-$Si_{1-x}C_x$:H *i*-layers as a function of the alloy composition x. Such results are used in an interpolation scheme to determine the dielectric function of a-$Si_{1-x}C_x$:H for any value of x. The dielectric function values are characteristic of the measurement temperature of 200°C, having been determined from RTSE during growth.

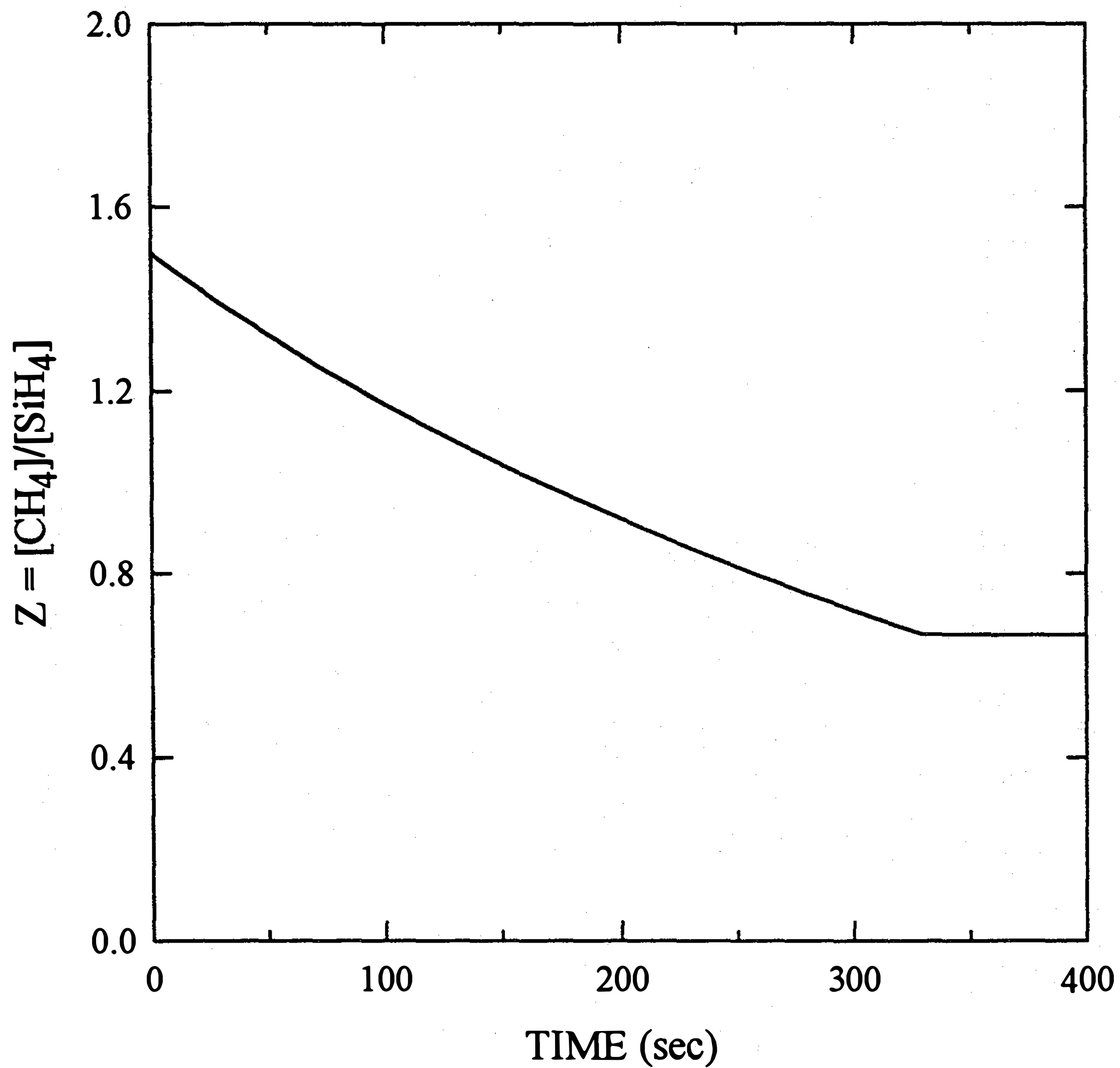

Fig. 35 The ramp in the $[CH_4]/[SiH_4]$ ratio, Z, as a function of time used to generate a widegap buffer layer in the initial stages of growth of an a-$Si_{1-x}C_x$:H *i*-layer.

7. Future Work

In order to reach the goals set in our proposal, as well as goals set by the Wide Gap Team, we must continue our efforts along the lines initiated here. The numbers in this list correspond to the topics highlighted in the Executive Summary at the beginning of this report. The future investigations will be continued under Phase II and Phase III of this subcontract where work enumerated in this section is confined to the topics addressed in Phase II.

1. **Improved Understanding of Stability in Materials and Solar Cells**

   We will continue to fabricate materials and solar cell structures for other Wide Bandgap Alloy Team members and industry and chart progress made in the stabilized efficiency of widegap solar cells. Where possible, numerical modeling and/or device fabrication will be used to test concepts of other team members. Efforts will be made to maintain close contact with the Metastability and Mid-Bandgap Alloy Teams and in the characterization of their materials. We will continue to collaborate with the industrial partners of the Wide-Bandgap Team by assisting with optical measurements of materials and structures. Our initial work has established baseline optical properties, namely $\alpha(h\nu)$ for $0.8 \leq h\nu \leq 5$eV in the annealed and light-soaked states, for widegap alloys prepared by Solarex. We have also characterized the structure of ZnO/Ag interfaces for USSC. In the future, we intend to study pure Si-based widegap materials and *p*-type microcrystalline materials at the request of ECD.

2. **Novel Intrinsic Material Optimization**

   We will complete assessment of selected novel materials using the same approach as used in Phase I for conventional PECVD materials. Films will be supplied to other team members for specialized measurements, and all measurements will be catalogued for comparison with standard materials. Our initial efforts in studying intrinsic a-$Si_{1-x}C_x$:H were undertaken in order to ensure that the properties of the alloys that we use in our structures are similar to those of device quality alloys of similar optical gaps prepared by industry. Our materials compare favorably to industry films of similar optical gaps. The state of the art however is progressing. In future work we intend to further optimize our intrinsic materials with higher gaps using H-dilution and lower substrate temperatures. We will use both temperature and gas pressure as variables in an attempt to optimize the layers as characterized by sub-bandgap absorption spectra, void density, and dark conductivity versus temperature. In these further attempts, we will continue to correlate electronic characteristics with microstructural evolution.

3. **Solar Cells Optimized for *p*- and *i*-Layer Performance**

   Optimization of amorphous and microcrystalline *p*- and amorphous *i*-layers together in a solar cell configuration will be completed, achieving the optimum *p/i* configuration within the parameter space of conventional PECVD amorphous and microcrystalline

films. The ability of numerical modeling to predict the performance of these optimized cells based on materials data inputs will be tested. Solar cell stability using material parameters will be modeled and consistency sought in the results. The cell design of both *p-i-n* and *n-i-p* structures will be modified as needed to improve the stability performance using insights provided by the modeling.

4. Novel *p*-Type Materials Optimization

The *p*-layer performance for novel wider-bandgap *p*-layer materials will be charted for amorphous silicon, silicon-carbon, as well as microcrystalline silicon. For those materials that show further promise for solar cells we will study materials growth on transparent conducting oxides (TCO), including ZnO, to ensure that the TCO degradation does not eliminate promising material candidates. We will deposit *p-i-n* and *n-i-p* solar cells using *p*-layers designed as an improvement over previously optimized amorphous materials. In situ ellipsometry studies of *p*-type μc-Si:H will be initiated in an attempt to better understand the material, its properties, and its suitability for devices. We will alter the μc-Si:H growth environment by varying the gas flow ratios while maintaining the H-dilution ratio constant. Optical absorption spectra of the μc-Si:H thin films will be obtained and compared to the results for a-$Si_{1-x}C_x$:H, to assess potential advantages of the former in solar cells. In addition, such materials will be doped in attempts to place the Fermi level closer to the conduction band edge than has been possible in the amorphous alloys.

5. Top Cell Interfaces

Studies of the correlation between interface stability and solar cell stability will be completed for optimum solar cells fabricated with conventional PECVD amorphous and microcrystalline *p*- and amorphous *i*-layers. Focus will be given to developing an optimum solar cell, on which interface corrective procedures will be instituted to further improve solar cell efficiencies.

6. Solar Cell Grading

Solar cells will be fabricated with graded *i*-layers using optimum amorphous and microcrystalline *p*-layers in the devices as guided by real time monitoring, modeling, and sensitivity analysis. The *i*-layers will be prepared under optimized conditions and comprehensive measurement of the stabilized performance in order to ensure that directions provided by the modeling are accurate. Further work needs to be accomplished in order to fully implement our grading capability. We need to develop the optical equations that allow us to convert the change in near-surface dielectric response, as measured by single-photon energy ellipsometry, to a near-surface band-gap. These equations must take into account the 10 ~ 20Å roughness layer that typically exists on the growing semiconductor surface. Once these equations are fully developed, we plan to install them in a real time monitoring and control loop, so that the calculated band gap is compared to a target value and the CH_4, H_2, and SiH_4 flow

meters are adjusted under computer control to meet the target value. Initially this well be set up on a single-chamber system for feasibility analysis, using a 486 microprocessor-based computer for speed. This will allow us to compare predicted and actual performances of cells with the pre-specified gradations, which can then be modeled in a quantitative, self-consistent manner.

8. Bibliography

1. I. An, Y. Lu, C. R. Wronski, and R. W. Collins, "Real time spectroellipsometry study of the interaction of hydrogen with ZnO during ZnO/a-$Si_{1-x}C_x$:H interface formation", *Appl. Phys. Lett.* **64**, 3317 (1994).

2. H. V. Nguyen, I. An, R. W. Collins, Y. Lu, M. Wakagi, and C. R. Wronski, "Preparation of ultrathin microcrystalline silicon layers by atomic hydrogen etching of amorphous silicon and end-point detection by real time spectroellipsometry", *Appl. Phys. Lett.* **65**, 3335 (1994).

3. M. Gunes, C. R. Wronski, and T. J. McMahon, "Charged defect states in intrinsic hydrogenated amorphous silicon films", *J. Appl. Phys.* **76**, 2260 (1994).

4. R. M. Dawson, C. M. Fortmann, M. Gunes, Y. M. Li, S. Nag, and C. R. Wronski, "The Staebler-Wronski effect and thermal equilibrium of defect and carrier concentrations", *Mat. Res. Soc. Symp. Proc.* **336**, 251 (1994).

5. M. Gunes, R. W. Collins, and C. R. Wronski, "Charged defect state distributions obtained from the analysis of photoconductivities in intrinsic a-Si:H films", *Mat. Res. Soc. Symp. Proc.* **336**, 413 (1994).

6. Y. Lu, S. Kim, M. Gunes, Y. Lee, C. R. Wronski, and R. W. Collins, "Process-property relationships for a-$Si_{1-x}C_x$:H deposition: excursions in parameter space guided by real time spectroellipsometry", *Mat. Res. Soc. Symp. Proc.* **336**, 595 (1994).

7 Y. Lu, S. Kim, I. Chen, Y. Lee, C. M. Fortmann, C. R. Wronski, and R. W. Collins, "Real time characterization of the preparation of a-Si:H based solar cells", *Conf. Rec. of the 24th IEEE PVSC* (IEEE, Piscataway, NJ, 1994), p. 421.

8. I. Chen, T. Jamali-beh, Y. Lee, C. Li, and C. R. Wronski, "Mobility and optical gaps in different a-Si:H based materials and their impact on cell performance", *Conf. Rec. of the 24th IEEE PVSC* (IEEE, Piscataway, NJ, 1994), p. 468.

9. M. Gunes, H. Liu, C. M. Fortmann, S. J. Fonash, and C. R. Wronski, "Direct correlations of bulk charged and neutral defect densities of states in a-Si:H films with characteristics of Schottky barrier solar cell structures", *Conf. Rec. of the 24th IEEE PVSC* (IEEE, Piscataway, NJ, 1994), p. 512.

10. R. W. Collins, I. An, H. V. Nguyen, Y. Li, and Y. Lu, "Real time spectroscopic ellipsometry studies of the nucleation, growth, and optical functions of thin films; part I: Tetrahedrally-bonded materials", in *Physics of Thin Films* **19**, edited by K. Vedam (Academic, New York, 1994), p. 49.

11. C. R. Wronski, I. Chen, M. Gunes, T. Jamali-beh, H. Liu, and R. W. Collins, "Quantitative correlation between a-Si:H material and solar cell properties: importance of charged defects", *8th Sunshine Workshop Tech. Digest* (MITI, Tokyo, Japan, 1995), p. 35.

12. R. W. Collins, Y. Lu, S. Kim, I. Chen, Y. Lee, and C. R. Wronski, "Real time monitoring of a-Si:H solar cells: evolution of microstructure and optical properties", *8th Sunshine Workshop Tech. Digest* (MITI, Tokyo, Japan, 1995), p. 53.

13. R. W. Collins, H. V. Nguyen, I. An, Y. Lu, M. Wakagi, "Preparation and optical properties of ultrathin silicon films", *Mat. Res. Soc. Symp. Proc.* **358**, 763 (1995).

14. H. V. Nguyen, Y. Lu, S. Kim, M. Wakagi, and R. W. Collins, "Optical properties of ultrathin crystalline and amorphous silicon films", *Phys. Rev. Lett.* **74**, 3880 (1995).

15. I. Chen and C. R. Wronski, "Internal photoemission on a-Si:H Schottky barriers revisited", *J. Non-Crys. Solids* **190**, 58 (1995).

16. Y. Lu, S. Kim, I. Chen, Y. Lee, C. M. Fortmann, C. R. Wronski, and R. W. Collins, "Real time monitoring of amorphous silicon solar cell fabrication", *Mat. Res. Soc. Symp. Proc.*, in press (1995).

17. T. Jamali-beh, I. Chen, H. Liu, Y. Lee, C. M. Fortmann, and C. R. Wronski, "Effect of white and red light illuminations on the degradation of a-Si:H solar cells", *Mat. Res. Soc. Symp. Proc.*, in press (1995).

18. H. Liu, C. T. Malone, C. M. Fortmann, and C. R. Wronski, "Analysis of Non-uniform creation of light-induced defects in Schottky barrier solar cell structures", *Mat. Res. Soc. Symp. Proc.*, in press (1995).

19. S. Kim, Y. Lu, and R. W. Collins, "Characterization of compositional gradients in amorphous semiconductor thin films by real time spectroscopic ellipsometry", *Mat. Res. Soc. Symp. Proc.*, in press (1995).

20. R. W. Collins, Y. Lu, S. Kim, and C. R. Wronski, "Real time ellipsometry characterization of a-Si:H based solar cells", *Proc. Int'l Workshop on Semiconductor Characterization*, in press (1995).

21. J. S. Burnham, R. W. Collins, S. Kim, J. Koh, Y. Lu, and C. R. Wronski, "Real time characterization of amorphous silicon solar cell fabrication by spectroscopic ellipsometry", *Surface Analysis '95* (University Park, PA, June 1995).

22. J. Koh, Y. Lu, S. Kim, J. S. Burnham, C. R. Wronski, and R. W. Collins, "Real time spectroellipsometry study of a-Si:H solar cells", *Appl. Phys. Lett.*, in press (1995).

23. S. Kim and R. W. Collins, "Optical characterization of continuous compositional gradients in thin films", *Appl. Phys. Lett.*, in press (1995).

24. R. W. Collins, J. Burnham, S. Kim, J. Koh, Y. Lu, and C. R. Wronski, "Insights into deposition processes for amorphous semiconductor materials and devices", *J. Non-Crys. Solids*, in press (1995).

25. H. Nguyen, S. Kim, Y. Lu, M. Wakagi, R. W. Collins, "Comparison of the optical properties of amorphous and crystalline silicon", *J. Non-Crys. Solids*, in press (1995).

26. I. Chen, L. Jiao, and C. R. Wronski, "A novel approach to the analysis of sub-bandgap absorption in a-Si:H based materials", *J. Non-Crys. Solids*, in press (1995).

27. H. Liu, L. Jiao, S. Semoushkina, and C. R. Wronski, "Distribution of charged defects in a-Si:H Schottky barrier solar cells", *J. Non-Crys. Solids*, in press (1995).

28. R. W. Collins and H. V. Nguyen, "Multichannel ellipsometry", in *Proc. of Highlights of Optical Spectroscopy of Semiconductors*, edited by R. Selci and L. Quagliano (Frascati, Italy, 1995), in press.

REPORT DOCUMENTATION PAGE

Form Approved
OMB NO. 0704-0188

Public reporting burden for this collection of information is estimated to average 1 hour per response, including the time for reviewing instructions, searching existing data sources, gathering and maintaining the data needed, and completing and reviewing the collection of information. Send comments regarding this burden estimate or any other aspect of this collection of information, including suggestions for reducing this burden, to Washington Headquarters Services, Directorate for Information Operations and Reports, 1215 Jefferson Davis Highway, Suite 1204, Arlington, VA 22202-4302, and to the Office of Management and Budget, Paperwork Reduction Project (0704-0188), Washington, DC 20503.

1. AGENCY USE ONLY (Leave blank)	2. REPORT DATE	3. REPORT TYPE AND DATES COVERED
	November 1995	Annual Subcontract Report, 15 July 1994 - 14 July 1995

4. TITLE AND SUBTITLE

Wide-Band-Gap Solar Cells with High Stabilized Performance

5. FUNDING NUMBERS

C: XAN-4-13318-03

TA: PV631101

6. AUTHOR(S)

C.R. Wronski, R.W. Collins, S.J. Fonash, J.S. Burnham, I-S. Chen, L. Jiao, S. Kim, J. Koh, Y. Lee, H. Liu, S. Semoushkina

7. PERFORMING ORGANIZATION NAME(S) AND ADDRESS(ES)

Pennsylvania State University

8. PERFORMING ORGANIZATION REPORT NUMBER

9. SPONSORING/MONITORING AGENCY NAME(S) AND ADDRESS(ES)

National Renewable Energy Laboratory
1617 Cole Blvd.
Golden, CO 80401-3393

10. SPONSORING/MONITORING AGENCY REPORT NUMBER

TP-411-20276

DE96000466

11. SUPPLEMENTARY NOTES

NREL Technical Monitor: W. Luft

12a. DISTRIBUTION/AVAILABILITY STATEMENT

12b. DISTRIBUTION CODE

UC-1262

13. ABSTRACT *(Maximum 200 words)*

This report describes work performed by Pennsylvania State University in collaboration with the NREL Wide-Band-Gap Team. The goal of this team is to develop a single-junction, wide-gap solar cell with good stabilized parameters. The objectives of the subcontract are to (1) develop a cost-effective amorphous silicon PV technology to foster a viable amorphous silicon PV industry in the U.S., ensuring that this industry remains a world leader in the a-Si technology; (2) help the U.S. a-Si PV industry achieve the U.S.DOE PV Program FY 1995 milestone of 10% stable efficiency commercial thin-film modules; (3) help the U.S. a-Si PV industry achieve 12% stable efficiency multi-junction a-Si:H modules for large-scale utility use by the year 2005. Issues covered in this report include (1) improved understanding of stability in materials and solar cells, (2) intrinsic materials optimization, (3) solar cells optimized for intrinsic layer performance, (4) p-type layer optimization, (5) top cell interfaces, and (6) solar cell grading.

14. SUBJECT TERMS

photovoltaics ; solar cells

15. NUMBER OF PAGES
83

16. PRICE CODE

17. SECURITY CLASSIFICATION OF REPORT	18. SECURITY CLASSIFICATION OF THIS PAGE	19. SECURITY CLASSIFICATION OF ABSTRACT	20. LIMITATION OF ABSTRACT
Unclassified	Unclassified	Unclassified	UL